ENERGY, ENVIRONMENT & STORAGE

AN INTERNATIONAL JOURNAL

Volume-2
Issue-2
May, 2022
ISSN:2791-6197

Editor in Chief
Dr. Selahaddin Orhan AKANSU

ENERGY, ENVIRONMENT AND STORAGE

EES JOURNAL

Founded and Published by Erciyes Energy Association

Energy, Environment and Storage Journal is indexed in Crossref

Printed in Turkey

ISSN-2791-6197

EES- EDITORIAL BOARD

BOARD MEMB

AIM AND SCOPE

Energy, Environment and Storage papers consider the prospects of energy technologies, environment, materials, process control and industrial systems. The Energy, Environment and Storage will be published 3 times per year.

Contributions describe novel and significant applications to the fields of:

- Hydrogen Fuels
- Hydrogen and Fuel Cell
- Hydrogen Economic
- Biomass
- Solar PV Technology
- Solar Thermal Applications
- Wind Energy
- Materials for Energy
- Drones and Energy Applications
- Nuclear Energy and Applications
- Hydro Power
- Fuel Technologies (CNG, LNG, LPG, Diesel, Gasoline, Ethanol, etc.)
- Numerical Modelling
- Energy Storage and Systems
- Battery Technologies
- Energy Management
- Heat and Mass Transfer
- Aerodynamics
- Aerospace and Energy Applications
- Combustion
- Electric Vehicle Transportation
- Off-grid Energy Systems
- Environment Management
- Air Pollution
- Water and Wastewater Pollution
- Water and Wastewater Management
- Waste Management
- Global Warming and Climate Change
- Environmental Ecosystem
- Environmental System Modelling and Optimization
- Ecological Applications or Conservation

CONTENTS

Energy, Environment and Storage

JournalHomepage: www.enenstrg.com

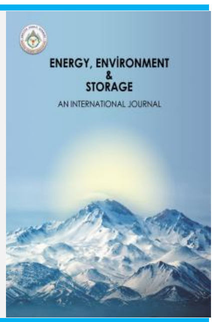

Atmospheric Modeling for Estimating Wind Potential: a Spatio-Temporal Assessment of the Northeast Region of Brazil

Beatriz Rogers Paranhos[1*], Luiz Landau[2], Marcio Cataldi[3]

[1]*Federal Universityof Rio de Janeiro, Alberto Luiz Coimbra Institute for GraduateStudiesandResearch in Engineering, LaboratoryofComputationalMethods in Engineering (LAMCE), Rio de Janeiro Technology Park, Rua Sydiney Martins Gomes dos Santos, 179 - Cidade Universitária, 21941-859, Rio de Janeiro, RJ, Brazil, ORCID:0000-0001-6487-3204*

[2]*Federal Universityof Rio de Janeiro, Alberto Luiz Coimbra Institute for GraduateStudiesandResearch in Engineering, LaboratoryofComputationalMethods in Engineering (LAMCE), Rio de Janeiro Technology Park, Rua Sydiney Martins Gomes dos Santos, 179 - Cidade Universitária, 21941-859, Rio de Janeiro, RJ, Brazil, ORCID: 0000-0001-7857-9946*

[3]*Fluminense Federal University, Technological Center, SchoolofEngineering, Rua Passo da Pátria, 156 - Bloco D, sala 133, 24210-240, Niterói, RJ, Brazil, ORCID: 0000-0001-9769-0105*

ABSTRACT. This work examines, on different aspects, the sensitivity of the Weather Research and Forecasting (WRF) atmospheric model over the Northeast Region of Brazil to evaluate its performance in representing wind speed and direction. Thus, it seeks to stimulate the growth of the wind industry in the country and the improvement of the WRF. For that, three compositions of physical parameterizations are proposed, two focused on the comparison of the Planetary Boundary Layer (PBL) scheme used and one on the global model Global Forecast System (GFS), as well as verified its results in two horizontal resolutions, 3 and 9 km. The first two weeks of March and September 2018 are evaluated. The applied statistical analyzes are validated through observations provided by the National Institute of Meteorology (INMET), as well as by GFS analyzes. The results demonstrate that the YSU-PBL scheme, with the topo_wind option activated, provided, for the periods of study, the most reliable wind reproduction over the Northeast, as well as the arrangement based on the GFS parameterizations. The WRF presents a better performance, when compared to the other analyzed regions, above all, on the northeastern coast, a range of relevant wind potential and, therefore, of great applicability of the model.

Keywords:*WRF, Modeling, Parameterization, Wind Energy,Wind, Brazilian Northeast.*

Article History*: Received:* ***08.01.2022****; Revised:* ***11.02.2022****; Accepted:* ***19.04.2022****; Available online:* ***20.04.2022***
Doi: https://doi.org/10.52924/YNYG1911

1. INTRODUCTION

The global search for trying to stop the climate crisis that is happening on the planet is perceptible through mechanisms such as the Paris Agreement, carried out during the 21st Conference of the Parties (COP 21) in 2015. With the participation of Brazil, this treaty wishes maintain, in relation to pre-industrial levels, the growth of the global average temperature below 2.0º C, through measures that reduce the emission of greenhouse gases [1, 2]. According to Arantegui and Jäger-Waldau [1], approximately 65% of the world's emissions of CO2, a long-lived greenhouse gas, come from the combustion of fossil fuels. Thus, many investments have been made with a focus on the decarbonization of energy sources, one of its main niches being the use and development of wind energy. For example, Hernández et al. [3] estimate that wind energy is capable of reducing total emissions of carbon dioxide in the European Union from approximately 6.600 to 13.100 Mt, depending on the technology involved, between 2015 and 2050.

In 2019, the total installed capacity of wind generation in the world was 650,758 MW. This is reflected in a growth of around 104%, when compared to 2013, and of about 33%, in relation to 2016 [4]. Such expansion of the sector is also observed in the Brazilian territory. According to EPE [5], in 2019, in the country, electrical production from wind energy was 55.986 GWh, which translates into an increase of approximately 15.5% when compared to the previous year. The Northeast Region is, in Brazil, the one that most develops in this branch, having generated, in 2019, about 89% of the electricity coming from this source. In order to minimize uncertainties in the wind estimate, which undermines the country's energy security and the expansion of the wind industry, it is

[*]Corresponding author: beatriz.paranhos@coc.ufrj.br

necessary to use efficient mechanisms for its forecast. In this sense, the WRF presents itself as one of the most widely used atmospheric models worldwide, with wide possibilities for evolution [6]. Although it is a promising tool for gauging wind data, considering the physical phenomena acting on a given surface and reducing the dependence on instrumental apparatus for in situ measurements, authors such as Carvalho et al. [7], Draxl et al. [8] and Santos-Alamillos et al. [9], demonstrate that the WRF's performance varies depending on specific factors of the simulation area in question. Therefore, sensitivity analyzes of the model have been carried out in different parts of the planet, in order to find better possibilities of local wind forecasts compared to the alternatives offered by the WRF and favoring the development of the model. This is the case of the work by Avolio et al. [10] that, among 5 evaluated WRF Planetary Boundary Layer schemes applied in the region of Calabria, Italy, found that ACM2 and YSU obtained the most satisfactory performances both in terms of wind speed and direction, when considering the vertical profile of the wind. The study by Carvalho et al. [7] compared 5 WRF PBL schemes over the Iberian Peninsula, noting that the most suitable performance for wind data simulation and for wind production estimates was ACM2. Thus, the present study aims to analyze the sensitivity of the WRF model, with regard to its wind speed and direction results, over the Northeast Region of Brazil, seeking to reduce associated errors and, thus, favor the operational planning of wind parks and the management of the distribution of the generated energy, as well as encouraging the growth of this sector in the country, the improvement of the WRF in this area of the map and providing support for new scientific research. For this, in this work it is evaluated, through high performance modeling, which physical parameterizations, among three different arrangements, lead to a more satisfactory local representation of the wind, using two horizontal resolutions, at two different times of the year. In addition, we find out at which points in the northeastern territory the WRF provides the most appropriate wind performance and which areas are most vulnerable to low quality reproductions.

In addition, in order to verify the degree of influence of the input data used and their treatment, the results of the WRF are compared to those referring to the analysis of the GFS model, applied as an initial and boundary condition in the simulations. This article is organized as follows: Section 2 gathers the materials and methods used, detailing the study area, the choice of data to validate the results, the adjustment of the WRF and the characteristics of the simulations, as well as the use of the GFS and the statistics selected for evaluation. Section 3 presents the results and the associated discussions. Section 4 makes the final considerations and concludes the work.

2. MATERIALS AND METHODS

2.1 Study area and selection of observed data

The Northeast Region of Brazil is composed of the States of Maranhão (MA), Piauí (PI), Ceará (CE), Rio Grande do Norte (RN), Paraíba (PB), Pernambuco (PE), Alagoas (AL), Sergipe (SE) and Bahia (BA). Its territory extends for more than 1.5 million km2, being the Region that shelters the largest coast of the country, with more than 3 thousand km of dimension [11]. The Northeast has a large share in the generation of Brazilian wind energy [5]. Because of this, the present work sought to concentrate its study area in the zone that encompasses the main northeastern wind farms, aiming to assist the different users of wind data for better decision making, as well as to favor the analysis of localities for future wind use [12]. In order to validate the results of this study, anemometric data from automatic surface observation meteorological stations from the National Institute of Meteorology, measured at a height of 10 m, were selected [13]. In all, 18 stations were elected, 2 in each state in the Northeast Region (Table 1). A satisfactory spatial distribution of the observed data was sought together with its complete hourly availability for the periods of time used.

Despite such an effort, the Aracaú Station (A360), in Ceará, did not present some data for the wind direction of September 2018. Therefore, its validation of the direction in that month was discarded, only performing such procedure for the wind speed.

2.2 Adjusting the WRF and characterizing the simulations

The sensitivity tests were performed considering version 4.0.3 of the Advanced Research WRF (ARW-WRF), developed by the National Center for Atmospheric Research (NCAR). So that a high performance modeling was computationally executable, this work relied on the use of the supercomputer Lobo Carneiro, from the Alberto Luiz Coimbra Institute for Graduate Studies and Research in Engineering (COPPE), at the Federal University of Rio de Janeiro (UFRJ). In adjusting the WRF, two domains were used (Figure 1), whose nesting occurred with the exchange of information in one-way. The first one, d01, with a horizontal resolution of 9 km, was dimensioned at 3,600 km x 3,600 km. The second, d02, refers to the study area, with dimensions of 1,425 km x 1,425 km and horizontal grid spacing of 3 km. The central point of the two grids is located in the southeast of the State of Ceará, at -7.02 latitude and -39.29 longitude. In order to smooth cartographic distortions on the study area, located near the Equator, the projection selected was that of Mercator [14].

Table 1 Selected Weather Stations and their main characteristics

State	City	Station code	Detainer	Latitude (^{0})	Longitude (^{0})	Altitude (m)
Alagoas	Maceió	A303	INMET	-9.55	-35.77	84
	Palmeira dos Índios	A327	INMET	-9.42	-36.62	278
Bahia	Lençóis	A425	INMET	-12.56	-41.39	438
	Uauá	A435	INMET	-9.83	-39.50	451
Ceará	Aracaú	A360	INMET	-3.12	-40.09	67
	Jaguaribe	A358	INMET	-5.91	-38.63	149
Maranhão	Bacabal	A220	INMET	-4.24	-44.79	22
	Farol Santana	A217	INMET	-2.27	-43.62	10
Paraíba	Campina Grande	A313	INMET	-7.23	-35.90	546
	Patos	A321	INMET	-7.08	-37.27	264
Pernambuco	Arco verde	A309	INMET	-8.43	-37.06	684
	Serra Talhada	A350	INMET	-7.95	-38.30	499
Piauí	Caracol	A337	INMET	-9.29	-43.32	515
	Picos	A343	INMET	-7.07	-41.40	233
Rio Grande do Norte	Mossoró	A318	INMET	-4.90	-37.37	29
	Natal	A304	INMET	-5.84	-35.21	47
Sergipe	Aracajú	A409	INMET	-10.95	-37.05	4
	Poço Verde	A419	INMET	-10.74	-38.11	367

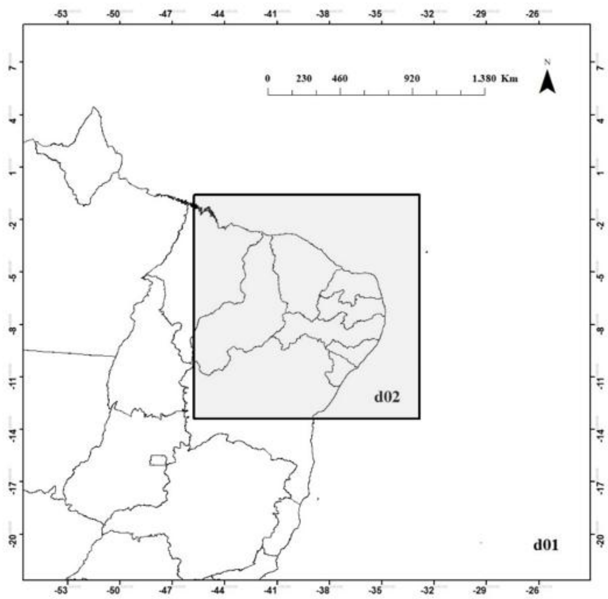

Fig. 1. Layout of the grids used in the WRF simulations

The initial and boundary conditions were obtained from the National Centers for Environmental Prediction (NCEP), through the analysis of the global GFS model, provided every 6 hours, with a horizontal resolution of 0.25o. Topography and land use data came from the Moderate Resolution Imaging Spectroradiometer (MODIS), configured at a resolution of 30 arc seconds for both grids.

The vertical resolution of the WRF was set at 45 vertical levels, with 12 of these levels less than 500 m from the surface. In order to soften the orographic effects on the surface coordinates, and, consequently, to avoid numerical errors, the hybrid coordinate system was used [15]. In order to carry out the simulations, in 2018, the first half of March was selected, a month typically with high rainfall levels in the Northeast Region and low wind intensities. In addition, the first fifteen days of September 2018 were chosen, as it is a time of low rainfall and high wind intensity in this extension of the Brazilian territory [16, 17].

The simulations were divided into one initialization and two more reinitializations for each of the evaluated fortnights, seeking to reduce numerical errors in the representation of the wind [18, 19]. In each execution, the first 6 h of simulation were discarded, considered time for model adjustment (spin up) so that the WRF would achieve computational stability [20].The time intervals that make up each of the simulations of March and September 2018 are shown in Table 2 and Table 3, respectively. It is worth mentioning that the file of initial conditions and contour of February 28, 2018, from 18h UTC, was damaged, being neglected. Soon, the March simulations started at 00h UTC on the 1st.

Table 2 Time intervals of the March 2018 simulations

Start	End
00h UTC 03/01/2018	06h UTC 03/06/2018
00h UTC 03/06/2018	06h UTC 03/11/2018
00h UTC 03/11/2018	06h UTC 03/16/2018

Table 3 Time intervals of the September 2018 simulations

Start	End
18h UTC 08/31/2018	00h UTC 09/06/2018
18h UTC 09/05/2018	00h UTC 09/11/2018
18h UTC 09/10/2018	00h UTC 09/16/2018

Three different arrangements were selected for physical parameterizations, called configuration 1 (C1), configuration 2 (C2) and configuration 3 (C3), gathered in Table 4, Table 5 and Table 6, in that order. The first two are differentiated by the Planetary Limit Layer scheme adopted, with the Microphysics, Long Wave Radiation, Short Wave Radiation, Surface Layer, Earth Surface Model and Cumulus schemes being fixed. The PBL options employed were the Yonsei University Scheme (YSU), in C1, and the Asymmetric Convection Model 2 Scheme (ACM2), in C2 [21, 22]. It is noteworthy that, in all cases, the Cumulus parameterization was only activated for the 9 km grid [23, 24].

Table 4 Physical parameterizations used in the C1 configuration

Physical process	Scheme	References
Microphysics	WSM6	[30]
Long wave radiation	RRTMG	[31]
Short wave radiation	RRTMG	[31]
Surface Layer	Revised MM5 Monin-Obukhov + topo_wind	[25, 32]
Land surface model	Unified Noah *Land-Surface Model*	[33]
Planetary boundary layer	YSU	[21]
Cumulus	Kain-Fritsch	[34]

Along with the parameterization of the Surface Layer, in C1, the Topographic Correction for Surface Winds to Represent Extra Drag from Sub – grid Topography and Enhanced Flow at Hill Tops (topo_wind) option 1 (Jiménez method) was included. It works only coupled to YSU and its main objective is to reproduce the orographic effects on surface circulations on a sub-grid scale [25]. In turn, for the composition of C3, physical parameterizations inspired by those used by the global GFS model were chosen. It is noteworthy that the MYNN 2.5 options were activated for the mass flow scheme (bl_mynn_edmf = 1), the movement quantity transport scheme (bl_mynn_edmf_mom = 1) and the Turbulent Kinetic Energy transport scheme - TKE (bl_mynn_edmf_tke = 1) [26, 27, 28, 29].

Table 5 Physical parameterizations used in the C2 configuration

Physical process	Scheme	References
Microphysics	WSM6	[30]
Long wave radiation	RRTMG	[31]
Short wave radiation	RRTMG	[31]
Surface Layer	Revised MM5 Monin-Obukhov	[32]
Land surface model	Unified Noah *Land-Surface Model*	[33]
Planetary boundary layer	ACM2	[22]
Cumulus	Kain-Fritsch	[34]

Table 6 Physical parameterizations used in the C3 configuration

Physical process	Scheme	References
Microphysics	Eta Ferrier	[35]
Long wave radiation	RRTMG	[31]
Short wave radiation	RRMTG	[31]
Surface Layer	MYNN	
Land surface model	Unified Noah *Land-Surface Model*	[33]
Planetary boundary layer	MYNN 2.5	[36, 37, 38]
Cumulus	New Simplified Arakawa–Schubert Scheme (for Basic WRF)	[39, 40]

2.3 Using GFS

From the GFS analysis data used as the initial and boundary condition in the WRF simulations, for the same periods, the performances of the global model were also directly evaluated. Thus, the GFS analyzes served as another way to validate the results of the WRF simulations.
In addition, the comparison between wind speed and direction provided by WRF and GFS analyzes helps to ascertain the sensitivity of the first model, considering whether the greatest impact on performance comes from the selection of physical parameterizations or from the initial and contour conditions themselves employed.

2.4 Applied statistics

Different statistical metrics were used to verify the accuracy of the WRF results, with the 3 and 9 km resolution grids, and the GFS analyzes. The calculations were performed with the hourly results provided by the WRF every 6 h, so that they could be compared to the GFS analyzes.

For the wind speed, the Bias, the Root Mean Squared Error (RMSE) and the Correlation Coefficient (r) were used, according to equations (1), (2) and (3), respectively [10, 41, 42].

Bias was applied to measure the model's tendency to overestimate or underestimate its results in relation to reality. The RMSE, in turn, reflects the average magnitude of the error regardless of the signal. Already, the use of r sought to evaluate the ability of the models to monitor the variability of the wind speed, through the linear relationship between the measured data and the observed data [43, 44].

$$Bias = 1/n \sum_{i=1}^{n} (P - O) \quad (1)$$

$$RMSE = \sqrt{1/n \sum_{i=1}^{n} (P - O)^2} \quad (2)$$

$$r = \frac{\sum_{i=1}^{n} (P-\bar{P})(O-\bar{O})}{\sqrt{\sum_{i=1}^{n} (P-\bar{P})^2 (O-\bar{O})^2}} \quad (3)$$

The wind direction was separated into classes, the octants (Table 7), to check whether the WRF simulations and GFS analyzes were able to indicate the correct octant of the direction, or, if not, if one of its neighboring octants was pointed out. Thus, the percentage of errors, in relation to the total sample, in stating the exact octant of the direction, as well as the percentage of relative errors in addition to the octants neighboring to the observed were stipulated.

Modern horizontal-axis wind turbines have orientation mechanisms capable of aligning their rotors and blades according to the wind direction, and it is not essential for this industry to accurately estimate this direction [45].

Table 7 Wind direction octants and their direction intervals

Direction octant	Interval
North	[0.0° – 22.5°]
Northeast	[22.5° – 67.5°]
East	[67.5° – 112.5°]
South east	[112.5° – 157.5°]
South	[157.5° – 202.5°]
South west	[202.5° – 247.5°]
West	[247.5° – 292.5°]
Northwest	[292.5° – 337.5°]

3.RESULTS AND DISCUSSION

3.1 Bias

The Bias of the wind speed at 10 m in height, for each of the selected stations, in the first half of March 2018, can be evaluated through Figure 2. In it, the results of each of the proposed WRF configurations are gathered, in the horizontal resolutions of 3 and 9 km, and of the analysis of the GFS.

It can be seen, through the presentation of positive Bias, that the WRF simulations overestimate, in all places and with both domains, the wind speed. GFS analyzes, in general, show the same trend in the period, except in Picos-PI, where they underestimate the speed. Although negative, this Bias is close to zero. In addition, it is possible to observe that, in 10 of the 18 stations, the resolution of 9 km obtains average errors lower than that of 3 km.

Figure 3 shows the Bias of the wind speed at 10 m for the first fifteen days of September 2018. In this period, it is noted, due to its positive values, that there is again an overestimation of the wind speed in relation to the data observed with all the simulated WRF options and everywhere. The GFS analyzes underestimate the speed in Maceió - AL and in Arco Verde - PE. Contrary to what was observed in March 13 of the 18 points achieved superior performances with the 3 km grid with at least one of the WRF configurations.

Authors such as Carvalho et al. [46] and Avolio et al. [10], among others, had already demonstrated the WRF's propensity to overestimate wind speed. The first group, found, in Portugal, that this trend is due to the smoothing and simplification of the representation of the terrain by the model. While the second group observed a similar pattern in southern Italy.

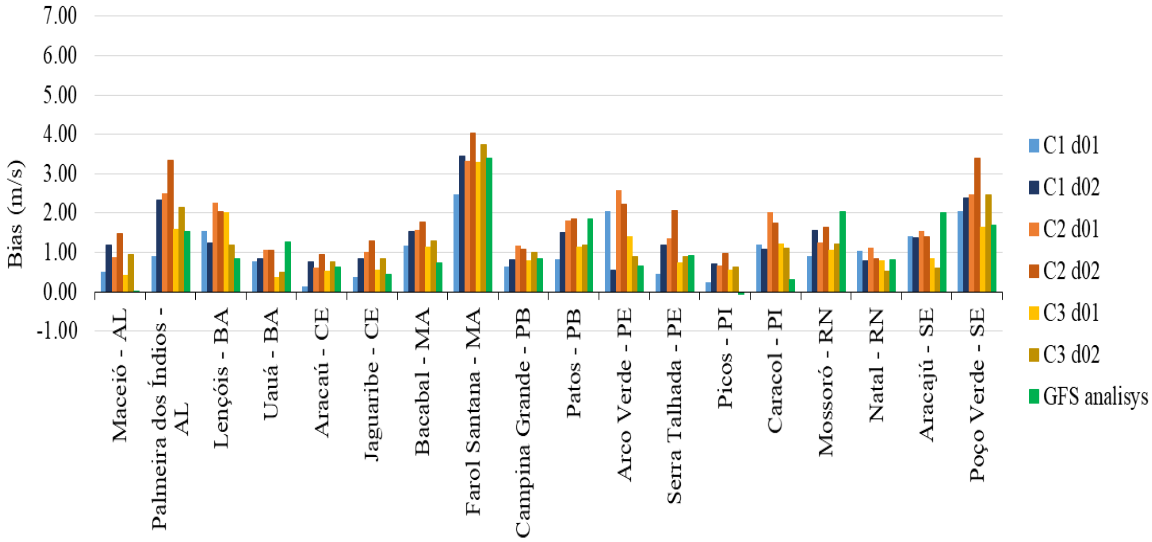

Fig. 2. Average errors (Bias) of wind speed at 10 m high - first half of March 2018

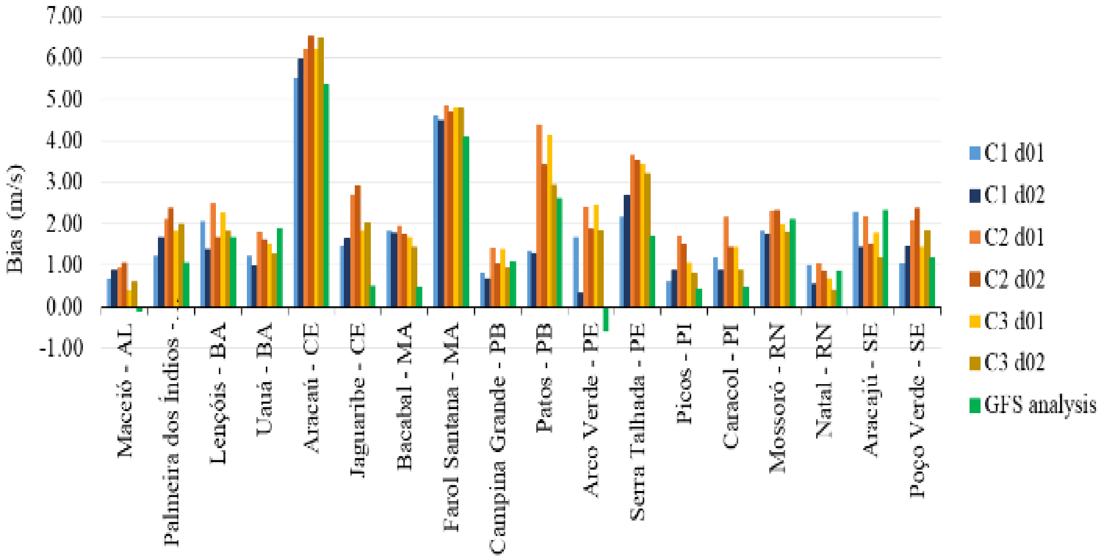

Fig. 3. Average errors (Bias) of wind speed at 10 m high - first half of September 2018

3.2 Spatial distribution of applied statistics

Figure 4 represents the spatial distribution of the lowest values of the RMSE, in (a) and (b), and of the highest r, in (c) and (d). Figure 5 gathers the lowest percentages of the indication of the wrong direction octant, in (a) and (b), and the lowest percentages of error in addition to the octants neighboring the correct one, in (c) and (d). The images on the left (a) and (c), in the two figures, refer to the interval of fifteen days in March and those on the right, (b) and (d), referring to the fifteen days of September 2018.

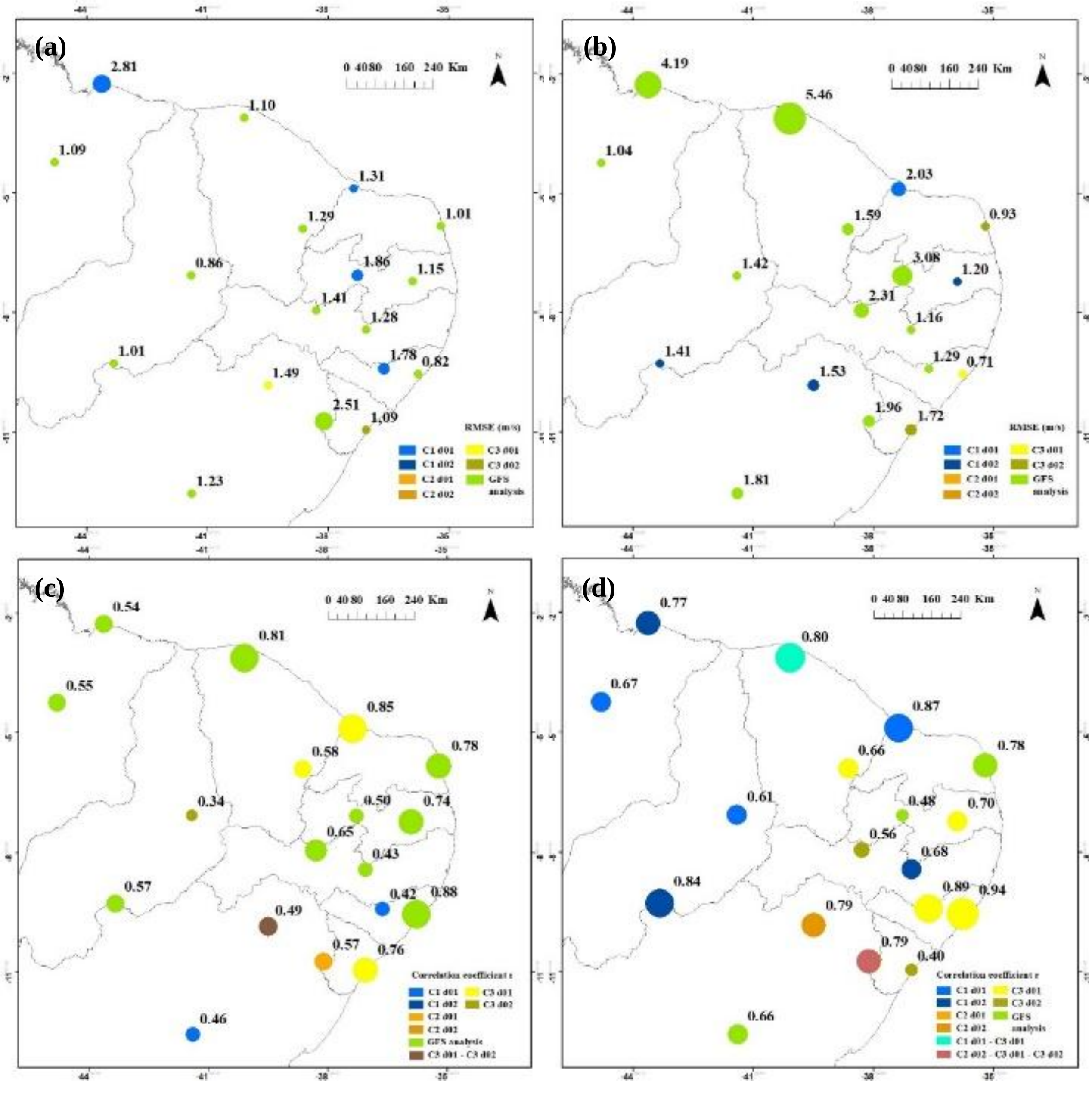

Fig. 4. Spatial distribution of the smallest errors in wind speed at 10 m in height: (a) RMSE for the first half of March 2018; (b) RMSE for the first half of September 2018; (c) r for the first half of March 2018; (d) r for the first half of September 2018

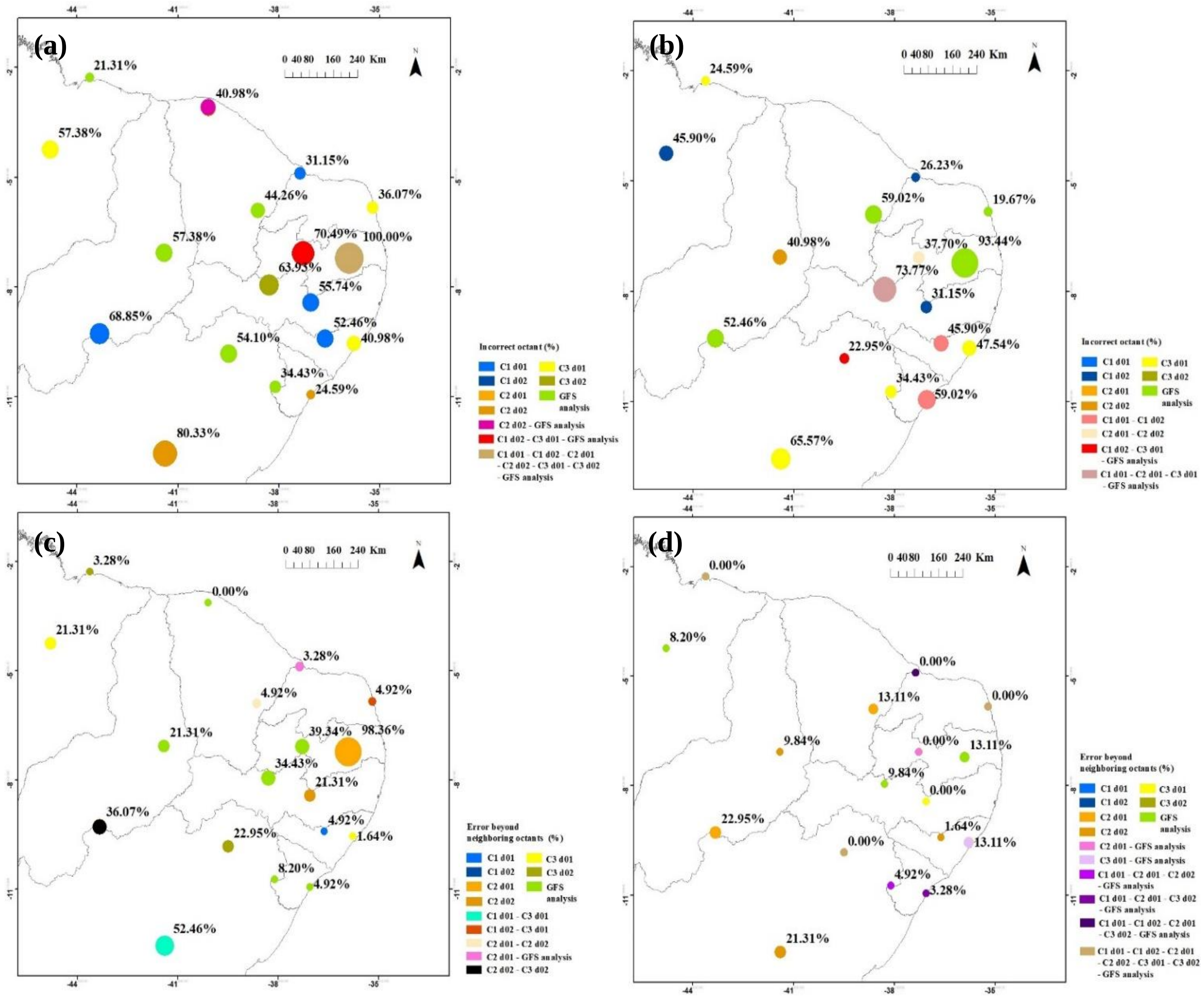

Fig. 5. Spatial distribution of the smallest errors in the wind direction at 10 m in height: (a) RMSE for the first half of March 2018; (b) RMSE for the first half of September 2018; (c) r for the first half of March 2018; (d) r for the first half of September 2018

It can be seen, through the analysis of Figure 4, that the magnitude of the error on the wind speed is predominantly lower, on the territory, with the analyzes of the GFS, both in March and in September. The lower horizontal resolution of GFS analyzes can influence the smallest errors in this magnitude, overestimating this speed with less intensity. As it is a systematic error, it can be corrected, for example, statistically in its post-processing [47].

In March, the WRF simulation that has the largest number of smaller RMSE on the map is the one that uses C1 in the 9 km resolution, all at points that the simulations in general had more difficulty to represent. On the other hand, C3-based reproduction obtained the smallest errors at two points close to each other, north of Bahia, with 9 km of resolution, and on the coast of Sergipe, with 3 km of resolution. In the first half of September, C1 is also the WRF option with the highest frequency of minor errors, after GFS analyzes. However, this occurs mostly with the 3 km grid. The simulations with C3 have better results at three points, all on the east coast, also with emphasis on the daughter grid. Representations with C2 do not achieve the best performance in any of the evaluation points and intervals.

From the point of view of the linear correlation of wind speed, in March, the GFS analyzes have the best results in most of the map. The application of configuration 3, especially in the resolution of 9 km, is the one that reaches a greater extension of the study area with the highest values of r.

Differently, in September, it is the WRF simulations that predominate with the strongest correlations. Basically, options C1 and C3 obtain the best correlations, with this configuration having one more station of advantage than that. In both cases, the highest frequency of strong correlations occurs with the 9 km grid.

Despite the increase in the error on the magnitude of the wind speed from March to September, there is an increase in the Correlation Coefficient from one period to the next over the entire length of the territory. The accurate estimate of the variability of the wind over time is substantial for the quality of the energy produced and its adequate planning, being, therefore, a relevant aspect that the WRF is able to offer strong correlations.

Through Figure 5, it is noted that, in March 2018, there is heterogeneity between the options that reach the lowest percentage of wrong octants of the wind direction at 10 m high. Nevertheless, GFS analyzes still stand out on the study area, either in isolation or in conjunction with some WRF simulation. Then, the reproductions of C1 and C3 obtain the same number of points with the smallest errors, with an emphasis on the resolution of 9 km.

In the case of the first half of September 2018, once again a heterogeneous distribution of the alternatives with the lowest percentages of error is observed. During this period, GFS analyzes and WRF simulations using C3, with the 9 km grid, are tied with the greatest number of locations where they achieve superior performance. As for the smallest errors in addition to the octant neighbours to the correct one, in March, a greater presence of the different WRF simulation options on the map is noted. In addition, reproductions with C3 match the GFS analysis and achieve the best performance in this regard, with the 9 km grid appearing and a location more than that of 3 km

In September 2018, a large part of the points generated errors in addition to the neighbouring octants below 10%. In the meantime, there are many places where this occurs with more than one alternative. The simulations associated with configuration 2 are the ones with the best performance, with the 9 km grid taking advantage of two locations in relation to the 3 km. It is worth highlighting the tendency of decreasing the percentage of errors in the wind direction, at 10 m height, from March to September 2018. Furthermore, the aptitude of both WRF simulations and GFS analyzes is demonstrated when, when they do not get it right the octant of the direction, point one of the neighbours to the correct one.

The GFS analyzes were expected to show more representative results of the wind, over the Northeast Region, for all statistical investigations. This is because these analyzes contain observed data assimilated throughout its domain, whereas the WRF had its contact with these observations limited to the initial and boundary conditions.

This oscillation in the WRF's ability to perform better or worse than the GFS analyzes reflects the impact, in the results, of both the input and contour information in the model and the appropriate choice of physical parameterizations for the desired location. The different maps indicate that the Northeast coast tends to have the results closest to reality, both for speed and wind direction. The highlight is on the east coast, an area of significant wind power generation capacity [48]. The north coast, especially on the coast of Maranhão and Ceará, despite good reliability for the linear correlation and for determining the direction octant, has low accuracy for the magnitude of the wind speed error. The area that, predominantly, presented the worst statistical performances of wind speed and direction, at 10 m in height, was that which covers the interior of Paraíba and Pernambuco, as well as Lençóis, located in the most central part of Bahia.

Note that Campina Grande behaved as an outlier within the sample, with errors in the indication of the wind direction above 90% when applying all WRF options, as well as with the GFS analyzes. It was only in the period of September 2018 that the error, besides the neighboring octants, in this place, managed to fall to less than 15%.

The performance of atmospheric systems over the Northeast Region may influence the similar behavior between the WRF simulations and the GFS analyzes on the map. The interior of Paraíba and Pernambuco is influenced by the Intertropical Convergence Zone (ZCIT) and also suffers the impacts of moisture transport from the ocean to the continent, being characterized as a place of formation of Lines of Instability and that can be covered by precipitation induced by Upper Tropospheric Cyclonic Vortex (UTCV) [49,50].

The central area of Bahia, on the other hand, is mainly affected by cold fronts and the formation of a UTCV. The South Atlantic Subtropical Anticyclone (SASA) is also able to impact this portion of the map thanks to the displacement of moisture inland [49, 50]. Otherwise, the northeastern coast, starting from Rio Grande do Norte and ending in Sergipe, suffers interference from trade winds and breeze circulation, in addition to SASA, favoring the intensification and stability of the wind [49, 50].

Thus, there is an association between areas of greater susceptibility to cloud formation with a worse performance in wind simulations by WRF. The occurrence of precipitation tends to weaken the intensity of the winds in the Northeast, which, in turn, generates greater vulnerability of the model to errors [17]. In addition, in March 2018, a La Niña ended [51]. According to Santos e Silva [17], this phenomenon is also responsible for contributing to the decrease in wind intensity in the Northeast Region of Brazil.

3.3 Topographic analysis

In order to complement the spatio-temporal analyzes, a map was created representing the altimetric difference between the dimensions provided by Embrapa's Digital Elevation Model (DEM) [52], with a resolution equivalent to approximately 90 m, and the dimensions applied by WRF to represent the topography of the region, of about 1 km of resolution.

Through Figure 6, there is a predominance of negative differences between the DEM and the topography used by the WRF, indicating the propensity of this model to apply a higher level than the real one. The average of this altitude difference over the study area is -2 m and its standard deviation is 65 m.

The coastal strip is, in general, able to have a realistic topographic representation within the WRF, as observed by the small altimetric difference in relation to the MDE. This fact reaffirms the quality of the model's performance in estimating wind speed and direction in this region. In contrast, in the interior of Paraíba and Pernambuco, a place of low wind performance in the evaluated periods, the quota differences fluctuate between positive and negative over small distances. A similar situation occurs in Lençóis, Bahia. This variation in the representation of the topography by the WRF may end up intervening in the intensity and direction of the atmospheric flow over these regions, impairing the performance of the simulations [53].

Santos et al. [54] had already observed in Triunfo, interior of Pernambuco, a smoothing of topographic conditions in the WRF in relation to reality. However, the authors reached underestimated results of wind speed, which goes in the opposite direction to that observed in the present work, in which overestimated results were found.

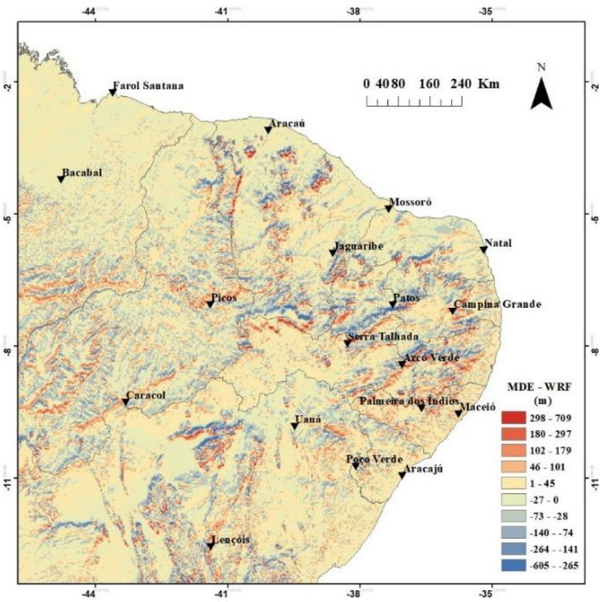

Fig. 6. Altimetric difference between a Digital Elevation Model and the topographic representation of the WRF

4.CONCLUSIONS

This work aimed to analyze, under different spectra, the sensitivity of the WRF atmospheric model in relation to the wind data produced by it over the Northeast Region of Brazil. Therefore, we sought to verify which parameter composition was capable of providing more reliable wind results.

Of the three physical parameterization arrangements investigated, configurations C1 and C3 were, within the studied time intervals, those that presented simulations together with performances more representative of both the speed and the direction of the wind in the different points of the study area.

The C1 configuration consists of the YSU scheme for the Planetary Boundary Layer, with the topo_wind option enabled. On the other hand, C3 is the GFS-based arrangement, which contains the MYNN 2.5 scheme for the PBL. The other characteristics of C1 and C3 are detailed in section 2.2.

In general, in the evaluated periods, the GFS analyzes showed lower errors regarding the magnitude of the wind intensity, while the WRF simulations achieved greater successes with its ability to express the variability of the wind speed over time and its direction. . As the errors on the magnitude are simpler for statistical correction than the others, the use of WRF showed an advantage in relation to GFS analyzes. The outstanding performance of the WRF simulations on the GFS analyzes was not assumed, since the said analyzes, despite their lower resolution, assimilate data observed in their domain. The WRF, on the other hand, had contact with these data restricted to initial and frontier conditions. In an operational forecast, after using the GFS analysis in the initial conditions, the WRF only has information from the GFS forecast as a boundary condition and from the WRF forecast itself. Spatially examining,it was noted that the most accurate performances, both in the WRF simulations and in the GFS analyzes, tend to be concentrated on the northeastern coast, especially on the east coast, which is a particularly favorable track for wind generation. In other words, the WRF has a promising application for the sector in these locations. Otherwise, the most discrepant wind results in relation to the observations are, above all, in nuclei in the interior of Paraíba and Pernambuco, as well as more in the center of Bahia.

In terms of seasonality, it was noted that in the first half of September the WRF simulations performed better than the same period in March. In addition to being a month often of more intense rainfall and milder wind speeds in the Northeast, in 2018, March passed the end of a La Niña, which may have made the model's representations even more difficult.

In addition, it was found that, in the period of greatest instability and cloudiness, March, simulations that contained a lower grid resolution tended to achieve better performance. In the time of more stable weather, September, a more refined resolution was necessary to reach lower errors on the intensity of the wind and, in the case of variability and direction, this oscillated more evenly according to the season investigated.

The different wind behaviors reproduced by the WRF over the Northeast region are in line with the topographic representation capacity used by the model. The most critical points observed in terms of accuracy tend to be those in which the topography used by the WRF is more coarse, which ends up affecting the air flow simulation.

For future work, it is suggested that sensitivity analyzes be carried out on the Northeast Region, encompassing a wider range of arrangements for physical parameterizations, as well as that simulations be carried out for longer periods of time and for other times of the year.

In addition, it is proposed to add to such evaluations the comparison between simulations that perform the technique of assimilation of observed data and those without this mechanism activated, to verify the ability to improve or not in the reproduction of the wind in the Northeast.

Acknowledgments
This study was financed in part by the Coordenação de Aperfeiçoamento de Pessoal de Nível Superior - Brasil (CAPES) - FinanceCode 001. Research developed with the support of the Advanced High Performance Computing Center (NACAD) at COPPE, Federal University of Rio de Janeiro (UFRJ). The authors would like to thank CAPES, NACAD and INMET, fundamental pieces for the accomplishment of this work.

REFERENCES

[1] Arantegui, R. L.; Jäger-Waldau, A. Photovoltaics and wind status in the European Union after the Paris Agreement. Renewable and Sustainable Energy Reviews, v. 81, p. 2460-2471, 2018.

[2] Hoegh-Guldberg, Ove et al. The human imperative of stabilizing global climate change at 1.5 C. Science, v. 365, n. 6459, 2019.

[3] Hernández, C. V.; González, J. S.; Fernández-Blanco, R. New method to assess the long-term role of wind energy generation in reduction of CO2 emissions – case study of the European union. Journal of cleaner production, v. 207, p. 1099-1111, 2019.

[4] WWEA. Statistics. WWEA/World Wind Energy Association. Available at: https://wwindea.org/blog/category/statistics/. Accessed on 20 nov. 2020.

[5] EPE. BalançoEnergético Nacional 2020: Ano base 2019 (National Energy Balance 2020: Base year 2019). EPE/Energy Research Company. Rio de Janeiro. 2020.

[6] Powers, J. G. et al. The weather research and forecasting model: Overview, system efforts, and future directions. Bulletin of the American Meteorological Society, v. 98, n. 8, p. 1717–1737, 2017.

[7] Carvalho, D. et al. Sensitivity of the WRF model wind simulation and wind energy production estimates to planetary boundary layer parameterizations for onshore and offshore areas in the Iberian Peninsula. Applied Energy, Vol. 135, p. 234–246, 2014.

[8] Draxl, C. et al. Evaluating winds and vertical wind shear from Weather Research and Forecasting model forecasts using seven planetary boundary layer schemes. Wind Energy, v. 17, n. 1, p. 39-55, 2014.

[9] Santos-Alamillos, F. J. et al. Analysis of WRF model wind estimate sensitivity to physics parameterization choice and terrain representation in Andalusia (Southern Spain). Journal of Applied Meteorology and Climatology, v. 52, n. 7, p. 1592–1609, 2013.

[10] Avolio, E. et al. Sensitivity analysis of WRF model PBL schemes in simulating boundary-layer variables in southern Italy: An experimental campaign. Atmospheric Research, v. 192, n. April, p. 58–71, 2017.

[11] Getirana, A.; Libonati, R.; Cataldi, M. Brazil is in water crisis – it needs a drought plan. Nature, v. 600, p. 218-220, 2021.

[12] IBGE. Anuário Estatístico do Brasil (Brazilian Statistical Yearbook). IBGE/ Brazilian Institute of Geography and Statistics. Rio de Janeiro, v.79, p.1-1-8-50, 2020.

[13] Abeeólica. Números Abeeólica – Fevereiro de 2019 (ABEEólica Numbers - February 2019). Abeeólica/Brazilian Wind Energy Association. Available at: http://abeeolica.org.br/dados-abeeolica/. Accessed on 17 jan. 2020.

[14] Inmet. Technical Note no 001/2011/Seger/Laime/Csc/Inmet. Inmet/ National Institute of Meteorology. n. 001, p. 1–11, 2011.

[15] NCAR. WRF-ARW version 4 Modeling System User's Guide. NCAR/National Center For Atmospheric Research. Mesoscale & Microscale Meteorology Division. 2019.

[16] Park, S.-H.; Klemp, J. B.; Kim, J.-H. Hybrid Mass Coordinate in WRF-ARW and Its Impact on Upper-Level Turbulence Forecasting. Monthly Weather Review, Vol. 147, n. 3, p. 971–985, 2019.

[17] Silveira, C. DA S. et al. Seasonality of Precipitation Over the Northern Brazilian Northeast in the Simulations of the IPCC-AR4. Revista Brasileira de Recursos Hídricos (Brazilian Journal of Water Resources), v. 17, n. 3, p. 125–134, 2012.

[18] Santos, A. T. S.; Silva, C. M. S. Seasonality, Interannual Variability, and Linear Tendency of Wind Speeds in the Northeast Brazil from 1986 To 2011. The Scientific World Journal, v. 2013, p. 1–10, 2013.

[19] Qian, J.-H.; Seth, A.; Zebiak, S. Reinitialized versus Continuous Simulations for Regional Climate Downscaling. Monthly Weather Review, Vol. 131, n. 11, p. 2857–2874, 2003.

[20] Lo, J. C. F .; Yang, Z. L.; Pielke, R. A. Assessment of three dynamical climate downscaling methods using the Weather Research and Forecasting (WRF) model. Journal of Geophysical Research Atmospheres, v. 113, n. 9, 2008.

[21] Lucas-Picher, P. et al. Dynamical Downscaling with Reinitializations: A Method to Generate Finescale Climate Datasets Suitable for Impact Studies. Journal of Hydrometeorology, v. 14, n. 4, p. 1159–1174, 2013.

[22] HONG, S.-Y.; Noh, Y.; Dudhia, J. A New Vertical Diffusion Package with an Explicit Treatment of Entrainment Processes. Monthly Weather Review, Vol. 134, n. 9, p. 2318–2341, 2006.

[23] Pleim, J. E. A Combined Local and Nonlocal Closure Model for the Atmospheric Boundary Layer. Part I: Model Description and Testing. Journal of Applied Meteorology and Climatology, v. 46, n. 9, p. 1383–1395, 2007.

[24] De Meij, A.; Vinuesa, J. F.; Maupas, V. Ghi calculation sensitivity on microphysics, land- and cumulus parameterization in WRF over the Reunion Island. Atmospheric Research, v. 204, n. January, p. 12–20, 2018.

[25] Skamarock, W. et al. A description of the advanced research WRF version 4. Technical Report, March, p. 162, 2019.

[26] Jiménez, P. A.; Dudhia, J. Improving the representation of resolved and unresolved topographic effects on surface wind in the wrf model. Journal of Applied Meteorology and Climatology, v. 51, n. 2, p. 300–316, 2012.

[27] DTC. Common Community Physics Package (CCPP) Scientific Documentation Version 3.0. DTC/Developmental Testbed Center. Available at: https://dtcenter.org/GMTB/v3.0/sci_doc/allscheme_page.html. Accessed on 6 jan. 2020.

[28] DTC. GFS Operational Physics Documentation. DTC/Developmental Testbed Center. Available at: https://dtcenter.org/GMTB/gfs_phys_doc_dev/index.html. Accessed on 6 jan. 2020.

[29] NOAA. Global Forecast System - Global Spectral Model (GSM) - v13.0.2. NOAA/National Oceanic and Atmospheric Administration. Available at: https://vlab.ncep.noaa.gov/web/gfs/documentation. Accessed on 6 jan. 2020.

[30] Campana, K. et al. The Development and Success of NCEP's Global Forecast System. In: 99th American Meteorological Society Annual Meeting. AMS, 2019.

[31] Hong, S-Y; Lim, J-O J. The WRF single-moment 6-class microphysics scheme (WSM6). Asia-Pacific Journal of Atmospheric Sciences, v. 42, n. 2, p. 129-151, 2006.

[32] Iacono, M. J. et al. Radiative forcing by long-lived greenhouse gases: Calculations with the AER radiative transfer models. Journal of Geophysical Research Atmospheres, v. 113, n. 13, p. 2–9, 2008.

[33] Jiménez, P. A. et al. A Revised Scheme for the WRF Surface Layer Formulation. Monthly Weather Review, Vol. 140, n. 3, p. 898–918, 2012.

[34] Tewari, M. et al. Implementation and verification of the unified noah land surface model in the WRF model. Bulletin of the American Meteorological Society, p. 2165–2170, 2004.

[35] Kain, J. S. The Kain – Fritsch convective parameterization: an update. Journal of applied meteorology, v. 43, n. 1, p. 170-181, 2004.

[36] Rogers, E. et al. National Oceanic and Atmospheric Administration Changes to the Ncep Meso Eta Analysis and Forecast System: Increase in resolution, new cloud microphysics, modified precipitation assimilation, modified 3DVAR analysis. NWS Tech. Proced. Bull, v. 488, p. 15, 2001.

[37] Nakanishi, M.; Niino, H. Development of an improved turbulence closure model for the atmospheric boundary layer. Journal of the Meteorological Society of Japan, v. 87, n. 5, p. 895–912, 2009.

[38] Nakanishi, M.; Niino, H. An improved Mellor-Yamada Level-3 model: Its numerical stability and application to a regional prediction of advection fog. Boundary-Layer Meteorology, v. 119, n. 2, p. 397–407, 2006.

[39] Olson, J. B. et al. A description of the Mynn-Edmf scheme and the coupling to other components in WRF – ARW. NOAA Technical Memorandum OAR GSD-61, NOAA. 2019.

[40] Han, J.; Pan, H. L. Revision of convection and vertical diffusion schemes in the Ncep Global Forecast System. Weather and Forecasting, v. 26, n. 4, p. 520–533, 2011.

[41] Kwon, Y. C.; Hong, S. Y. A mass-flux cumulus parameterization scheme across gray-zone resolutions. Monthly Weather Review, Vol. 145, n. 2, p. 583–598, 2017.

[42] Mattar, C.; Borvarán, D. Offshore wind power simulation by using WRF in the central coast of Chile. Renewable Energy, v. 94, p. 22–31, 2016.

[43] Ratjiranukool, P.; Ratjiranukool, S. Evaluating Wind Speed by WRF Model over Northern Thailand. Energy Procedia, v. 138, p. 1171–1176, 2017.

[44] Chai, T; Draxler, R. R. Root mean square error (RMSE) or mean absolute error (MAE)? - Arguments against avoiding RMSE in the literature. Geoscientific model development, v. 7, n. 3, p. 1247-1250, 2014.

[45] Hallak, R.; Pereira Filho, A. J. Methodology for performance analysis of convective system simulations in the metropolitan region of São Paulo with the ARPS model: sensitivity to variations with advection and data assimilation schemes. Revista Brasileira de Meteorologia (Brazilian Journal of Meteorology), v. 26, n. 4, p. 591-608, 2011.

[46] Amaral, B. M. Modelos Varx para Geração de Cenários de Vento e Vazão Aplicados a Comercialização de Energia (VARX Models for Generation of Wind and Flow Scenarios Applied to Energy Trading). Masters dissertation. Pontifical Catholic University of Rio de Janeiro - PUC Rio. Rio de Janeiro. 2011.

[47] Carvalho, D. et al. WRF wind simulation and wind energy production estimates forced by different reanalyses: Comparison with observed data for Portugal. Applied Energy, Vol. 117, p. 116-126, 2014.

[48] Saha, S. Response of the NMC MRF model to systematic-error correction within integration. Monthly weather review, v. 120, n. 2, p. 345-360, 1992.

[49] Cepel. Atlas of the Brazilian Wind Potential: Simulations 2013. Cepel/Electric Energy Research Center. Rio de Janeiro. 2017.

[50] Ferreira, A. G .; Da Silva Mello, N. G. Main atmospheric systems acting on the Northeast region of Brazil and the influence of the Pacific and Atlantic oceans on the region's climate. Brazilian Journal of Climatology, v. 1, n. 1, 2005.

[51] Reboita, M. S. et al. Precipitation regimes in South America: a literature review. Brazilian Journal of Meteorology, v. 25, n. 2, p. 185–204, 2010.

[52] NOAA. Cold & Warm Episodes by Season. NOAA/National Oceanic and Atmospheric Administration. Available at: https://origin.cpc.ncep.noaa.gov/products/analysis_ monitoring/ensostuff/ONI_v5.php. Accessed on 28 oct. 2020.

[53] Miranda, E. E. de; (Coord.). Brazil in Relief. Campinas: Embrapa Satellite Monitoring, 2005. Available at: http://www.relevobr.cnpm.embrapa.br. Accessed on 13 feb. 2019.

[54] Stull, R. B. An introduction to boundary layer meteorology. Atmospheric Sciences Library, Dordrecht: Kluwer, 1988, vol. 1, 1988.

[55] Santos, A. T. S. et al. Assessment of Wind resources in two parts of Northeast Brazil with the use of numerical models. Meteorological Applications, v. 23, n. 4, p. 563-573, 2016.

Research Article *Energy, Environment and Storage* (2022) 02-02:14-23

Energy, Environment and Storage

JournalHomepage: www.enenstrg.com

A Proposed Algorithm for Detecting Invisible Celestial Objects by Generalizing the Planck's Blackbody Radiation Law

Claude Ziad El-Bayeh

Department of Electrical Engineering, Bayeh Institute, 55 Kfar Saleh-Hay El Arbe Street, Amchit, Lebanon, ORCID: 0000-0002-8268-8878

ABSTRACT. Blackbody radiation was proposed by Planck to measure the temperature of a body by observing its electromagnetic waves spectrum. However, when it comes to massive objects such as stars, other factors can affect the emitted wavelength of the light from the body, such as gravitational field and doppler effect, which are caused not only by the star but also by the observer (i.e., Earth). Hence, predicting the surface temperature of a star by using only its radiation might not be accurate especially for massive stars. To solve the problem, and to give more accuracy to the measurement, this paper proposes an algorithm and a modification of the Plank's blackbody radiation theory by considering the impact of relativistic Doppler effect and the gravitational field of both, the emitter (i.e., star), and the receiver (i.e., Earth). For validation purposes, the proposed modification theory is compared to the original one proposed by Planck using four different case studies, (a) sun is considered as an emitter and the earth as the receiver; (b) a massive star is considered as an emitter and the earth as a receiver; (c) the earth is considered as an emitter and a massive star as a receiver; finally (d) two identical stars are considered as emitter and receiver, respectively. Results show that our proposed method works perfectly and gives more accurate results compared to the traditional Plank's theory since the impact of gravitational field and Doppler effect on the spectrum are considered.

Keywords: Blackbody radiation, General theory of relativity, Doppler Effect, Planck hypothesis, electromagnetic spectrum, gravitational field, Wien's displacement law.

Article History: Received: 09.02.2022; Revised: 11.03.2022; Accepted: 19.04.2022; Available online: 20.04.2022
Doi: https://doi.org/10.52924/GIAH1715

1. INTRODUCTION

In physics, blackbody radiation is a type of electromagnetic radiation within or surrounding a body in thermodynamic equilibrium with its environment or emitted by a blackbody (an opaque and non-reflective body) held at constant and uniform temperature. The radiation has a specific spectrum and intensity that depends only on the temperature of the body [1-2].A perfectly insulated enclosure that is in thermal equilibrium internally contains the body, will emit radiation through a hole made in its wall, providing the hole is small enough to have negligible effect upon the equilibrium [3-4].A blackbody at room temperature appears black, as most of the energy it radiates is infra-red and cannot be perceived by the human eye. At higher temperatures, blackbodies glow with increasing intensity and colors that range from dull red to blindingly brilliant blue-white as the temperature increases [5-8].Although planets and stars are neither in thermal equilibrium with their surroundings nor perfect blackbodies, blackbody radiation is used as a first approximation for the energy they emit. Black holes are near-perfect blackbodies, and it is believed that they emit blackbody radiation (called Hawking radiation), with a temperature that depends on their mass [9-12].The term *black body* was introduced by Gustav Kirchhoff in 1860 [3]. When used as a compound adjective, the term is typically written as hyphenated, for example, black-body radiation, but sometimes also as one word, as in blackbody radiation. Blackbody radiation is also called complete radiation or temperature radiation or thermal radiation.

On the other hand, Doppler Effect affects the wavelength of the electromagnetic wave which is demonstrated by Doppler. In addition, gravitational fields also affect the wavelength of the electromagnetic wave which was proved by the general theory of relativity [13-15]. Hence, it can be deduced that the electromagnetic spectrum emitted by a blackbody is affected by both, Doppler effect and the gravitational field, which are not considered in the original theory proposed by Planck. In fact, the blackbody theory works perfectly for small gravitational field and for small velocities of the object. It might not give accurate results when it comes to massive objects such as massive stars moving at high speed. It is important to mention that blackbody theory is applied to a

*Corresponding author: c.bayeh@hotmail.com

wide range of objects such as galaxies, black holes, stars, planets, human, molecules, and even atoms [16-27].

To fill the gap in the literature and to increase the accuracy of the measurement, this paper generalizes the blackbody radiation theory and Wien's displacement law by considering the impact of the Doppler effect and the gravitational field on the electromagnetic spectrum emitted by the blackbody. In addition, the proposed theory can be implemented in other fields of physics as in [28-35].

This paper is organized as follows: The second section presents backgrounds on the blackbody radiation law and Planck's hypothesis, the general Doppler effect, and the gravitational field. In section 3, the author proposes a general theory of the blackbody radiation.In the fourth section, results are presented. Finally,a conclusion is shown in section five.

2. BACKGROUND OF EXISTING THEORIES

2.1. Blackbody Radiation and Planck's Hypothesis

According to the blackbody radiation theory, any object at any temperature emits electromagnetic waves in the form of thermal radiation from its surface.The characteristics of this radiation depend on the temperature and properties of the object's surface. Studies showed that the radiation consists of a continuous distribution of wavelengths from all portions of the electromagnetic spectrum. If the object is at room temperature, the wavelengths of thermal radiation are mainly in the infrared region; hence, the radiation is not detected by the human eyes. For this reason, infrared cameras are widely deployed in dark to detect movements and to see objects, animals and humans. As the surface temperature of the object increases, the object eventually begins to glow visibly red. At sufficiently high temperatures, the glowing object appears white; at very high temperature it appears blue and so on. A blackbody is an ideal system that absorbs all radiation incidents on it, and emits electromagnetic radiation on a large spectrum, which is called blackbody radiation. **Fig. 1** and **Fig. 2**show how the intensity of blackbody radiation varies as a function of the temperature and wavelength based on classical and the Planck's theories, respectively, [3]. As an example, for a temperature of 5000K, the spectral radiance using classical theory does not converge for small wavelengths as it appears in **Fig. 1**. However, Plank corrected the equation in which the spectral radiance converges for any temperature as in **Fig. 2**.

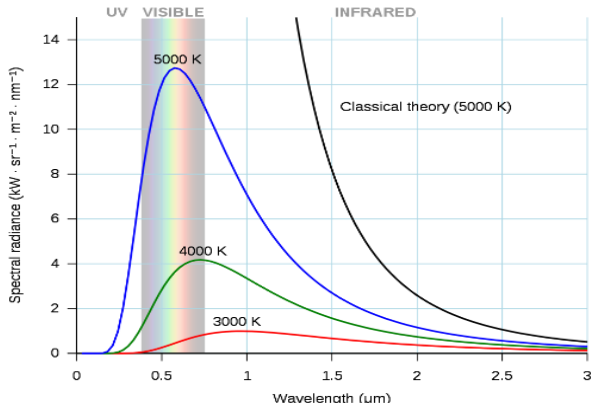

Fig. 1. Intensity as a function of the wavelength and temperature of a blackbody using classical theory.

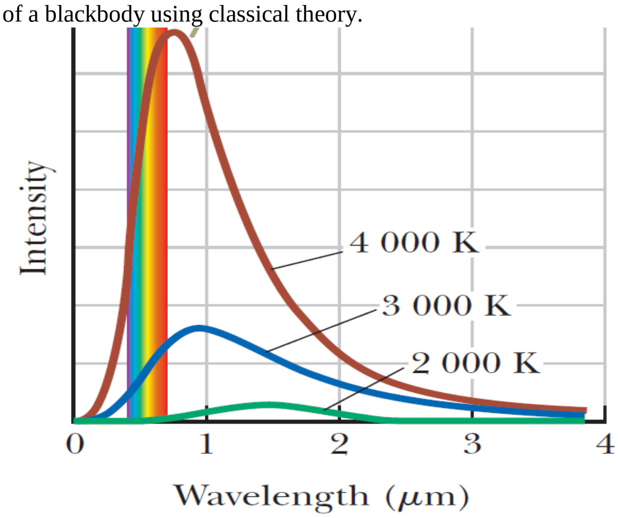

Fig. 2. Intensity as a function of the wavelength and temperature of a blackbody using Plank's theory. Visible light spectrum is between 0.4 and 0.8μm [3].

According to the classical theory, the total power of the emitted radiation increases with temperature and known as Stefan's law. This behavior is expressed in Eq. (1), [3]. Where, P is the power of electromagnetic waves radiated from the surface of the object, [W].$\sigma$is the Stefan–Boltzmann constant equal to $5.6696 \cdot 10^{-8} W/m^2K^4$.$A$ is the surface area of the object, [m^2].T is the surface temperature in Kelvin.e is the emissivity; it is equal to $e = 1$for a blackbody.

$$P = \sigma A e T^4 \tag{1}$$

The peak of the wavelength distribution shifts to shorter wavelengths as the temperature increases. This behavior is described by Eq. (2) and called Wien's displacement law [3]. Where λ_{max} is the wavelength at which the curve peaks.T is the absolute temperature of the object's surface emitting the radiation.

$$\lambda_{max} T = 2.898 \cdot 10^{-3} m \cdot K \tag{2}$$

The classical theory could not explain the radiation at very high temperature as in Figure 1. Therefore, Planck improved the theory by introducing Eq. (3), [3]. This mathematical expression for the wavelength distribution agrees remarkably well with the experimental results as presented in Figure 2. It includes the parameter h, which Planck adjusted so that his curve matched the experimental data at all wavelengths. The value of this parameter is found to be independent of the material of which the blackbody is made and independent of the temperature. It is a fundamental constant of nature, and it is equal to $h = 6.626 \cdot 10^{-34} J \cdot s . k_B$is theBoltzmann's constant, $k_B = 1.38064852 \cdot 10^{-23} m^2 \cdot kg \cdot s^{-2} K^{-1}$.

$$I(\lambda, T) = \frac{2\pi hc^2}{\lambda^5 \left(e^{\frac{hc}{\lambda k_B T}} - 1\right)} \tag{3}$$

In fact, the Planck's hypothesis is a very good approach to explain the radiation from a blackbody. It can work perfectly for bodies with weak gravitational fieldand moving at a very low speed. However, for massive bodies such as supper massive stars and quasars, the gravitational field is very strong and can affect the length of the electromagnetic wave. As an example, the emitted light from a massive blackbody is shifted to a lower frequency when it goes out the body,then it is shifted to a higher frequency when it is approaching an observer with a strong gravitational field. The same for the Doppler Effect, when the blackbody and the observer are approaching to each other, the electromagnetic wave is shifted to a higher frequency; when they are running away from each other, the electromagnetic wave is shifted to a lower frequency. From this place, it is necessary to also define the Doppler effect and the gravitational field in the next subsections.

2.2. Relativistic Doppler effect in two-dimensional space

The doppler effect is used to measure the speed of an object in space. In case the source approaches the observer, the measured frequency is increased, and the wavelength is reduced. In case the source is moving away from the observer, the frequency is reduced, and the wavelength is increased. The general doppler effect in a two-dimensional space is described by Eq. (4), [3].Where, f_R is the frequency received by the receiver (observer).V_w is the velocity of the wave, in our case, the wave is an electromagnetic radiation, and the velocity is equal to the velocity of the light $V_w = c$.V_R is the velocity of the receiver (observer).θ_R is the angle formed between the vector velocity of the receiver and the axis source-receiver (SR).V_S is the velocity of the source, in our case, it is the Blackbody.θ_S is the angle formed between the vector velocity of the source and the axis source-receiver (SR).f_S is the frequency emitted by the source (blackbody).**Fig. 3** presents the vectors of the source and the observer (receiver).

$$f_R = \left(\frac{V_w + V_R \cos(\theta_R)}{V_w - V_S \cos(\theta_S)}\right) f_S \tag{4}$$

The relativistic frequency f_R according to the special relativity of Einstein can be written as in Eq. (5).

$$f_R = f_S \left(\frac{V_w + V_R \cos(\theta_R)}{V_w - V_S \cos(\theta_S)}\right) \sqrt{\frac{1 - \left(\frac{V_S}{V_w}\right)^2}{1 - \left(\frac{V_R}{V_w}\right)^2}} \tag{5}$$

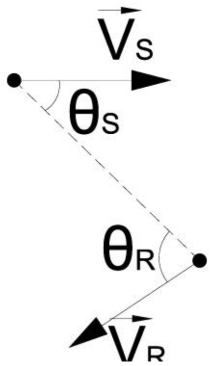

Fig. 3. Relationship between two vectors $\overrightarrow{V_S}(|V_S|, \theta_S)$ and $\overrightarrow{V_R}(|V_R|, \theta_R)$in a 2D space.

However, in this paper, we are interested in finding a relationship between the wavelengths of the receiver and the source instead of the frequency. To do so, Eq. (6) is used which presents the relationship between the frequency and the wavelength of the light. Then, by substituting it in Eq. (4), Eq. (7) is obtained. λ_R is relativistic wavelength measured by the receiver, and λ_S is the real relativistic wavelength emitted by the source. In case the receiver and the source are approaching to each other, then $\lambda_R \leq \lambda_S$, if they are moving away, then $\lambda_R \geq \lambda_S$.

$$f = \frac{c}{\lambda} \tag{6}$$

$$\lambda_R = \lambda_s \left(\frac{c - V_S \cos(\theta_S)}{c + V_R \cos(\theta_R)}\right) \sqrt{\frac{1 - \left(\frac{V_R}{c}\right)^2}{1 - \left(\frac{V_S}{c}\right)^2}} \tag{7}$$

2.3. Gravitational redshift

According to the general theory of relativity [7], light is affected by the gravitational field of an object (such as a star). Hence, if the light is leaving the star, its wavelength becomes larger, and it is redshifted as depicted in **Fig. 4**. This phenomenon is called gravitational redshift and expressed as in Eq. (8). Where, f_S and f_R are the frequencies of the light at the source and receiver; G is the Newton's gravitational constant ($G = 6.6738 \cdot 10^{-11} Nm^2/kg^2$); M_S is the mass of the source; R_S is the radius of the source (in case of a spherical shape); c is the velocity of the light in a vacuum ($c = 299792458 m/s$). When an electromagnetic wave exits from a massive body, there is a reduction in its energy. Its frequency is also reduced due to the electromagnetic radiation propagating in opposition to the gravitational gradient. There also exists a corresponding blueshift when electromagnetic radiation propagates from an area of a weaker gravitational field to an area of a stronger gravitational field.

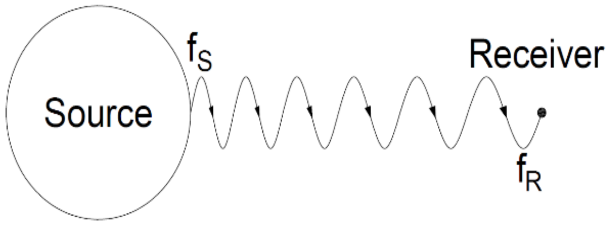

Fig. 4. Example of a gravitational redshift when an electromagnetic signal is emitted by the source toward the received, where $f_s > f_R$.

$$\frac{f_S - f_R}{f_S} = \frac{GM_S}{R_S c^2} \tag{8}$$

Since we are interested in calculating the wavelength, Eq. (6) is substituted in Eq. (8). Hence, the wavelength relationship between the source and the receiver is presented in Eq. (9).

$$\lambda_R = \frac{\lambda_S}{\left(1 - \frac{GM_S}{R_S c^2}\right)} \tag{9}$$

On the other hand, if the light is approaching to a massive receiver, the photon gains energy and increases its frequency; hence, its wavelength is reduced as described in Eq. (10) and depicted in **Fig. 5**. Where, M_R is the mass of the receiver and R_R is the radius of the receiver.

$$\lambda_R = \lambda_S \left(1 - \frac{GM_R}{R_R c^2}\right) \tag{10}$$

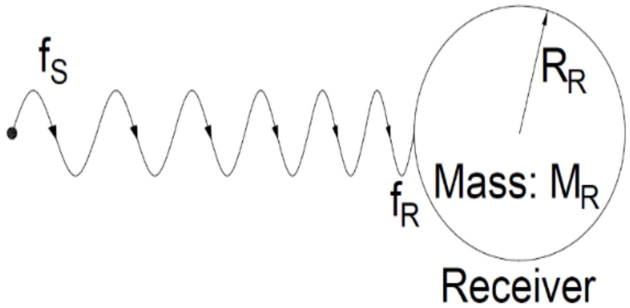

Fig. 5. Example of a gravitational redshift when an electromagnetic signal is emitted by the source toward the received, where $f_S < f_R$.

3. PROPOSED ALGORITHM FOR DETECTING INVISIBLE CELESTIAL OBJECTS

3.1. Proposed General Blackbody Radiation Theory

In this paper, the blackbody radiation theory is generalized, in which the impact of relativistic doppler effect and the gravitational redshift on the wavelength are considered. **Fig. 6** presents the variation of the wavelength passing from the source to the receiver considering the movement of both objects, their speed, mass, and radius. Planck postulated that "*The radiation has a specific spectrum and intensity that depends only on the temperature of the body*". However, since the relativistic doppler effect and gravitational redshift phenomena affect the wavelength of light received by the receiver, the postulate should be corrected as it will appear later in this paper.

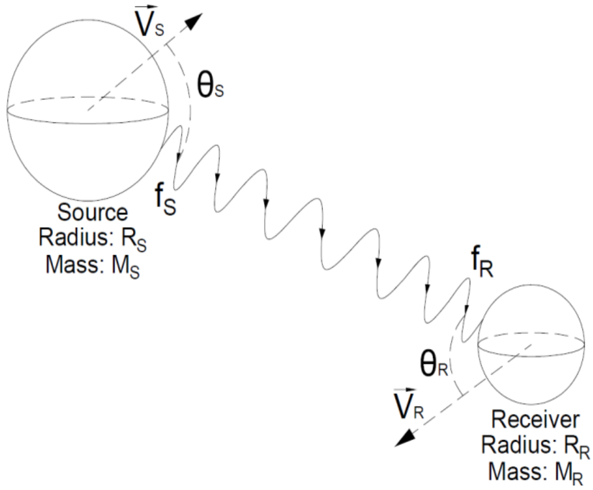

Fig. 6. Variation of the wavelength considering relativistic doppler effect and gravitational redshift.

Eq. (11) presents the relationship between the wavelength emmitted by the source and received by the receiver, which takes into account the gravitational redshift and the relativistic doppler effect.This relationship is important in studyingthe blackbodies and theirwavelength spectrum since it gives more accurate results especially for massive objects compared to the equation proposed by Planck. Equations (12) and (13) present the intensity of the electromagnetic spectrum of the blackbody at the source ($I_S(\lambda_S, T)$) and receiver ($I_R(\lambda_R, T)$) levels, respectively. Once the intensity at the receiver level is measured, it becomes easier to calculate the intensity at the source level. Hence, it is possible to calculate the missing information of the blackbody such as its speed, moving direction, surface's temperature, mass, and distance between the source and the receiver.

$$\lambda_R = \lambda_S \frac{\left(1 - \frac{GM_R}{R_R c^2}\right)}{\left(1 - \frac{GM_S}{R_S c^2}\right)} \left(\frac{c - V_S \cos(\theta_S)}{c + V_R \cos(\theta_R)}\right) \sqrt{\frac{1 - \left(\frac{V_R}{c}\right)^2}{1 - \left(\frac{V_S}{c}\right)^2}} \tag{11}$$

$$I_S(\lambda_S, T) = \frac{2\pi h c^2}{\lambda_S^5 \left(e^{\frac{hc}{\lambda_S k_B T}} - 1\right)} \tag{12}$$

$$I_R(\lambda_R, T) = \frac{2\pi h c^2 \left[\frac{\lambda_R}{\left(\frac{\left(1 - \frac{GM_R}{R_R c^2}\right)}{\left(1 - \frac{GM_S}{R_S c^2}\right)}\left(\frac{c - V_S \cos(\theta_S)}{c + V_R \cos(\theta_R)}\right)\sqrt{\frac{1 - \left(\frac{V_R}{c}\right)^2}{1 - \left(\frac{V_S}{c}\right)^2}}\right)}\right]^{-5}}{\left(\exp\left(\frac{hc\left(\frac{\left(1 - \frac{GM_R}{R_R c^2}\right)}{\left(1 - \frac{GM_S}{R_S c^2}\right)}\left(\frac{c - V_S \cos(\theta_S)}{c + V_R \cos(\theta_R)}\right)\sqrt{\frac{1 - \left(\frac{V_R}{c}\right)^2}{1 - \left(\frac{V_S}{c}\right)^2}}\right)}{\lambda_R k_B T}\right) - 1\right)} \tag{13}$$

The same procedure can be applied to the Wien's displacement law that determines the wavelength for the maximum intensity, as in Eq. (14). The electromagnetic wave with the highest intensity measured by the source and the receiver are defined in Equations (15) and (16), respectively. Where, $\varepsilon = 2.898 \cdot 10^{-3} m \cdot K$.

$$\lambda_{max} T = \varepsilon \tag{14}$$

$$\lambda_S^{Max} = \frac{\varepsilon}{T} \tag{15}$$

$$\lambda_R^{Max} = \frac{\varepsilon}{T} \frac{\left(1 - \frac{GM_R}{R_R c^2}\right)}{\left(1 - \frac{GM_S}{R_S c^2}\right)} \left(\frac{c - V_S \cos(\theta_S)}{c + V_R \cos(\theta_R)}\right) \sqrt{\frac{1 - \left(\frac{V_R}{c}\right)^2}{1 - \left(\frac{V_S}{c}\right)^2}} \tag{16}$$

Whenever λ_R^{Max} and I_R^{Max} are measured, it becomes easier to calculate λ_S^{Max} and I_S^{Max}, in which Eq. (17) represents the λ_S^{Max} as a function of $I_R^{Max}(\lambda_R^{Max}, T)$ and λ_R^{Max}, and Eq. (18) represents $I_S^{Max}(\lambda_S^{Max}, T)$ as a function of $I_R^{Max}(\lambda_R^{Max}, T)$ and λ_R^{Max}.

$$\lambda_S^{Max} = \left(\frac{I_R^{Max}(\lambda_R^{Max}, T) \cdot \left(e^{\frac{hc}{\varepsilon k_B}} - 1\right)}{2\pi h c^2} \right)^{-\frac{1}{5}} \tag{17}$$

$$I_S^{Max}(\lambda_S, T) = I_R^{Max}(\lambda_R^{Max}, T) \tag{18}$$

3.2. Proposed algorithm to detect invisible celestial objects

Invisible objects in the universe are also considered as blackbodies that emit a spectrum of light in which the wavelength of the maximum intensity is not located within the visible spectrum.The visible spectrum or optical spectrum is the portion of the electromagnetic spectrum that is visible to the human eye. Electromagnetic radiation in this range of wavelengths is called visible light or simply light. A typical human eye will respond to wavelengths from about 380 to about 750 nanometers [30]. In terms of frequency, this corresponds to a band in the vicinity of 400–790 THz. These boundaries are not sharply defined and may vary per individual. Under optimal conditions these limits of human perception can extend to 310 nm (UV) and 1100 nm (NIR) [31]. Therefore, it is not easy to notice the celestial objects and to know more about their characteristics such as mass, volume, radius, density, etc. In this section, an algorithm is proposed to detect invisible celestial objects especially stars from a distant by detecting their maximum wavelength (λ_R^{Max}) and the corresponding maximum spectrum intensity ($I_R^{Max}(\lambda_R^{Max}, T)$).

In this section, it is important to focus on the measurable parameters that can be detected by instruments from the receiver's viewpoint such as the telescope. First, it is important to mention what are the parameters that can be determined before starting the calculation.

Table 1 presents the constants and variables of the equations from (11) to (18). Some of them are known, others are to be measured, determined, or calculated.

Eq. (19) is deduced from Eq. (11), in which M_S/R_s is written as a function of other known parameters. M_S can be known since it is possible to measure the impact of the celestial object on its environment. Therefore, R_S can be calculated as in Eq. (20), and it is also possible to determine the density of the celestial object as per the Eq. (21). It can be noted that the density of the celestial object is not constant and might change based on its velocity, and the velocity of the observer.

Table 1. Data set needed.

Parameter	Status	Value
c	Constant	$299792458 m/s$
ε	Constant	$2.898 \cdot 10^{-3} m \cdot K$
G	Constant	$6.6738 \cdot 10^{-11} Nm^2/Kg^2$
h	Constant	$6.626 \cdot 10^{-34} J \cdot s$
k_B	Constant	$1.38064852 \cdot 10^{-23} J \cdot K^{-1}$
λ_R^{Max}	Detected	Only after measurement
I_R^{Max}	Detected	Only after measurement
M_R	Measured	Only after measurement
R_R	Measured	Only after measurement
V_R	Measured	Only after measurement
θ_R	Measured	Only after measurement
V_S	Measured	Only after measurement
θ_S	Measured	Only after measurement
λ_S^{Max}	Calculated	Eq. (17)
I_S^{Max}	Calculated	Eq. (18)
T	Calculated	$T = \varepsilon/\lambda_S^{Max}$
M_S	Unknown	To be calculated
R_S	Unknown	To be calculated

Begin

Define constants:
$c = 299792458 m/s$; $\varepsilon = 2.898 \cdot 10^{-3} m \cdot K$
$G = 6.6738 \cdot 10^{-11} Nm^2/Kg^2$; $h = 6.626 \cdot 10^{-34} J \cdot s$
$k_B = 1.38064852 \cdot 10^{-23} J \cdot K^{-1}$

Input receiver's data (observer such as Earth):
-Mass of the receiver (M_R)
-Radius of the receiver (R_R), or volume of the receiver
-Velocity of the receiver (V_R)
-Travelling angle of the receiver (θ_R)

Measure source's data (celestial object):
-Velocity of the source (V_S)
-Travelling angle of the source with respect to the receiver (θ_S)

Detect the radiation from the source received by the receiver:
-Maximum wavelength (λ_R^{Max})
-Maximum intensity of the spectrum ($I_R^{Max}(\lambda_R^{Max}, T)$)

Calculate the original radiation emitted by the source:
-Maximum wavelength: $\lambda_S^{Max} = \left(\frac{I_R^{Max}(\lambda_R^{Max}, T) \cdot \left(e^{\frac{hc}{\varepsilon k_B}} - 1\right)}{2\pi h c^2} \right)^{-\frac{1}{5}}$
-Maximum spectrum intensity: $I_S^{Max}(\lambda_S^{Max}, T) = I_R^{Max}(\lambda_R^{Max}, T)$
-Blackbody's temperature: $T = \varepsilon/\lambda_S^{Max}$

Calculate the ratio M_S/R_S:

$$\frac{M_S}{R_S} = \frac{c^2}{G}\left[1 - \frac{\lambda_S^{Max}}{\lambda_R^{Max}}\left(1 - \frac{GM_R}{R_R c^2}\right)\left(\frac{c - V_S\cos(\theta_S)}{c + V_R\cos(\theta_R)}\right)\sqrt{\frac{1-\left(\frac{V_R}{c}\right)^2}{1-\left(\frac{V_S}{c}\right)^2}}\right]$$

Predict M_S or R_S based on the observation of the object in its surrounding:
In case M_S is determined, calculate R_S:

$$R_S = \frac{M_S}{\frac{c^2}{G}\left[1 - \frac{\lambda_S^{Max}}{\lambda_R^{Max}}\left(1 - \frac{GM_R}{R_R c^2}\right)\left(\frac{c - V_S\cos(\theta_S)}{c + V_R\cos(\theta_R)}\right)\sqrt{\frac{1-\left(\frac{V_R}{c}\right)^2}{1-\left(\frac{V_S}{c}\right)^2}}\right]}$$

In case R_S is determined, calculate M_S:

$$M_S = R_S\frac{c^2}{G}\left[1 - \frac{\lambda_S^{Max}}{\lambda_R^{Max}}\left(1 - \frac{GM_R}{R_R c^2}\right)\left(\frac{c - V_S\cos(\theta_S)}{c + V_R\cos(\theta_R)}\right)\sqrt{\frac{1-\left(\frac{V_R}{c}\right)^2}{1-\left(\frac{V_S}{c}\right)^2}}\right]$$

Calculate the density of the blackbody:

$$\rho_S = \frac{3}{4\pi R_S^2}\frac{c^2}{G}\left[1 - \frac{\lambda_S^{Max}}{\lambda_R^{Max}}\left(1 - \frac{GM_R}{R_R c^2}\right)\left(\frac{c - V_S\cos(\theta_S)}{c + V_R\cos(\theta_R)}\right)\sqrt{\frac{1-\left(\frac{V_R}{c}\right)^2}{1-\left(\frac{V_S}{c}\right)^2}}\right]$$

End

Fig. 7. Proposed algorithm fordetecting invisible celestial objects and calculating all their necessary data.

$$\frac{M_S}{R_S} = \frac{c^2}{G}\left[1 - \frac{\lambda_S^{Max}}{\lambda_R^{Max}}\left(1-\frac{GM_R}{R_R c^2}\right)\left(\frac{c - V_S\cos(\theta_S)}{c + V_R\cos(\theta_R)}\right)\sqrt{\frac{1-\left(\frac{V_R}{c}\right)^2}{1-\left(\frac{V_S}{c}\right)^2}}\right] \tag{19}$$

$$R_S = \frac{M_S}{\frac{c^2}{G}\left[1 - \frac{\lambda_S^{Max}}{\lambda_R^{Max}}\left(1-\frac{GM_R}{R_R c^2}\right)\left(\frac{c - V_S\cos(\theta_S)}{c + V_R\cos(\theta_R)}\right)\sqrt{\frac{1-\left(\frac{V_R}{c}\right)^2}{1-\left(\frac{V_S}{c}\right)^2}}\right]} \tag{20}$$

$$\rho_S = \frac{3}{4\pi R_S^2}\frac{c^2}{G}\left[1 - \frac{\lambda_S^{Max}}{\lambda_R^{Max}}\left(1-\frac{GM_R}{R_R c^2}\right)\left(\frac{c - V_S\cos(\theta_S)}{c + V_R\cos(\theta_R)}\right)\sqrt{\frac{1-\left(\frac{V_R}{c}\right)^2}{1-\left(\frac{V_S}{c}\right)^2}}\right] \tag{21}$$

Fig. 7 Presents the algorithm used to detect the invisible celestial object and calculate all its necessary information.

3.3. Programming in MATLAB

The proposed algorithm and the general blackbody radiation are programmed in MATLAB for simulation purposes. The code is written hereafter, in which it asks the user to put the needed parameters and calculates the Wien's displacement law for both the source and the receiver. In addition, it plots the "spectral radiance of the blackbody" with respect to the receiver and the source.

4. RESULTS AND DISCUSSIONS

4.1 Assumptions

In order to show the significance of this study, the proposed general blackbody radiation is compared to the original one by Planck for four different case scenarios.

- Case 1: the sun is considered as a source (blackbody) and the earth as a receiver. The following data are given:
  - Mass of the sun $M_S = 1.989 \cdot 10^{30}kg$
  - Radius of the sun $R_S = 6.963 \cdot 10^8 m$
  - Velocity of the sun$V_S = 0m/s$
  - Angle of movement: $\theta_S = 0^0$
  - Mass of the earth $M_R = 5.9736 \cdot 10^{24}kg$
  - Radius of the earth $R_R = 6.371 \cdot 10^\wedge 6m$
  - Velocity of the earth $V_R = 29.78 \cdot 10^3 m/s$
  - Angle of movement: $\theta_R = 90^0$
- Case 2: A star is considered as a source and the earth as a receiver.The following data are given:
  - Mass of the star $M_S = 2 \cdot 10^{35}kg$
  - Radius of the star $R_S = 2.97 \cdot 10^8 m$
  - Velocity of the star$V_S = 0m/s$
  - Angle of movement: $\theta_S = 0^0$
  - Mass of the earth $M_R = 5.9736 \cdot 10^{24}kg$
  - Radius of the earth $R_R = 6.371 \cdot 10^\wedge 6m$
  - Velocity of the earth $V_R = 0m/s$
  - Angle of movement: $\theta_R = 0^0$

```
clc;clear;closeall; %Clear all previous data on MATLAB
for section=1:1%Physical Constants
    h=6.626e-34;%Planck's constant
    c=299792458;%velocity of the light
    KB=1.3806488e-23;%Boltzmann constant
    G=6.6738e-11;%Newton's gravitational constant
    T=5000;%Temperature of the blackbody in Kelvin
end
for section=1:1%Input data
fprintf('-----General Blackbody Radiation-----\n');
fprintf('------------------------------------\n');
    repeat='y';
while repeat=='y'
for section1=1:1%Input Data from the user
Ms_Input='Mass of the Blackbody: Ms=';
Ms=input(Ms_Input);
Rs_Input='Radius of the Blackbody: Rs=';
    Rs=input(Rs_Input);
Vs_Input='Velocity of the Blackbody: Vs=';
    Vs=input(Vs_Input);
As_Input='Movement angle of the Blackbody: As=';
    As=input(As_Input);
Mr_Input='Mass of the Receiver: Mr=';
Mr=input(Mr_Input);
Rr_Input='Radius of the Receiver: Rr=';
    Rr=input(Rr_Input);
Vr_Input='Velocity of the Receiver: Vr=';
Vr=input(Vr_Input);
Ar_Input='Movement angle of the Receiver: Ar=';
Ar=input(Ar_Input);
end
for section1=1:1%Calculation
    a1=1-G*Mr/(Rr*c^2);
    a2=1-G*Ms/(Rs*c^2);
    a3=(c-Vs*cos(As*pi/180))/(c+Vr*cos(Ar*pi/180));
gamma=sqrt((1-(Vr/c)^2)/(1-(Vs/c)^2));
a4=a1/a2*a3*gamma;
Ratio_LambdaR_to_LambdaS=a4
Ratio_Wavelength_R_to_Wavelength_S=a4
Wavelength_S=2.898e-3./T
Wavelength_R=2.898e-3./T.*a4
    x=0:0.5e-7:4e-6;
    Is=(2*pi*h*c^2)./(x.^5.*(exp((h*c)./(x.*KB.*T))-1));
Ir=(2*pi*h*c^2)./((x./a4).^5.*(exp((h*c)./...
       ((x./a4).*KB.*T))-1));
end
for section1=1:1%Visible Spectrum
%Minimum visible light
y1=0;y2=5e13;x1=380e-9;x2=381e-9;
b1=(y2-y1)/(x2-x1); b2=y1-b1*x1;
y_red=b1*x+b2;
%Maximum visible light
y1=0;y2=5e13;x1=700e-9;x2=701e-9;
b1=(y2-y1)/(x2-x1); b2=y1-b1*x1;
y_blue=b1*x+b2;
end
for section1=1:1%Plot Data
    figure('name','Intensity of the blackbody')
xmin=0;xmax=max(x);ymin=0;ymax=max(Ir).*1.05;
FontSize=14;
    plot(x,Ir,'-*','Color',[1,0.5,0],'LineWidth',1);
    hold on;
    plot(x,Is,'-D','Color',[0,.5,1],'LineWidth',1);
    hold on;
    plot(x,y_red,'-','Color',[1,0,0],'LineWidth',2);
    hold on;
    plot(x,y_blue,'-','Color',[0,0,1],'LineWidth',2);
    hold on;
    legend('Ir','Is','Minimum visible light',...
'Maximum visible light',...
'Location','southeast','Orientation','vertical');
axis([xminxmaxyminymax])
xlabel('Wavelength [\mum]');
ylabel('Spectral Radiance');
    title('Spectral Radiance of the blackbody');
ax = gca; ax.FontSize = FontSize;
grid on;
end
for section1=1:1%Ask for repetition
fprintf('Do you want to repeat ?\nPress y for ''Yes'' or
            any key for ''No''\n');
    repeat=input('Y/N=','s'); %string input
clc; close all;
end
end%End while
end
```

- Case 3: the earth is emitting radiation to a star. In this case, the earth is considered as a blackbody and the star as a receiver.The following data are given:
    - Mass of the earth $M_S = 5.9736 \cdot 10^{24} kg$
    - Radius of the earth $R_S = 6.371 \cdot 10\text{^}6m$
    - Velocity of the earth $V_R = 0m/s$
    - Angle of movement: $\theta_R = 0^0$
    - Mass of the star $M_R = 3 \cdot 10^{35} kg$
    - Radius of the star $R_R = 2.97 \cdot 10^8 m$
    - Velocity of the star$V_R = 0m/s$
    - Angle of movement: $\theta_R = 0^0$

- Case 4: Binary massive stars are considered with the following data:
    - Mass of the star 1:$M_S = 3 \cdot 10^{35} kg$
    - Radius of the star 1:$R_S = 2.97 \cdot 10^8 m$
    - Velocity of the star 1:$V_S = 10^6 m/s$
    - Angle of movement of star 1: $\theta_S = 0^0$
    - Mass of the star 2:$M_R = 3 \cdot 10^{35} kg$
    - Radius of the star 2:$R_R = 2.97 \cdot 10^8 m$
    - Velocity of the star 2:$V_R = 10^6 m/s$
    - Angle of movement of star 2: $\theta_R = 180^0$

- Physical constants
    - Newton's gravitational constant$G = 6.6738 \cdot 10^{-11} Nm^2/kg^2$
    - Speed of light in a vacuum: $c = 299792458m/s$
    - Planck constant: $h = 6.626 \cdot 10^{-34} J \cdot s$
    - Boltzmann constant:$k_B = 5.6696 \cdot 10^{-8} W/m^2K^4$
- Other parameters: $T = 5000K$

In the following subsections, the Wien's displacement lawand the Spectral Radiance of the blackbody are calculated from the viewpoint of the receiver (using the Planck's blackbody radiation theory) and the source (using the proposed general blackbody radiation theory in this paper).

4.2. Case 1

In this case, the sun is considered as a source and the earth as a receiver. Real data are provided in **Table 2** in order to show the difference between the proposed model in this paper and the one proposed by Planck. Planck's theory measures the blackbody radiation as it is received by the observer (such as the earth in this case) neglecting other factors, such as, the mass, radius, velocity, and the angle of movement of both the source and the receiver. Fig. 8 presents a comparison between the spectral radiance of the blackbody from the perspective of the receiver (Planck's theory) and the source (proposed theory in this paper) for the case 1. It can be remarked that both spectrums are almost identical since the masses of the sun and the earth do not highly deform the wavelength of the light. Therefore, both methods give almost the same results.

Table 2. Summary data for case 1.

Data	Source	Receiver
Mass	1.989e30	5.9736e24
Radius	6.963e8	6.371e6
Velocity	0	2.978e4
Angle of movement	0	90

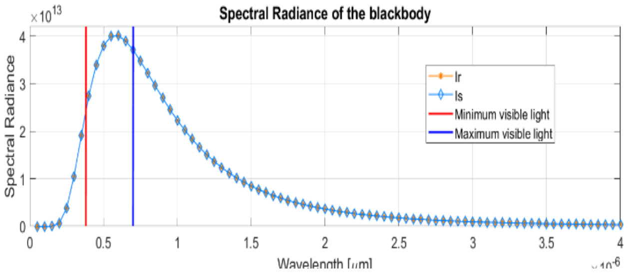

Fig. 8. Comparison between the spectral radiance of the blackbody from the perspective of the receiver (Planck's theory) and the source (proposed theory in this paper) for the case 1.

4.3. Case 2

In this case, a massive star is considered (100,553 times massive than the sun) as a source and the earth as a receiver. Data are provided in **Table 3** in order to show the difference between the proposed model in this paper and the one proposed by Planck. Fig. **9** presents a comparison between the spectral radiance of the blackbody from the perspective of the receiver (Planck's theory) and the source (proposed theory in this paper) for the case 2. It can be remarked that there is a difference between both spectrums, in which the one measured at the source level (sun) is visible, while it is not from the earth since thespectrum is shifted to the right side.

Table 3. Summary data for case 2.

Data	Source	Receiver
Mass	2e35	5.9736e24
Radius	2.97e8	6.371e6
Velocity	0	0
Angle of movement	0	0

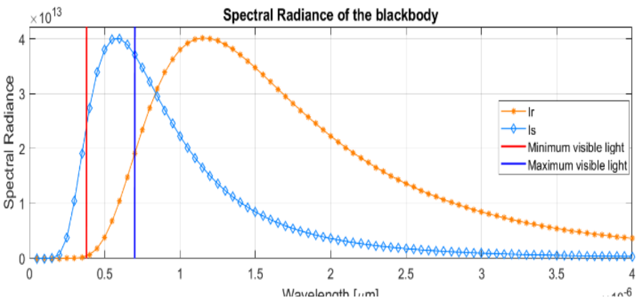

Fig. 9. Comparison between the spectral radiance of the blackbody from the perspective of the receiver (Planck's theory) and the source (proposed theory in this paper) for the case 2.

4.4. Case 3

In this case, the inverse scenario of case 2 is studied in which the earth is considered as a source and it emits light which is received by a massive star (150,829 times massive than the sun). Data are provided in **Table 4** in order to show the difference between the proposed model in this paper and the one proposed by Planck. **Fig. 10**presents a comparison between the spectral radiance of the blackbody from the perspective of the receiver (Planck's theory) and the source (proposed theory in this paper) for the case 3. It can be remarked that there is a difference between both spectrums, in which the one measured at the source level (earth) is visible, while it is not from the receiver since thespectrum is shifted to the left side.

Table 4. Summary data for case 3.

Data	Source	Receiver
Mass	5.9736e24	3e35
Radius	6.371e6	2.97e8
Velocity	0	0
Angle of movement	0	0

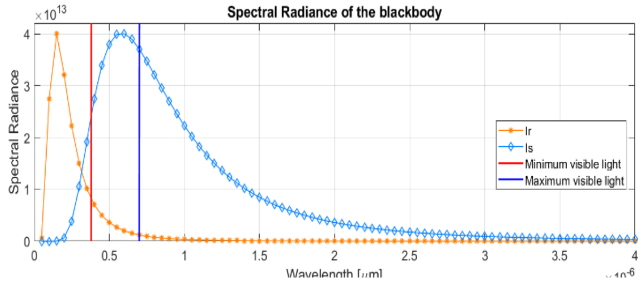

Fig. 10. Comparison between the spectral radiance of the blackbody from the perspective of the receiver (Planck's theory) and the source (proposed theory in this paper) for the case 3.

4.5. Case 4

In this case, two identical stars with the same mass, radius, velocity, and direction are examined. The star 1 has an angle equal to zero which means that it is approaching the second star. However, the angle of the second star is 180 degrees which means that it is going away from the first star. In another meaning, the distance between the two stars do not change. Data are provided in **Table 5** in order to show the difference between the proposed model in this paper and the one proposed by Planck. **Fig. 11**presents a comparison between the spectral radiance of the blackbody from the perspective of the receiver (Planck's theory) and the source (proposed theory in this paper) for the case 4. It can be remarked that there both spectrums are identical even if they are massive stars. The reason is that when the light is emitted by star 1, it becomes redshifted, and its wavelength is increased. However, when the light approaches star 2, since it has the same characteristics of star 1, the light is shifted to the left side of the spectrum (blue-shifted). Hence, the aggregated difference in the wavelength becomes equal to "0". Hence, both methods give same results and spectrums. In another meaning, if we want to see any distant massive object in the space even a black hole, we should have the same characteristics. Hence, the question that arises, can we see all black holes in the universe if we live in a black hole?

Table 5. Summary data for case 4.

Data	Source	Receiver
Mass	3e35	3e35
Radius	2.97e8	2.97e8
Velocity	1e6	1e6
Angle of movement	0	180

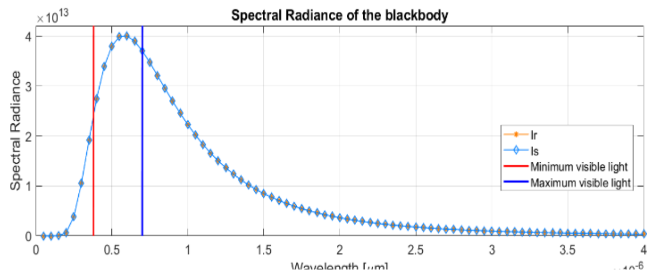

Fig. 11. Comparison between the spectral radiance of the blackbody from the perspective of the receiver (Planck's theory) and the source (proposed theory in this paper) for the case 4.

In conclusion, the proposed method could explain why we are not able to see black holes, which are massive objects in space (and maybe with tiny diameters), but they are not visible since the emitted light could be highly shifted and may not be easy to be detect. These massive objects exert huge gravitational field to their surrounding and could explain why the stars on the boarder of the galaxy do not obey Kepler's laws. In fact, Kepler's law mentioned that "based on the distribution of matter in the galaxy, the speed of an object in the outer part of the galaxy would be smaller than that for objects closer to the center, just like for the planets of the solar system."That is notwhat is observed in reality; scientists showed that for objects outside the central core of the galaxy, the curve of speed versus distance from the center of the galaxy is approximately flat rather than decreasing at larger distances. Therefore, these objects (including our own Solar System in the Milky Way) are rotating faster than can be accounted for by gravity due to the visible galaxy. This surprising result means that there must be additional mass in a more extended distribution, causing these objects to orbit so fast, and has led scientists to propose the existence of dark matter.

5. CONCLUSION

This paper generalizes the "blackbody radiation law" and the "Wien's displacement law" in which it considers many factors such as the mass, radius, velocity, angle of movement, and the surface temperature of both the source and the receiver. All these factors can affect the wavelength of the blackbody and may give inaccurate results if they are not considered. The proposed theory could explain why it is not easy to observe some massive objects in the space even if they emit radiations, such as black holes and dark matters. For validation purposes, the proposed theory is compared to the one suggested by Max Planck in 1901. Results show that both methods give almost the same results for objects with low gravitational fields in space running at low velocity. However, the predicted electromagnetic wavelength using both theories become different for objects with high gravitational fields and travelling at high speed in space. Planck postulated that "***The radiation has a specific spectrum and intensity that depends only on the temperature of the body***". However, as it has been demonstrated in this paper, other factors affect also the intensity of the spectrum including the movement of both objects with respect to each other and their gravitational fields. Hence, the modified postulate the is proposed in this paper will be as follows: "***The radiation has a specific spectrum and intensity that depends on the temperature of the blackbody, density, velocity and movement direction of both the blackbody and the receiver***".

REFERENCES

[1] R. M. Goody, Y. L. Yung,"*Atmospheric Radiation: Theoretical Basis*", (2nd ed.),Oxford University Press, ISBN 978-0-19-510291-8, (1989).

[2] A. Hermann,"*The Genesis of Quantum Theory, Nash, C.W. (transl.)*". MIT Press, ISBN 0-262-08047-8. a translation of Frühgeschichte der Quantentheorie*(1899–1913)*, Physik Verlag, Mosbach/Baden, (1971).

[3] R. A. Serway. J. W. Jewett Jr., "*Physics for Scientists and Engineers*", Published by Brooks/Cole, ISBN-13: 978-0-495-82781-8, (2010).

[4] J. Bunningham, V. Vedral, "*Introductory Quantum Physics and Relativity*", Published by Imperial College Press, ISBN-13: 978-1-84816-514-4, (2011).

[5] B. Berche, "*Relativite*", Laboratoire de physique des materiaux, universite Henri Poincarre, Nancy1.

[6] J. D. Jackson, "*Classical electrodynamics*", Wiley, New York, (third edition), (1999).

[7] I. R. Kenyon, "*General relativity*", Oxford University Press, New York, (1990).

[8] M. V. Berry, "*Principle of cosmology and gravitation*". Institute of Physics publishing, Bristol, (1989).

[9] P. M. Schwarz, J. H. Schwarz, "*Special relativity, from Einstein to strings*", Cambridge University Press, Cambridge, (2004).

[10] M. Longair, "*Theoretical concept in physics*", Cambridge University Press, Cambridge, (2003).

[11] W. Pauli, "*Theory of relativity*", Dover, New York, (1958).

[12] F. Rohrlich, "*Classical charged particles*", Addison-Wesley, Redwood, (1965).

[13] P. G. Bergmann, "*Introduction to the Theory of relativity*", Dover, New York, (1976).

[14] T. Adam, N. Agafonova, A. Zghiche, "*Measurement of the neutrino velocity with the OPERA detector in the CNGS beam*", Journal of High Energy Physics 2012.10 (2012): 1-37.

[15] M. Rezaei, "*Imaginary Relativity*", WSEAS Transactions on Communications, Volume 9, Issue 2,(February 2010), pp. 127-142.

[16] M. Neagu, "*A relativistic approach on 1-jet spaces of the rheonomic Berwald-Moor metric*", Balkan Society of Geometers, Geometry Balkan Press, (2011).

[17] C. Zhang, J. Yue, "*Application of an improved adaptive chaos prediction model in aero-engine performance parameters*", WSEAS Transactions on Mathematics, Volume 11, Issue 2,(February 2012), pp. 114-124.

[18] F. Rozman, "*The EM properties of light*", url: http://www.anti-energija.com/The_properties_of_light.pdf

[19] S. Asif, "*Sputnik and the Soviet Space Challenge*", Gainesville, Florida, The University of Florida Press, (2003), p. 155.

[20] Linda J. Vandergriff,V. McLean"*Nature and Properties of Light*", Fundamentals of Photonics (2008): 1-38.

[21] C. V. Raman, S. Bhagavantam, "*Experimental proof of the spin of the photon*", Indian 3. Phys. 6 353-366,(1931).

[22] F. Kenneth, "*Basic Physics*", Walton, Massachusetts: Blaisdell Publishing Co., (1968).

[23] Jenkins, White. "*Fundamentals of Optics*", New York: McGraw-Hill, (1976).

[24] "*National Photonics Skills Standard for Technicians*", Pittsfield, Massachusetts: Laurin Publishing Company, Inc., (1995).

[25] S. Khalil, "*Electro-Optical Systems Analysis*", Los Angeles: Electro-Optical Research Company, (1985).

[26] C. Starr, C. Evers, L. Starr. "*Biology: concepts and applications*". Cengage Learning, (2014).

[27] D. H. Sliney. "*What is light? The visible spectrum and beyond*", Eye Volume 30, no. 2, (2016). pp. 222-229.

[28] C. Z. Bayeh, "*Introduction to the Absolute Zero Velocity Machine*", International Journal of Mathematics and Computers in Simulation, Vol. 6 (3), March 2012, pp.307-314.

[29] C. Z. Bayeh, "*General Theory of electronic configuration of atoms*", IOSR Journal of Applied Chemistry, Vol. 6, No. 5, January 2014, pp. 14-40.

[30] C. Z. Bayeh, N. E. Mastorakis, "*Unification of the Duality of the Light in One Form*", in the book "Recent Advances in Systems Science and Mathematical Modeling", Proceedings of the 3rd International Conference on Mathematical Models for Engineering Science (MMES '12), Paris, France, WSEAS Press, December 2-4, 2012, pp. 56-64.

[31] C. Z. Bayeh, N. E. Mastorakis, "*Introduction to Astro-Atomic Unitless*", in the book "Recent Advances in Systems Science and Mathematical Modeling", Proceedings of the 3rd International Conference on Mathematical Models for Engineering Science (MMES '12), Paris, France, WSEAS Press, December 2-4, 2012, pp. 45-50.

[32] C. Z. Bayeh, N. E. Mastorakis, "*Measuring the speed of a spaceship using the "Absolute zero velocity machine"*", in the book "Advances in Mathematical and Computational Methods", Proceedings of the 14th WSEAS International Conference on Mathematical and Computational Methods in Science and Engineering (MACMESE '12), Sliema, Malta, WSEAS Press, September 7-9, 2012, pp. 72-78.

[33] C. Z. Bayeh, N. E. Mastorakis, "*Transformation between a fixed frame and a running frame at constant velocity which contains the "Absolute zero velocity machine"*", in the book "Advances in Mathematical and Computational Methods", Proceedings of the 14th

WSEAS International Conference on Mathematical and Computational Methods in Science and Engineering (MACMESE '12), Sliema, Malta, WSEAS Press, September 7-9, 2012, pp. 44-52.

[34] C. Z. Bayeh, N. E. Mastorakis, “*Absolute Zero Velocity Machine*”, in the book “Mathematical Models and Methods in Modern Science”, Proceedings of the 14th WSEAS International Conference on Mathematical Methods, Computational Techniques and Intelligent Systems (MAMECTIS '12), Porto, Portugal, WSEAS Press, July 1-3, 2012, pp. 302-306.

[35] C. Z. Bayeh, “*General Law of Universal Gravitation*”, International Journal of Modern Physics and Application. Vol. 1, No. 5, December 2014, pp. 49-62.

Research Article *Energy, Environment and Storage* (2022) 02-02:24-30

Energy, Environment and Storage

JournalHomepage: www.enenstrg.com

Investigation of the Theoretically Potential for Biogas Production from Mucilage in the Marmara Sea

Saliha Özarslan[1*], M. Raşit Atelge[2], Sebahattin Ünalan[3], S. Orhan Akansu[4]

[1]Department of Mechanical Engineering, Faculty of Engineering, Erciyes University, Kayseri, Türkiye, ORCID:0000-0001-5696-9644

[2]Department of Mechanical Engineering, Faculty of Engineering, Siirt University, Siirt, Türkiye, ORCID:0000-0002-0613-2501

[3]Department of Mechanical Engineering, Faculty of Engineering, Erciyes University, Kayseri, Türkiye, ORCID:0000-0002-5605-2614

[4]Department of Mechanical Engineering, Faculty of Engineering, Erciyes University, Kayseri, Türkiye, ORCID:0000-0002-0085-7915

ABSTRACT

This research is about the disposal and evaluation of mucilage, which threatens human health, marine ecosystem, social life and economy. For this purpose, the idea of providing benefits by creating an alternative to meet the energy need, which is one of the world's priority problems, has been adopted. It has been determined that mucilage can be used in the production of biogas, which is a popular energy type in recent times, in line with its structural properties and content. Biogas, which has the potential to be an alternative to fossil fuels thanks to its numerous advantages, is a versatile renewable energy source that can be used in many different areas. In this study, the biogas production potential of mucilage was investigated theoretically with two different methods. One of the methods is to calculate the methane yield based on the protein, lipid and carbohydrate content of the organic matter. In the other method, according to the results of elemental analysis, the methane yield was calculated using the stoichiometric equation. According to the analysis and calculations, the theoretical methane yield of the mucilage was found to be 528.68 mL CH_4/g VS according to the organic matter content and 526.15 mL CH_4/g VS according to the elemental content. Theoretical calculation of the methane yield before the experimental study saves material and time. In this direction, it has been concluded that the biogas production potential of the mucilage is high and suitable for experimental work, since the methane yield values calculated using different methods are high and close to each other. It is believed that this study, which investigates the disposal of mucilage, which is a harmful formation, and its usability in the production of biogas, which is an efficient energy type, makes a multi-faceted contribution to the literature for humanity.

Keywords: Biogas, Bio-fuel, Methane, Mucilage

Article History: Received: 27.01.2022; Revised: 11.03.2022; Accepted: 19.04.2022; Available online: 20.04.2022
Doi: https://doi.org/10.52924/DDSB1885

1. INTRODUCTION

In our age, energy demand is mostly met by conventional fuels derived from petroleum and electricity produced from fossil fuels. Industrialization and urbanization lead to an increase in the use of fossil fuel resources and thus an increase in toxic and harmful substances released into the environment. Although it takes millions of years for fossil resources to originate, existing supplies are exhausted considerably faster than new fossil fuels are created. The world is in danger of running out of non-renewable energy resources. The rapid decrease in fossil fuel reserves also causes these fuels to become more expensive. In addition, the widespread use of non-renewable fossil energy sources causes an increase in environmental problems that are unacceptable for humanity in the long term, such as global warming, greenhouse gas emissions and climate change. For example, when the carbon footprint is evaluated as a result of the activities of a Waste Recycling Facility located in the province of Kayseri in Turkey; the share of carbon footprint was found to be 76.8% in transportation activities originating from waste collection, 23.1% in natural gas from consumption for heating purposes, and less than 0.1% in electricity use. The total CO_2 emission of the facility was found as 132711 tons. For suchreasons, the search for clean, cheap, renewable and sustainable energy has attracted great interest in recent years. Solar energy, wind energy, biomass energy, tidal energy, and geothermal energy are examples of renewable energy that can be recycled in nature. Natural resources for renewable

*Corresponding author: salihaozarslan@windowslive.com

energy are plentiful, inexhaustible, and good to the environment. One of the renewable energy types is biogas energy. Biogas has been a considerably more popular research issue in the last ten years as worldwide energy demand and environmental consciousness have increased[1-5].

Biogas is a versatile, renewable energy source that may be used to generate heat and power instead of traditional fossil fuels.This type of energy, which can also be used in electricity generation, also has the potential to be used as a gas fuel in the automotive industry.Biogas is obtained by the degradation of the biomass source with microorganisms under anaerobic conditions[6,7]. It mostly contains two main components, methane (CH4) and carbondioxide (CO2). However, other trace species are also present, such as hydrogen sulfide (H2S), hydrogen (H2), nitrogen (N2), ammonia (NH3), oxygen (O2) and carbon monoxide (CO). Water, dust particles, siloxanes, aromatic and halogenated chemicals are also found in ordinary biogas, although the concentrations of these trace components are quite small compared to methane and carbon dioxide power[8].The anaerobic digestion (AD) process consists of several successive biochemical steps. All of these biochemical steps are carried out by microorganisms in the environment. During the AD process, the waste of some microorganisms becomes a food source for other microorganisms. These biochemical steps consist of hydrolysis, acidification and methanogenic phases, respectively[9]. The methanogenic phase is the phase in which the production of CH4 gas occurs prominently. This phase is the last step of the reactions and stands out as the rate determining phase in some waste types. While the methanogenic phase is the rate-determining step when the raw materials are easily degradable, the hydrolysis phase is the rate-determining step in raw materials with a complex structure [10].

General components of organic substances; can be listed as carbohydrates, protein, lipid and lignin. Hydrolysis is generally characterized as the breakdown of nutrients in water into small building blocks. Carbohydrates are hydrolyzed in a few hours, proteins and lipids in a few days, and lignin and lignocellulose in longer time [11]. Another disadvantage of raw materials with lignin and lignocellulose components is that the degradation process cannot be performed completely. The presence of non-biodegradable raw materials causes low CH4 yields and long processing times. Therefore, it is required to deconstruct the complex structures and slowly biodegradable components in the waste into small building blocks in order to improve the CH4 production. Examples of these slowly degrading components are lignocellulosic biomass. Some processing steps have been proposed to achieve high degradation of such biomass [12]. These steps are called preprocessing.

With the pretreatment stages, the waste components become easily biodegradable, thus reducing the most important disadvantage in AD processes [13]. In the literature, pretreatments are grouped into three groups: physical, chemical and biological. In addition, to reduce the effect and expense of biogas production, these pretreatments are administered concurrently or sequentially with two or more pretreatments, referred to as combined pretreatments. In this case,oil extraction has been defined as a combined pretreatment in the literature and has been successfully applied to biomass (microalgae) grown in water [11].In the literature, there are comprehensive studies on biogas and methane production from a wide variety of organic wastes such as tea factory waste, brewed tea waste, orange pulp, grass, pond sludge mixed with apple, vegetable waste, fruit pulp waste, algae, cow dung, cow urine, wheat straw, water hyacinth and banana peels[14-22].

Mucilage can be defined as a slimy, sticky structure formed by the overgrowth of plant organisms called phytoplankton, the rise in sea temperature and the resulting increase in bacterial activities. In the literature review on mucilage, studies in different fields were identified. For example, with the use of remote sensing techniques, a system for detecting mucilage production in the Sea of Marmara has been devised. It has been demonstrated that mucilage production may be detected rapidly and accurately from satellite photos anywhere across the world using this new technology [23].In a study on the formation and structure of mucilage, it was determined that foam accumulation occurs in the North Sea's coastal waters every spring, on the sea surface and on the beaches under windy conditions. For this reason, a single phytoplanktonic species called Phaeocystis multiplied, causing the food chain to deteriorate and mucilage was observed [24]. Öztürk et al., on the other hand, examined the dispersion of mucilage in the Marmara Sea’s water and determined that it reached the lower layer waters[25].

Giuliani et al. researched the effects of mucilage on other organisms in their study on mucilage formed in theTyrrhenian Sea in the Mediterranean[26]. Another study was carried out in the Mediterranean. Viruses in seawater containing mucilage were investigated to examine the mucilage's potential to host new microbial diversity and/or spread marine diseases. The development of mucilage in the Mediterranean has been connected to climate-related sea surface warming, according to the findings[27]. In some of the studies, the importance of bacteria in the mucilage phenomenon in the North Adriatic Sea, temporal dynamics of dissolved and particulate organic carbon, phytoplankton community structure, hypotheses and the relationships between mucilage events and climate variability were investigated [28-32]. Phytoplankton composition, environmental conditions and harmful algae growth production of mucilage in the Marmara Sea are also among the investigations [33,34]. In a study conducted on the shores of Büyükada in the Marmara Sea, the role of unicellular organisms in mucilage formation was investigated [35].

In addition, temporal changes in phytoplankton composition in the Northeast Marmara Sea, as well as changes in zooplankton population abundance and community structure, were explored [29,30]. In another study, temporal changes in picoplanktonic Synechococcus (Cyanobacteria) abundance during a mucilage formation in Bandırma and Erdek Bays were investigated [31]. Additionally, the effects of the mucilage event on a fish species in the shallow waters of the Dardanelles and North Aegean Sea are among the researched subjects [32]. Another study was conducted on Cryptobenthic fish communities affected by the mucilage formation in the northeastern Aegean Sea [33].Aslan et al. reported that in their study investigating the effect of mucilage on peraccharide communities, which have an important place in the marine ecosystem, negative results were revealed [34].In the study of Caronni et al., the ecology of microalgae species that cause mucilage formation in the Western Mediterranean was investigated[35].Furthermore, a study was conducted to research the effects of mucilage on ship operations in maritime and it was aimed to minimize the effects of mucilage [36].In their study, Uflaz et al. investigated the large-scale mucilage event that consisted in the North Aegean Sea and the Dardanelles Strait in 2021 and investigated the effect of some benthic species on mass mortality[37]. As can be seen, studies on mucilage structure have focused on the causes of formation, its structure, and its effects on other living things and nature. No study has been found in the literature regarding the disposal of mucilage or its conversion into high value-added products.

As mentioned in the previous lines, biogas is considered as a clean energy type obtained from organic wastes by anaerobic digestion and can be an alternative to fossil fuels.Biogas is suitable for utilize in many different areas such as electricity production, domestic heating, automotive industry, purification and chemical industry.Carbon (C), hydrogen (H), oxygen (O), nitrogen (N) and sulphur (S) are important elements for biogas production[45,46].In addition, according to the information obtained from the literature, methane yields of biomass (microalgae) grown in water were found at a good level[47-50].Based on these, this study aimed to obtain and dispose of a beneficial product from the environmentally harmful mucilage structure formed in the Marmara Sea in Türkiye. In this study, which aims to provide multi-faceted benefits, the potential of biogas production from the mucilage structure formed by the combination of many biological and chemical conditions in the seas was investigated. The theoretical potential of the mucilage structure for biogas production, which is such a useful energy type, has been investigated. It is thought that converting mucilage into biogas, which is a clean energy type, will make important contributions both in the field of energy production and in the disposal of mucilage, which is harmful to the environment.

With the help of an elemental analyser (Leco/TruSpec Micro model, USA), the C, H, O, N, and S contents of each substrate were determined. Theoretical biological methane potential (mL CH_4/g VS) was then estimated from elemental analysis findings ($C_nH_aO_bN_c$) offeedstocks using the stoichiometric equation (Eq. (2)) (BMP_{thAtC})[51].

Elemental analysis is the process of measuring certain elements in a sample. Elemental analysers work with a combustion reaction-based logic. With combustion at high temperatures (950-1300^{o}C), organic matter containing C, H, N and S decomposes in pure oxygen environment and turns into gaseous compounds. As a result of combustion, carbon turns into CO_2 gas; hydrogen to H_2O; nitrogen turns into N_2 gas and finally sulfur into SO_2 gas and the device reports the C, H, N, S amounts in the sample as percentages over these gases. The percentage of O other than these was calculated by subtracting the C, H, N, S percentages and the percentages of trace metals from the percentage. Experiments were carried out at Recep Tayyip Erdoğan University Central Research Laboratory Application and Research Center (Merlab) in Türkiye, using a TruSpec Micro brand device. The experiments were repeated three times, and the averages of the results were taken.

2. MATERIALS AND METHODS

2.1 Determination of Protein, Lipid and Carbohydrate Percentages

The amounts of organic waste components such as protein, lipid and carbohydrates affect the biogas and methane yield. Theoretically, 1014, 740 and 370 mL CH_4/g VS methane can be produced from lipids, proteins and carbohydrates in the AD process, respectively [52].In order to determine the theoretical biogas and methane yield of wastes, carbohydrate, protein and lipid ratios should be measured. Protein determination was determined by Kjeldahl protein method, lipid percentages were determined by Soxhlet method and ash determination was determined according to the method applied in VS calculation. Carbohydrates were obtained by adding other percentages and subtracting from 100.

2.2 Determination of Theoretical Methane Yield

It is possible to compute the theoretical methane yield by two different methods. In the first method, methane yield is calculated using protein, carbohydrate and lipid percentages and is shown in Equation (1) (BMP_{thOFC}).In the second method, the methane yield is calculated from the stoichiometric equation (Equation (2)) (BMP_{thAtC}). The n, a, b, c values in the stoichiometric equation were calculated according to the elemental analysis results of the samples ($C_nH_aO_bN_c$)[51].

$$\boldsymbol{BMP_{thOFC} = 415 \times Carbohydrate\% + 496 \times Protein\% + 1014 \times Lipid\%} \quad (1)$$

$$\boldsymbol{BMP_{thAtC} = 22.4\,\frac{\frac{n}{2}+\frac{a}{8}-\frac{b}{4}-\frac{3c}{8}}{12n+a+16b+14c}} \quad (2)$$

3. RESULT AND DISCUSSION

3.1 Determination of Protein, Lipid and Carbohydrate Percentages and Theoretical Methane Yield

Table 2 shows the organic fraction composition analysis of mucilage and the theoretical methane yield computed with Equation 1 based on this. The protein, lipid, ash and carbohydrate percentages of the mucilage were measured as 2.7, 28, 18 and 51.3%, respectively. Accordingly, the methane yield was calculated as 528.68mL CH_4/g VS. This result is significant.

Nielfa et al.[53]investigated the experimental and theoretical methane yield of samples obtained by mixing organic fraction municipal solid waste and biological sludge at different ratios. Theoretical methane yield of Co-digestion 1 sample prepared at the ratio of 80/20 (organic fraction municipal solid/biological sludge % weight) was calculated as 506.3 ml CH_4/g VS, according to the organic fraction composition. The experimental methane yield of the same sample was found as 220.6 ± 6 ml CH_4/g VS. In another study, Maya-Altamira et al.[54] investigated the methane potential of food processing industry wastewater. The theoretical methane yield of the wastewater used in the production of peas was 0.49 STPl-CH_4/gCOD and the experimental methane yield was 0.36 ± 0.05 STPl-CH_4/gCOD, according to the organic fraction.

Table 2 Protein, Lipid and Carbohydrate Content and Theoretical Methane Yield of Mucilage

	Protein (%)	Lipid(%)	Ash (%)	Carbohydrate (%)	BMP_{thOFC}(mLCH_4/gVS)
Mucilage	2.7	28	18	51.3	528.68

3.2 Determination of Theoretical Methane Yield by Elemental Analysis

The elemental analysis consequencesbelong to the mucilage are shown in Table 3. In the structure of mucilage, the C ratio is 51.40%, the H ratio is 7%, the O ratio is 40.08%, the N ratio is 1.44% and the S ratio is 0.08%. Considering these data, the methane yield was calculated as 526.15mL CH_4/g VS by means of Equation 2.It is believed that the fact that the theoretical methane yields calculated by the organic fraction composition analysis and calculated with the stoichiometric equation according to the elemental analysis results are so close to each other increases the accuracy.

Table 3 Theoretical Methane Yield of Mucilage based on Elemental Analysis

				$C_nH_aO_bN_c$		$C_nH_aO_bN_cS_d$		BMP_{thAtC} (mL CH_4/g VS)	
				calculation	**integer number**	**calculation**	**integer number**	$C_nH_aO_bN_c$	$C_nH_aO_bN_cS_d$
Mucilage	**C (%)**	51.40	n	4.28	42	4.28	1715		
	H (%)	7.00	a	6.95	68	6.95	2784		
	O (%)	40.08	b	2.51	24	2.51	1004	526.15	525.59
	N (%)	1.44	c	0.10	1	0.10	41		
	S (%)	0.08	d	0	0	0	1		

Aragón-Briceño et al.[55] carried out a study to determine the effects of process conditions on the properties of hydrocoals and process waters during hydrothermal treatment of a wastewater digester, and the effects of the fate of nutrients such as nitrogen and phosphorus on methane yield.Boyle and Buswell equations were used to determine the theoretical methane yields of the hydrothermal products they used in their studies. When they compared the theoretical methane yields with the experimental data, they found that Boyle's equation was closer to the BMP values.For example, the methane yield obtained in one of the experimental studies was 260.0 (mL of CH_4/g of COD added), while the calculated theoretical value was 271.6 (mL of CH_4/g COD).Nielfa et al.[53], on the other hand, tried different methods, including elemental and organic fraction composition analyses, to calculate the theoretical methane production efficiency produced by digesting municipal solid waste and biological sludge together, and compared them with the experimental conclusions. For one of the models they created, the error percentage was 5 for the elemental composition and -3 for the organic fraction composition.

Table 4 Comparison of theoretical methane yields of studies in the literature

Sample	BMP_{thAtC} (mL CH_4/g VS)	BMP_{thOFC} (mL CH_4/gVS)	Reference
Wastewater (Vegetable production: leek and fried onion)	340 (at STP conditions)	300	[54]
Wastewater (Vegetable fats and oils)	350	140	[54]
Biological sludge	333.9	338.2	[53]
Chlorella sp. algae	550	-	[56]
Nannochloropsis sp. algae	630	-	[56]
Mucilage	526.15	528.68	This study

Maya-Altamira et al.[54], in their study to evaluate the methane potential of food industry wastewater, suggested that estimating the theoretical methane yield based on atomic fractions is more precise than estimating based on organic composition. The reason for this, they claimed, was that the VS analytical results were less representative than the COD values. Bohutskyi et al.[56] conducted a study on methane production from different algae strains. For example, in the experimental study in which T. weissflogii algae was used as the substrate, the methane yield was determined to be 0.38 ± 0.01 L CH_4 (g VS)$^{-1}$. The theoretically calculated yield is very close to this value (0.48 L CH_4 (g VS)$^{-1}$).In another study by Bird et al.[57] using marine algae, the theoretical methane yield was given together with the experimental yield. For example, the difference between the theoretical and actual biochemical methane potential obtained from one of the Gracilaria spp. samples was determined as only 0.02 (m^3 kg^{-1} V.S. added).

As can be seen from the examples, the theoretically calculated methane yield can be quite close to the actual yield. Calculating the methane yield with different methods using different data allows the prediction of possible scenarios and the verification of the result.In addition, the theoretical calculations made before the experimental studies save time and material. In this study, the methane yield of the mucilage material was calculated theoretically by two different methods. The fact that the results are very close to each other increases the probability of the experimental study to be successful. The high results also give a hint that experiments to produce methane from the mucilage structure will be successful as well as worth trying.

4. CONCLUSION

In this study, theoretical methane yield of mucilage was investigated by using two different methods.In the first of these methods, the methane yield was calculated according to the protein, lipid and carbohydrate content of the mucilage. The protein percentage of the mucilage was 2.7, the lipid percentage was 28 and the carbohydrate percentage was 51.3.The methane yield calculated accordingly is 528.68 mL CH_4/g VS. The second method used to calculate the theoretical methane yield is the method using elemental analysis results. According to the results of the elemental analysis of the mucilage, the percentages of C, H, O, and N are 51.4, 7, 40.08 and 1.44, respectively. The methane yield calculated from these results is 526.15 mL CH_4/g VS. When the theoretical methane yield calculated by the organic fraction composition analysis and the theoretical methane yield calculated with the stoichiometric equation according to the elemental analysis results are examined, it is seen that the use of mucilage for biogas production is quite promising in terms of energy production.

REFERENCES

[1] A. Pareek, R. Dom, J. Gupta, J. Chandran, V. Adepu, & P.H. Borse, Insights into renewable hydrogen energy: Recent advances and prospects,*Materials Science for Energy Technologies*, Vol. 3: pp. 319-327, 2020.

[2] H. Wang, Z. Lei, X. Zhang, B. Zhou, & J. Peng, A review of deep learning for renewable energy forecasting,*Energy Conversion and Management*, Vol. 198: pp. 111799, 2019.

[3] M. Atelge, D. Krisa, G. Kumar, C. Eskicioglu, D.D. Nguyen, S.W. Chang, A. Atabani, A.H. Al-Muhtaseb, & S. Unalan, Biogas production from organic waste: Recent progress and perspectives,*Waste and Biomass Valorization*, Vol. 11(3): pp. 1019-1040, 2020.

[4] J. Olaleru, J. Kirui, F. Elegbeleye, & T. Aniyikaiye, Green technology: Solution to global climate change mitigation,*Energy, Environment, and Storage Journal*, Vol. 1(1): pp. 26-41, 2021.

[5] N.F. Demirbas, Evaluation of carbon footprint in a waste recovery/recycle facility,*Energy, Environment, and Storage Journal*, Vol. 1(1): pp. 7-12, 2021.

[6] N. Scarlat, J.-F. Dallemand, & F. Fahl, Biogas: Developments and perspectives in europe,*Renewable energy*, Vol. 129: pp. 457-472, 2018.

[7] M. Atelge, A. Atabani, S. Abut, M. Kaya, C. Eskicioglu, G. Semaan, C. Lee, Y. Yildiz, S. Unalan, & R. Mohanasundaram, Anaerobic co-digestion of oil-extracted spent coffee grounds with various wastes: Experimental and kinetic modeling studies,*Bioresource Technology*, Vol. 322: pp. 124470, 2021.

[8] I.U. Khan, M.H.D. Othman, H. Hashim, T. Matsuura, A. Ismail, M. Rezaei-DashtArzhandi, & I.W. Azelee, Biogas as a renewable energy fuel–a review of biogas upgrading, utilisation and storage,*Energy Conversion and Management*, Vol. 150: pp. 277-294, 2017.

[9] R. Goswami, P. Chattopadhyay, A. Shome, S.N. Banerjee, A.K. Chakraborty, A.K. Mathew, & S. Chaudhury, An overview of physico-chemical mechanisms of biogas production by microbial communities: A step towards sustainable waste management,*3 Biotech*, Vol. 6(1): pp. 72, 2016.
[10] F. Passos, V. Ortega, & A. Donoso-Bravo, Thermochemical pretreatment and anaerobic digestion of dairy cow manure: Experimental and economic evaluation,*Bioresource technology*, Vol. 227: pp. 239-246, 2017.
[11] M. Atelge, A. Atabani, J.R. Banu, D. Krisa, M. Kaya, C. Eskicioglu, G. Kumar, C. Lee, Y. Yildiz, & S. Unalan, A critical review of pretreatment technologies to enhance anaerobic digestion and energy recovery,*Fuel*, Vol. 270: pp. 117494, 2020.
[12] R. Karki, W. Chuenchart, K. Surendra, S. Shrestha, L. Raskin, S. Sung, A. Hashimoto, & S.K. Khanal, Anaerobic co-digestion: Current status and perspectives,*Bioresource Technology*, Vol.: pp. 125001, 2021.
[13] H. Şenol, Anaerobic digestion of hazelnut (corylus colurna) husks after alkaline pretreatment and determination of new important points in logistic model curves,*Bioresource technology*, Vol. 300: pp. 122660, 2020.
[14] A. Lahbab, M. Djaafri, S. Kalloum, A. Benatiallah, M. Atelge, & A. Atabani, Co-digestion of vegetable peel with cow dung without external inoculum for biogas production: Experimental and a new modelling test in a batch mode,*Fuel*, Vol. 306: pp. 121627, 2021.
[15] S. Özarslan, S. Abut, M. Atelge, M. Kaya, & S. Unalan, Modeling and simulation of co-digestion performance with artificial neural network for prediction of methane production from tea factory waste with co-substrate of spent tea waste,*Fuel*, Vol. 306: pp. 121715, 2021.
[16] R. Atelge, Co-digestion of orange pulp and cattle manure with different c/n ratios and a new modeling of biogas production,*Karadeniz Fen Bilimleri Dergisi*, Vol. 11(2): pp. 557-569,
[17] C. Rodriguez, A. Alaswad, K. Benyounis, & A.G. Olabi, Pretreatment techniques used in biogas production from grass,*Renewable and sustainable energy reviews*, Vol. 68: pp. 1193-1204, 2017.
[18] S. Sandhu and R. Kaushal, Anaerobic co-digestion of food wastes, algae, pond sludge and cow dung for biogas yield enhancement as a potent approach to reduce carbon footprints,*Australian Journal of Mechanical Engineering*, Vol.: pp. 1-20, 2022.
[19] R. Baitha and R. Kaushal, Experimental and numerical study of biogas, methane and carbon dioxide produced by pre-treated wheat straw and pre-digested cow dung,*International Journal of Sustainable Engineering*, Vol. 12(4): pp. 240-247, 2019.
[20] R. Kaushal and R. Baitha, Biogas and methane yield enhancement using graphene oxide nanoparticles and ca (oh) 2 pre-treatment in anaerobic digestion,*International Journal of Ambient Energy*, Vol. 42(6): pp. 618-625, 2021.
[21] R. Baitha and R. Kaushal, Numerical and experimental study of biogas, methane and carbon dioxide produced by pre-treated slurry,*International Journal of Ambient Energy*, Vol. 41(2): pp. 198-204, 2020.
[22] V.B. Barua, V. Rathore, & A.S. Kalamdhad, Anaerobic co-digestion of water hyacinth and banana peels with and without thermal pretreatment,*Renewable Energy*, Vol. 134: pp. 103-112, 2019.
[23] A. Uğur, O.S. Yılmaz, M. Çelen, A.M. Ateş, F. Gülgen, & F.B. Şanlı, Determination of mucilage in the sea of marmara using remote sensing techniques with google earth engine,*International Journal of Environment and Geoinformatics*, Vol. 8(4): pp. 423-434, 2021.
[24] C. Lancelot, The mucilage phenomenon in the continental coastal waters of the north sea,*Science of the total environment*, Vol. 165(1-3): pp. 83-102, 1995.
[25] İ.D. Öztürk, S. Mutlu, G. Kaman, F.B. Partal, A. Demirtaş, S. Çağlar, E. Kuzyaka, H. Altıok, & D. Ediger, Vertical distribution of mucilage typology in the water column after a massive mucilage formation in the surface waters of the sea of marmara,*Journal of the Black Sea/Mediterranean Environment*, Vol. 27(2), 2021.
[26] S. Giuliani, C.V. Lamberti, C. Sonni, & D. Pellegrini, Mucilage impact on gorgonians in the tyrrhenian sea,*Science of the Total Environment*, Vol. 353(1-3): pp. 340-349, 2005.
[27] R. Danovaro, S. Fonda Umani, & A. Pusceddu, Climate change and the potential spreading of marine mucilage and microbial pathogens in the mediterranean sea,*PLoS One*, Vol. 4(9): pp. e7006, 2009.
[28] F. Azam and E. Funari, Significance of bacteria in the mucilage phenomenon in the northern adriatic sea,*Annali dell'Istituto superiore di sanità*, Vol. 35(3): pp. 411-419, 1999.
[29] M. Giani, F. Savelli, D. Berto, V. Zangrando, B. Ćosović, & V. Vojvodić, Temporal dynamics of dissolved and particulate organic carbon in the northern adriatic sea in relation to the mucilage events,*Science of the Total Environment*, Vol. 353(1-3): pp. 126-138, 2005.
[30] C. Totti, M. Cangini, C. Ferrari, R. Kraus, M. Pompei, A. Pugnetti, T. Romagnoli, S. Vanucci, & G. Socal, Phytoplankton size-distribution and community structure in relation to mucilage occurrence in the northern adriatic sea,*Science of the Total Environment*, Vol. 353(1-3): pp. 204-217, 2005.
[31] D. Degobbis, A. Malej, & S.F. Umani, The mucilage phenomenon in the northern adriatic sea. A critical review of the present scientific hypotheses,*Annali dell'Istituto superiore di sanità*, Vol. 35(3): pp. 373-381, 1999.
[32] M. Deserti, C. Cacciamani, J. Chiggiato, A. Rinaldi, & C.R. Ferrari, Relationships between northern adriatic sea mucilage events and climate variability,*Science of the total environment*, Vol. 353(1-3): pp. 82-88, 2005.

[33] V. Tüfekçi, N. Balkis, C.P. Beken, D. Ediger, & M. Mantikci, Phytoplankton composition and environmental conditions of the mucilage event in the sea of marmara,*Turkish Journal of Biology*, Vol. 34(2): pp. 199-210, 2010.
[34] S. Taş, H.A. Ergül, & N. Balkis, Harmful algal blooms (habs) and mucilage formations in the sea of marmara,*The Sea of*, Vol. 768, 2016.
[35] N. Balkis, H. Atabay, I. Türetgen, S. Albayrak, H. Balkis, & V. Tüfekçi, Role of single-celled organisms in mucilage formation on the shores of büyükada island (the marmara sea),*Journal of the Marine Biological Association of the United Kingdom*, Vol. 91(4): pp. 771-781, 2011.
[36] S. Tas, D. Kus, & I.N. Yilmaz, Temporal variations in phytoplankton composition in the northeastern sea of marmara: Potentially toxic species and mucilage event,*Mediterranean Marine Science*, Vol. 21(3): pp. 668-683, 2020.
[37] M.İ. Okyar, F. Üstün, & D.A. Orun, Changes in abundance and community structure of the zooplankton population during the 2008 mucilage event in the northeastern marmara sea,*Turkish Journal of Zoology*, Vol. 39(1): pp. 28-38, 2015.
[38] B. Toklu-Alicli, S. Polat, & N. Balkis-Ozdelice, Temporal variations in the abundance of picoplanktonic synechococcus (cyanobacteria) during a mucilage event in the gulfs of bandırma and erdek,*Estuarine, Coastal and Shelf Science*, Vol. 233: pp. 106513, 2020.
[39] A. Altin, O. Ozen, & H. Ayyildiz, Temporal variations of the demersal fish community in the shallow waters of çanakkale strait, north aegean sea, during the course of a mucilage event, Vol., 2015.
[40] C. Dalyan, N.B. Kesici, & F. Yalgın, Preliminary study on cryptobenthic fish assemblages affected by the mucilage event in the northeastern aegean sea,*Journal of the Black Sea/Mediterranean Environment*, Vol. 27(2), 2021.
[41] H. Aslan, Z. Tekeli, & Ö. Bacak, Effects of mucilage on the benthic crustacean in the north aegean sea,*Journal of the Black Sea/Mediterranean Environment*, Vol. 27(2), 2021.
[42] S. Caronni, A. Bresciani, M.A. Delaria, F. Meloni, A. Navone, P. Panzalis, K. Heimann, & G. Ceccherelli, Ecology of the benthic mucilage-forming microalga chrysophaeum taylorii in the w mediterranean sea: Substratum and depth preferences,*Estuarine, Coastal and Shelf Science*, Vol. 161: pp. 38-45, 2015.
[43] E. Uflaz, E. Akyüz, F. Bolat, P. Bolat, & Ö. Arslan, Investigation of the effects of mucilage on maritime operation,*Journal of the Black Sea/Mediterranean Environment*, Vol. 27(2), 2021.
[44] H.B. Özalp, A preliminary assessment of the mass mortality of some benthic species due to the mucilage phenomenon of 2021 in the çanakkale strait (dardanelles) and north aegean sea,*Journal of the Black Sea/Mediterranean Environment*, Vol. 27(2), 2021.
[45] S. Achinas and G.J.W. Euverink, Theoretical analysis of biogas potential prediction from agricultural waste,*Resource-Efficient Technologies*, Vol. 2(3): pp. 143-147, 2016.
[46] I.F.S. dos Santos, N.D.B. Vieira, L.G.B. de Nóbrega, R.M. Barros, & G.L. Tiago Filho, Assessment of potential biogas production from multiple organic wastes in brazil: Impact on energy generation, use, and emissions abatement,*Resources, Conservation and Recycling*, Vol. 131: pp. 54-63, 2018.
[47] M. Alzate, R. Muñoz, F. Rogalla, F. Fdz-Polanco, & S. Pérez-Elvira, Biochemical methane potential of microalgae biomass after lipid extraction,*Chemical Engineering Journal*, Vol. 243: pp. 405-410, 2014.
[48] B. Zhao, J. Ma, Q. Zhao, L. Laurens, E. Jarvis, S. Chen, & C. Frear, Efficient anaerobic digestion of whole microalgae and lipid-extracted microalgae residues for methane energy production,*Bioresource technology*, Vol. 161: pp. 423-430, 2014.
[49] J.L. Ramos-Suárez and N. Carreras, Use of microalgae residues for biogas production,*Chemical Engineering Journal*, Vol. 242: pp. 86-95, 2014.
[50] D. Hernández, M. Solana, B. Riaño, M. García-González, & A. Bertucco, Biofuels from microalgae: Lipid extraction and methane production from the residual biomass in a biorefinery approach,*Bioresource technology*, Vol. 170: pp. 370-378, 2014.
[51] M.M. Ali, D. Nourou, B. Bilal, & M. Ndongo, Theoretical models for prediction of methane production from anaerobic digestion: A critical review,*International Journal of Physical Sciences*, Vol. 13(13): pp. 206-216, 2018.
[52] P.W. Harris and B.K. McCabe, Review of pre-treatments used in anaerobic digestion and their potential application in high-fat cattle slaughterhouse wastewater,*Applied Energy*, Vol. 155: pp. 560-575, 2015.
[53] A. Nielfa, R. Cano, & M. Fdz-Polanco, Theoretical methane production generated by the co-digestion of organic fraction municipal solid waste and biological sludge,*Biotechnology Reports*, Vol. 5: pp. 14-21, 2015.
[54] L. Maya-Altamira, A. Baun, I. Angelidaki, & J.E. Schmidt, Influence of wastewater characteristics on methane potential in food-processing industry wastewaters,*Water research*, Vol. 42(8-9): pp. 2195-2203, 2008.
[55] C. Aragón-Briceño, A. Ross, & M. Camargo-Valero, Evaluation and comparison of product yields and bio-methane potential in sewage digestate following hydrothermal treatment,*Applied energy*, Vol. 208: pp. 1357-1369, 2017.
[56] P. Bohutskyi, M.J. Betenbaugh, & E.J. Bouwer, The effects of alternative pretreatment strategies on anaerobic digestion and methane production from different algal strains,*Bioresource technology*, Vol. 155: pp. 366-372, 2014.
[57] K.T. Bird, D.P. Chynoweth, & D.E. Jerger, Effects of marine algal proximate composition on methane yields,*Journal of applied phycology*, Vol. 2(3): pp. 207-213, 1990.

Research Article *Energy, Environment and Storage* (2022) 02-02:31-40

Energy, Environment and Storage

JournalHomepage: www.enenstrg.com

Bulk Switched DC-DC Buck Converter

Seyfettin Gürel[1], Sezai Alper Tekin[2*]

[1]*Energy Market Regulatory Authority (EPDK),Ankara, Turkey* [1]*ORCID:0000-0001-8504-2784*

[*2]*Department of Industrial Design Engineering, Erciyes University, Kayseri, Turkey*[*2]*ORCID:0000-0001-5860-2758*

ABSTRACT. This paper presents a buck converter which has an high efficient and low power consumption for low power applications. The proposed topology is based on buck converter using switching MOSFET with bulk-terminal. The suitable bulk-terminal switching voltage is selected by analyzing the effect of bulk voltage on a MOSFET performance. It is concluded that the bulk-switched DC-DC buck converter structure has the advantages such as high switching performance, low power consumption and high efficiency compared to conventional DC-DC converter circuits. The efficiency value has obtained 88.2%. The proposed circuit is approved experimentally and simultaneously.

Keywords:CMOS Integrated Circuits, Converters, DC-DC power converters, .Solar Power Conversion, Switching Converters

Article History: Received: 22.02.2022; Revised: 11.03.2022; Accepted: 26.04.2022; Available online: 26.04.2022

Doi: https://doi.org/ 10.52924/BCMQ4493

1. INTRODUCTION

In recent years, renewable energy systems have been popular whereas the fossil fuel based conventional system has the negative effect on the environment and human health. In addition, it is also important to transport and store the energy in these systems in the most efficient way. Therefore, scholars have been focused on the design systems used as being more efficient and sustainable. The converter circuits are a very critical importance in terms of efficiency because the voltage and current parameters need to be converted for storing and transporting. The converter circuits can be defined as structures that efficiently convert voltage and current levels of generated electrical energy to significant levels to be used in power systems [1]. Additionally, DC/DC converters using for low power applications constitute the backbone of diverse portable electronic devices such as smartphones, laptops, navigation devices and automotive electronics which are using batteries as their power supply. Portable devices ordinarily consist of several sub-circuits that should be supplied with different voltage levels which is the main supply voltage [2]. There are many workings in the literature about DC-DC Converter applications such that it can be used in various areas such as communication systems, energy har vesting circuits for solar systems and piezoelectricapplications. Piezoelectric harvesting circuits are attractive because it can be said that these circuits make easier energy harvesting from piezoelectric material by matching load impedance with source impedance in circuit. This is also called maximum power point in which the circuit operates with maximum output voltage. Then, the maximum power transfer can be available from harvesting circuit. Optimizing with these parameters, the buck harvester circuit has high output voltage and high switching speed that can be designed for piezoelectric devices [3,4]. Hence, there are many kinds of converters which are suggested for different voltage ranges by researchers [4-9]. An off-grid with lead acid-based battery PV system is designed for the system. The charge status of battery is arranged with MPPT technique. It is specified that there is an improvement in PV performance which is simulated with DSP card design. There may be shading and mismatch conditions due to the interconnection of PV panels. To solve this problem, distributed MPPT system with synchronous buck converter is proposed for increasing efficiency [10, 11]. As indicated in the above, many designs of innovative converters are mainly related to reducing the dimensions of circuit components, area and the total weight of circuit design for mobile systems.

These parameters can be resized when it is available new devices that operate at high switching frequencies. The suggested buck converter design is composed of main circuit and the control unit for control-ling the microprocessor via opto-coupler [12].

The converter topology which exists in literature also takes place in data communication systems. It is possible to reach high power levels and data rates for these systems

*Corresponding author: satekin@erciyes.edu.tr

[13]. The minimization of losses is the most important topic for designing converter circuits. In the literature, there are many designs and techniques offered by a scholar to diminish the switching stress and losses in different converter designs [14-17]. On the other hand, there are many studies about algorithm-based DC-DC Converter designs, but it is not enough studies that focusing switching loses circuit design for buck converters. there are few workings about the circuit and transistor structures in the literature [16].

The present study is aimed to bulk controlled DC-DC buck converter that reduces transistor switching losses using bulk terminal of a MOSFET. The main aim of this study is to design a DC-DC buck converter which has less power consumption than the current state-of-the-art studies available in the literature. Circuit designs which consist of transistors with four terminals are available in literature related with low-power applications and microelectronic circuit designs [26, 27]. However, it is not encountered converter applications in literature. Besides, there are not many studies about the suggested converter which includes low power circuit structures. The clear contribution of this design is to have low power consumption and operate at low-er duty cycle compared with other converter topologies in the literature. In this study, it is intended to design the DC-DC buck converter which is simple and effective without changing the fundamental structure of buck converter. The classic and proposed buck converter designs are examined and performed as a simulation and experimentally. Additionally, the proposed and other converters which are given in literature are compared with respect to performance criteria. Eventually, the proposed design can contribute positively to the converter structures.

2. THE CONVENTIONAL BUCK CONVERTER

A classic buck converter is shown in Fig. 1. During the design process of converter structures, the structure of the topology is very important to validate and analyze the operation of the circuit.

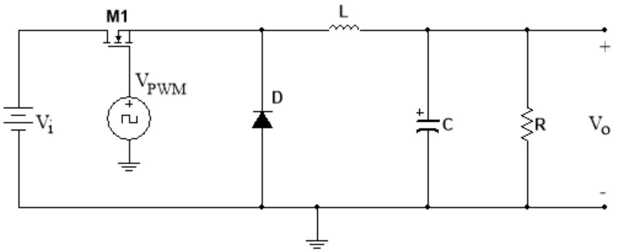

Fig 1. The conventional DC-DC Buck Converter.

The mathematical equations for this converter can be given as Equation (1-3):

$$V_i(t)=V_0(t)+L\cdot\frac{di(t)}{dt} \quad (1)$$

$$i_L(t)=\frac{1}{L}\int (V_i(t)-V_0(t \quad (2)$$

When it is applied KVL and KCL in the Fig. 1, it is obtained as follows:

$$i_c(t)=i_L(t)-i_R(t) \quad (3)$$

2. PROPOSED CIRCUIT DESIGN

2.1 The Switching of MOSFET

There is a duration that is necessary for operating MOSFET in the cut-off region or out of this region. In converter design, the core of the converter is the MOSFET which is the semiconductor device to control the whole system. The on-period duration changes the values between maximum and minimum values of the duty cycle (D). The output voltage varies with this duty cycle. Also, the switching frequency is reversely proportional with voltage ripple in load. For reducing ripples, the frequency should be increased [19]. The frequency of MOSFET is most important parameter for designing desired input and output voltages. When the frequency boosts up, the power consumption also ascends. Besides, the amount of power consumption reaches its highest values in falling and rising times of MOSFET. For this reason, it becomes very important to deal with this effect via using different strategies.

The bulk terminal of MOSFET is usually connected to source terminal. In this manner, it is tried to eliminate the body effect parameter. However, the body effect can be considered as an advantageous for the MOSFET. Therefore, it is also possible to use bulk terminal of MOSFET. The MOSFET's threshold voltage V_{TH} is given by Equation (4) [20].

$$V_{TH}=V_{T0}+\gamma\cdot[\sqrt{|2\varphi_F|-v_{BS}}-\sqrt{|2\varphi_F|}] \quad (4)$$

(a)

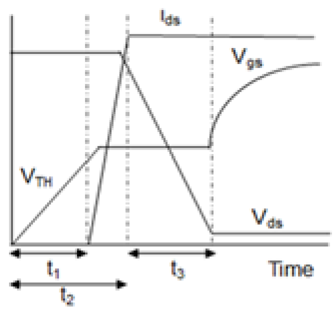

(b)

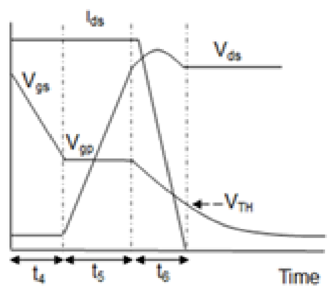

Fig. 2(a). A turn on transient of the MOSFET; **(b).** A turn off transient of the MOSFET

In Equation (4), γ is the factor of body effect, V_{BS} is the voltage of bulk-to-source voltage, V_{T0} is the threshold voltage when V_{BS} =0, φ_F represents the change in the surface potential, respectively [21]. From the equation

(4), it can be said that increasing with V_{BS}, the value of V_{TH} decreases. Hence, a drain current ID increases and a drain resistance R_D decrease during operation of the MOSFET.

The MOSFET has been used as a switching device. To make switching process, it has been used PWM signal. PWM signal is preferable since it has been given an ability to control on the system. The turn-on and turn-off characteristics which are called switching time for the MOSFET is displayed in Fig. 2(a) and (b) [22].
The length of the switching time has a negative effect on the power consumed by the transistor. The shorter switching time can reduce the power consumed by the transistor. That is why, this power dissipation should be lessened. In rising time, the switching time faster and more efficient than in falling time because the effect on applying V_{BS} voltage has a positive impact on MOSFET performance in rising time. However, the same situation is not possible in falling time for MOSFET because the power dissipation occurs due to the absence of good switching characteristics in this duration. Therefore, the adaptive circuit design is needed for reducing the undesirable effect of this structure.

$$t_1 = R_G \cdot C_{iss} \cdot ln\left(\frac{1}{1 - \frac{V_{TH}}{V_{GS}}}\right) \qquad (5)$$

where C_{iss} is input capacitance, V_{GS} is gate-to-source voltage. Also, R_G is the resistance of drain terminal. t_1 isthe time where V_{TH} is only the parameter for switching the MOSFET in Fig. 2a.

$$t_2 = R_G \cdot C_{iss} \cdot ln\left(\frac{1}{1 - \frac{V_{GP}}{V_{GS}}}\right) \qquad (6)$$

where V_{GP} is gate to plateu voltage. Ciss is input capacitance. t2 is the duration where V_{GP} and V_{GS} are two parameters which determine the length of this duration.

$$t_3 = R_G \cdot C_{gd} \cdot \left(\frac{V_{DS}}{V_{GS} - V_{GP}}\right) \qquad (7)$$

in which V_{DS} is the drain-to-source voltage. t_3 is the time where V_{DS} , V_{gp} and V_{GS} constitute this duration. C_{gd} represents gate-to-drain capacitance.

$$t_4 = R_G \cdot C_{gd} \cdot ln\left(\frac{V_{GS}}{V_{GP}}\right) \qquad (8)$$

t_4 is the duration where only the effect of V_{GS} parameter is dominant. C_{gd} represents gate-to-drain capacitance.

$$t_5 = R_G \cdot C_{gd} \cdot \frac{V_{DS}}{V_{GP}} \qquad (9)$$

t_5 is the time where V_{GP} and V_{DS} are effective. C_{gd} represents gate-to-drain capacitance.

$$t_6 = R_G \cdot C_{iss} \cdot ln\left(\frac{V_{GP}}{V_{TH}}\right) \qquad (10)$$

t_6 is the duration where V_{TH} affects the duration of this time. V_{TH} is threshold voltage of the transistor. C_{iss} represents total input capacitance.

From Equation (4), it can be observed that when the bulk-terminal voltage increases, the rising time shortens. By considering this approach, it can be commented that V_{BS} is lessened in the rising time. When the bulk-terminal voltage is increased, the power consumption is also decreased in rising time. However, the bulk-terminal voltage expands falling time, the power consumption is also increased in failing time because the high V_{BS} voltage values adversely impact the switching time of the MOSFET in falling time and it causes the increase in power consumption in MOSFET. In rising time, the bulk-terminal voltage should be increased. Whereas, V_{BS} must be decreased in falling time.

2.2 Buck Converter Circuit Design

The buck converter is shown in Figure 3. It is the com-mon topology for employing power distribution cir-cuits, development boards, etc. It ensures the required local voltage values from higher voltage values in the system. A typical converter includes an active and controlled switch, rectifier elements (diode e.g.), ca-pacitors and inductors. The basic structure of the con-verter permits the achievement of high efficient power characteristics with the design. The buck converter contains the inductor on the output of the buck con-verter that yields a regulated output current to the load. This seems to beadvantageous in terms of achieving high efficient converter design. However, some specific conditions may appear, and these issues should be taken into consideration during the design procedure. The input is applied to switching device and the behavior of input current has active waveform. This situation has the negative effect on converter since the controlled current spreads out the noise into all system. To eliminate this undesired impact, the appropriate decoupling is indispensable for converter. Therefore, capacitor is an important portion of converter structure.

It was also promising for applying this idea to the buck converter topology. When the basic structure of buck converter is simple, the extra advantage of the effect of bulk terminal voltage for buck converter has become more competitive comparing with converter structures.

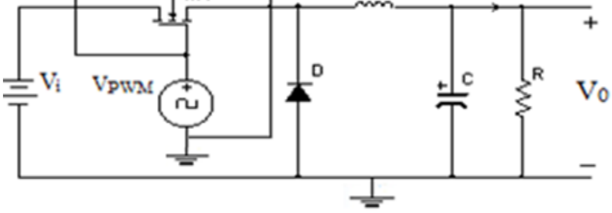

Figure 3. The proposed DC-DC Buck Converter

Two circuit topologies are analyzed and examined for understanding the effect of bulk-terminal voltage on a proposed DC-DC Buck Converter. Each circuit is analyzed and simulated with PSPICE. The proposed converter has depicted on Fig. 3. Transistor M_1 that has four terminals is switching element. M_2 and M_3 connected bulk terminal of M1 are voltage divider circuit. There are M_2 and M_3 MOSFETs that represent resistors in the voltage divider circuit.

A low amplitude voltage that is synchronized with the PWM signal VPWM is applied to the bulk terminal of M1 by the voltage divider circuit. Thus, the threshold voltage of the transistor M1 is changed simultaneously with the PWM signal. The W/L equations wereformulated for TSMC 0.13 μm technology. Drain currents I_{D2} and I_{D3} for M2 and M3 given as,

$$I_{D2}=\frac{1}{2}k_n\frac{W_2}{L_2}\cdot(V_{GS2}-V_{TH2})^2 \quad (11)$$

$$I_{D3}=\frac{1}{2}k_n\frac{W_3}{L_3}\cdot(V_{GS3}-V_{TH3})^2 \quad (12)$$

where I_{D2} and I_{D3} are drain currents of M2 and M3 respectively. V_{GS2} and V_{GS3} are gate-source voltages, W_2/L_2 and W_3/L_3 are aspect ratios of M_2 and M_3. The transconductance parameter represents kn. Also, V_{TH2}, V_{TH3} are the threshold voltages of M_2 and M_3, respectively. Because M_2 and M_3 are identical, then, $V_{TH2}= V_{TH3}$ and $I_{D2}=I_{D3}$. Also, $V_{GS2}= V_{PWM} - V_{BS}$ and $V_{GS3}= V_{BS}$ where V_{BS} is equal to V_B-V_S as shown in Figure 3. V_{PWM} is PWM voltage. Therefore, the equation can be written as bulk-source voltage V_{BS} of M_1:

$$V_{BS}=\sqrt{\frac{2I_{D3}}{k_n(W_3/L_3)}}+V_{TH3} \quad (13)$$

wherein the bulk current has been neglected because it is very small compared to I_{D2}.It is also important to determine ideal value of inductor L and capacitor C for the proposed converter because the voltage or current which is charging on capacitor or inductor may reduce the output voltage or output current. The next step is to calculate the duration in which the switch is ON, OFF and total time in DC-DC Buck Converter Design. In the proposed design, input voltage is selected as V_i=10V and the output voltage is selected as V_0=3.3V. The output voltage is adjusted as 3.3 V because many electronic systems such as microprocessors, communication and mobile application systems work with 3.3V. Therefore, it is preferred this voltage level. Also, the input voltage can be selected at a different value. For these requirements, the inductor value, switching frequency, the capacitor value is calculated via formulas. The value of inductor and capacitor calculations are given as in detail as Equation 14 and 15.

The inductor value which is used in circuit is calculated as given by,

$$L=\frac{3.33\cdot V_o\cdot(t_{total}-t_{on})}{I_0} \quad (14)$$

In Equation (14), the output current ripple ratio is taken as a constant 0.3 in buck converter design. Therefore, this value can be written as a 3.3 in nominator [23].

The capacitor value which is used in circuit is calculated as given by,

$$C=\frac{V_o\cdot(V_i-V_o)}{8\cdot L\cdot f_s^2\cdot V_i} \quad (15)$$

The output current I_0 of proposed buck converter is calculated from Equation (16).

$$I_0=\frac{V_0}{R} \quad (16)$$

The output voltage can be found by Equation (17).

$$V_o=D\cdot V_i \quad (17)$$

where V_{in} represents input voltage and D is duty cycle of buck converter when all losses are ignored.

An input power of converter can be calculated by Equation (18).

$$P_i=D\cdot V_i\cdot I_0 \quad (18)$$

in which, D represents Duty Cycle, V_{in} stands for input voltage. Channel voltage which is the voltage drop on transistor M_1 when it is conduction is affected I_0. A similar formula is used for calculating output power of converter given as Equation (19).

$$P_o=V_o\cdot I_0 \quad (19)$$

The efficiency of DC-DC Buck Converter is another critical design criterion for proposed structure. After calculating input and output powers of converter, the efficiency can be calculated by Equation (20).

$$\eta=\frac{P_o}{P_i} \quad (20)$$

3. SIMULATION RESULTS

In this section, it is examined input and output powers of systems for each circuit with using PSPICE. The first circuit can be thought of as a classical DC-DC Buck converter without applying a voltage to the bulk terminal.

The second circuit is the structure that has the optimized performance with its proposed circuit part. In this circuit, the V_{BS} voltage is adjusted to 1.2V with the using Voltage divider circuit. This value is determined by simulating V_{BS} voltage for negative and positive V_{BS} voltages. Figure 4 illustrates the V_{BS} voltage which is applied to bulk terminal of M1 and the threshold voltage variation. The value of V_{BS} is specified as 1.2V. This value is the optimized value for the switching performance for M1. A suitable value for V_{BS} is simulated in PSPICE for positive and negative voltages. As a result, the bigger and the smaller bulk terminal voltage values have less efficient on M1 performance for calculated L and C values. Therefore, the best switching performance appears when the V_{BS} value is 1.2 V for this MOSFET parameters. The switching frequency is selected as 20 kHz. To get V_{BS}=1.2V, voltage divider circuit consisting of M2 and M3 has employed as shown in Figure 3. From equation (A), W_3/L_3 is calculated as 29.5 for I_{D3} =65 μA and kn =27.6 μA/V2. Also, W_2/L_2 is calculated as 0.5. The Figure 4 shows the relationship between V_{BS} and threshold voltage of M1. The primary aim of this study is to design a high-efficiency DC-DC buck converter for low power applications. It should be 3.3V source such as portable system, communication systems. All the design parameters are determined according to DC-DC Buckconverter which has the input voltage V_i=10V and output voltage V_o=3.3 V. Then, the inductor value and the capacitor value of Buck Converter are calculated according to formulas (13), (14) successively where C_{iss} is calculated as 131.12 fF. The switching frequency is taken as 20kHz-100 kHz for switching of M1. The inductor value is calculated and specified as 220 µH and capacitor value is calculated as 40µF. R is selected as 1kΩ. P_{out} is 109 mW, therefore output current will be 33 mA. All these conditions have the effect on working of buck converter and the operation of this circuit structure is directly related with these parameters because, the inductor value should be as small as possible regarding with maximizing output voltage and current. The switching frequency also ought to be selected commonly frequency values. The voltage of M_1 is another critical parameter for operation M_1 safely.

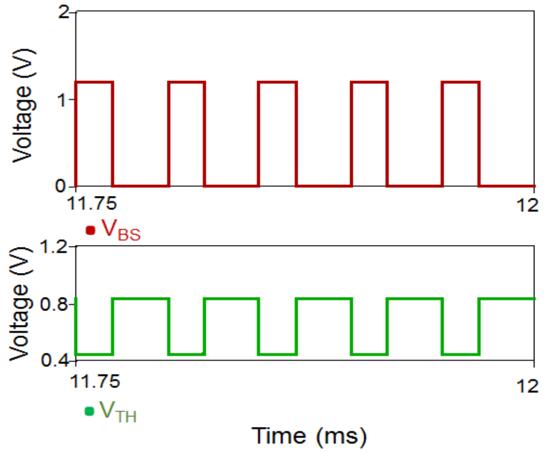

Figure 4. The threshold voltage waveform for proposed buck converter with V_{BS}

This voltage value must be small for getting high performance of MOSFET. All things considered, two circuit structure is simulated via SPICE and the results are evaluated. Figure 5 shows the output voltage of conventional circuit.

It is desired to have the voltage of converter is 3.3 V. This value appears when the duty cycle is 0.395. The theoretical output voltage should be 3.95V when the input voltage 10V.

Figure 6 depicts the output voltage of proposed circuit. The output voltage of this converter is aimed to have 3.3 V. Thisvoltage value occurs when the duty cycle is 0.35. The theoretical output voltage should be 3.5V when the input voltage 10V.

There is a difference between the theoretical and simulation values for conventional buck converter. This is caused by the non-synchronous rectification diode and the current of the converter is small.

Figure 7 displays the output current of proposed circuit. The current of proposed converter is 33 mA when the duty cycle is 0.35.

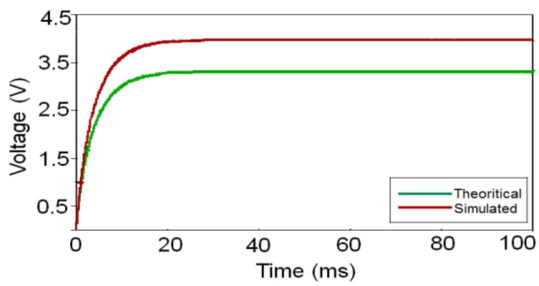

Figure 5. The output voltage of conventional buck converter

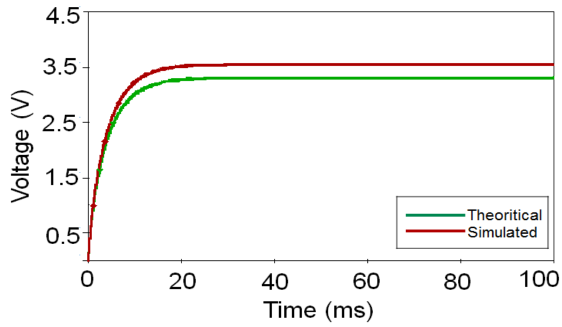

Figure 6. The output voltage of proposed buck converter

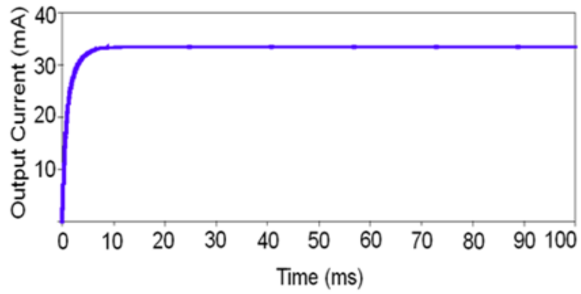

Figure 7. The output current of proposed buck converter

Fig. 8 illustrates the duty cycle- output current characteristics of conventional and proposed circuit designs. It is obvious that when it is compared two circuits, the proposed circuit has higher output current values than conventional circuit.This difference is the effect of applyingbulk-terminal voltage to the bulk terminal of the transistor. With the help of this voltage, the switching performance of the transistor becomes better and the output current of the converter reaches its maximum values compared with conventional circuit. Fig. 9 shows the change in output voltage in two converters for same D value. There is a change in output voltage for proposed circuit. The output voltage should be 10V when the Duty Cycle is taken as 1 since the value of input voltage is 10V, yet this is not same as the Equation (17). The reason for this phenomenon can be explained as the effect of the inductor value, selecting exact value of switching frequency, the voltage of the switching transistor and the diode losses.

The switching frequency also affects the efficiency of the Buck Converter. When the switching frequency increases, there may occur some power consumption owing to high frequency values. The effect on switching frequency is also investigated on the efficiency of the converter. It can be seen that the proposed convertor is more efficient than the conventional converter by applying voltage from bulk terminal. Reducing power consumption with better switching performance is the main goal of this study to increase the total efficiency of the system.

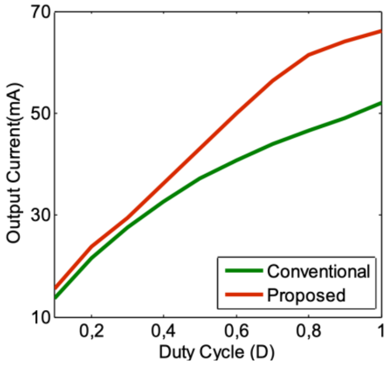

Figure 8. Dutycycle–output current characteristics of two buck converters

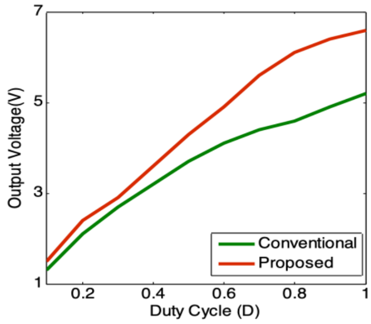

Figure 9. Dutycycle–output voltage characteristics of two buck converters

Figure 10 displays the power consumption distribution on a switching transistor that is simulated in PSPICE. This pattern shows the maximum power dissipation values that the transistor consumes. The Figure 10 A stands for power consumption of switching transistorwhich is used in conventional circuit and the Figure 10 B shows power consumption pattern of switching transistor which is used in proposed circuit. The bulk-terminal voltage on switching transistor has an important impact on power consumption on the converter. The power losses dominantly occur at rising and falling time of switching process for MOSFET. It was calculated the switching power losses in both rising and falling times 7.5 mW and 5mW for classic and proposed buck converters, respectively.

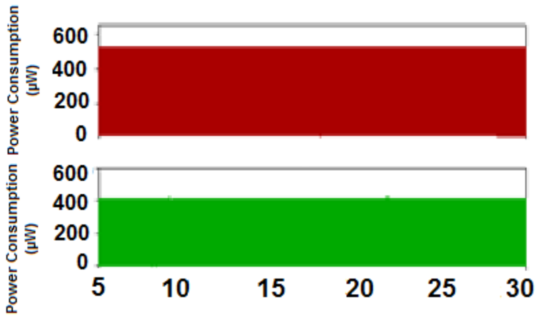

Figure 10. The power consumption distribution on MOSFET

The proposed design increases the efficiency of the suggested structure when it is compared with conventional circuit. This approach would be used in different converter topologies. The main aim of this study is to prove that this design increases the efficiency of the suggested structure when it is compared with conventional circuit.

This approach would be used in different topologies. When it is investigated deeply, the proposed design has larger input voltage/output voltage ratio when it is compared with other converter topologies in Table II. However, minimizing the input voltage can allow having a higher efficiency value for proposed converter. Therefore, the efficiency of novel converter is advantageous in this sense. The converter is also useful as shown in Table II with its simpleness and it is easier to it is easy to control than other converter designs in the literature. The buck proposed converter is advantageous for using in low power applications because it has smaller duty cycle than other converter designs which are listed in Table II. The quantity of power consumption is also another attractive property of this design since it has low power consumption as 1.76 mW. At a first glance, this value seems to be very low when it is taken into consideration the other converter topologies. However, this is reasonable power consumption level for the DC-DC buck converter topology that operates at low power levels. It can also operate at lower duty cycle compared with other converter circuits. The duty cycle of this converter is 0.39. The other converter topologies have bigger duty cycle values than the proposed converter. The exact contribution of this design is to have low power consumption and operate at lower duty cycle compared with other converter topologies in the literature. The output current of buck converter is small in low power applications. Therefore, the output power also becomes small and the efficiency of the converter decreases respectively[30]. The proposed topology is available to develop more stable and efficient converter structure to design more advanced topologies.

3.EXPERIMENTAL RESULTS

The experiments are performed by using two types of MOSFET for both converters. Initially, the classic buck converter with IRLB3034 MOSFET was constructed and some important data are taken to give a detailed form in Table I. The experimental output voltage waveform of the classic buck converter is given in Figure 11.

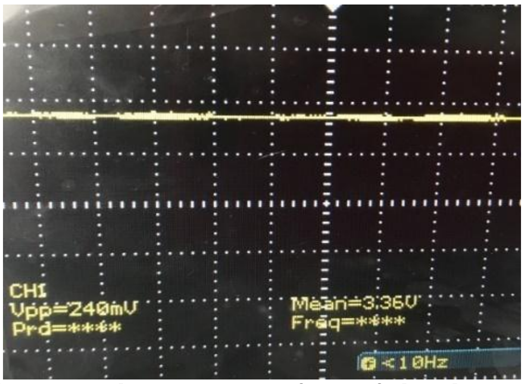

Figure 11. The output waveform of the classic buck converter with the IRLB3034 MOSFET.

In figure 11, the output voltage of this converter is nearly 3.3 V as approved by theoretical approaches. Besides, there appear some undesired ripples on the output voltage of the buck converter. This is an undesirable effect on the performance of the converter. In the second part of the experimental studies, the proposed buck converter was set up by using 4-terminal silicon gate P-Channel

MOSFET (MIC94030). This MOSFET has many advantages in that it has lowresistance value and allows the substrate connection to be distinguished from the source pin. It also has heat management and exhibited low power dissipation during the switching process.The voltage that applied from substrate pin of MIC94030 was calculated from Voltage Divider Circuit. In Fig. 3, there exist two MOSFETs for acting as a resistor.Therefore, it is preferred to use resistors instead of these MOSFETs. To have V_{BS}=1.2V, the resistor values of the Voltage Divider Circuit are specified as R_1=1kΩ and R_2=10KΩ. Theparameters of conventional and proposed buck converters are given in Table 1.

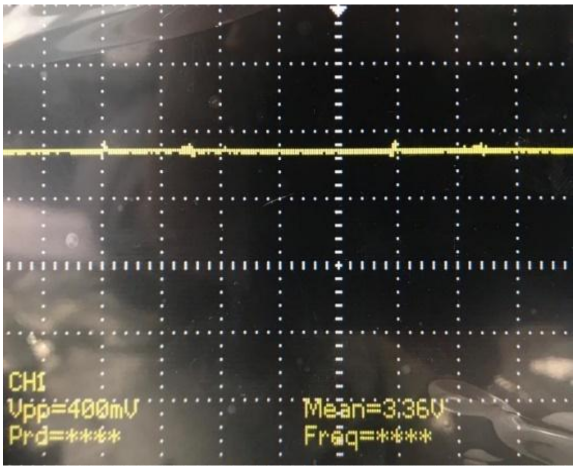

Figure 12. The output waveform of the classic buck converter with the MIC94030 MOSFET.

Figure 12 shows the output waveform of the proposed buck converter with the MIC94030 MOSFET. The output voltage value of the proposed buck converter is approximately obtained 3.3 V which is proved via theoretical results.

The output waveform of the proposed converter has low number of ripples comparing with a conventional buck converter. Also, this converter works at a lower duty cycle when it is set against with conventional buck converter.

Furthermore, the novel converter design is more efficient than the classic buck converter because of the experimental results. This situation provides less power consumption in the converter and this converter performs better than the classic buck converter. Table II illustrates the detailed in formation about these converters. The image of the experimental prototype is given in Figure 13 for proposed the buck converter with 4-pin MIC94030.

Figure 13. The picture of the proposed buck converter with the MIC94030 MOSFET on PCB.

The proposed structure is more efficient than the conventional converter structure for the same values as seen from the Table1.

Table 1. The Specifications for Conventional and Proposed Circuits

	Conventional (Simulation)	**Conventional (Experiment)**	**Proposed (Simulation)**	**Proposed (Experiment)**
MOSFET Type	NMOS	NMOS (IRLB3034)	NMOS	**PMOS (MIC94030)**
Input Voltage	10 V	10 V	10 V	10 V
Inductor	220 µH	220 µH	220 µH	220 µH
Capacitor	40 µF	40 µF	40 µF	40 µF
Output Voltage	3.3 V	3.3 V	3.3 V	3.3 V
Output Current	33 mA	33 mA	33 mA	33 mA
Duty Cycle	0.395	0.41	0.35	0.39
Switching Frequency	20 kHz	20 kHz	20 kHz	20 kHz
Efficiency	82.1	81.5	90.7	88.2
Power Dissipation by MOSFET	1.94 mW	2.44 mW	1.2 mW	1.76 mW

Table 2. Comparison of the Buck Converter Parameters Which Are Selected In Related Papers

	Lindiya [24]	Ito [25]	Woo [26]	Park[27]	Zhang [28]	Su [29]	Proposed
Input Voltage	12V	12 V	1.8 V	2.2V-3.3V	1.8 V	2.5 V	10 V
Inductor (L)	2100 µH	395.8µH	4.7 µH	3 µH	220 µH	N/A	220 µH
Capacitor (C)	100 µF	79.32 µF	4.7 µF	3 µF	1 µF	470 nF	40 µF
Output Voltage	5V	N/A	1V-1.5V	1.7 V	0.3V-0.55 V	0.8V-1.5V	3.3 V
Output Current	N/A	N/A	300 mA	0.01-20 mA	10 mA	8.4 mA	33.6 mA
V_i/V_0 Ratio	2.4	N/A	1.8	1.29	3.27-6	1.66-2.25	3.03
Duty Cycle (D)	0.48	N/A	N/ A	N/A	0.015-0.98	0.5	0.39
Efficiency (%)	N/A	N/A	94	92.4	86	66.7	88.2
Switching Frequency	4.5-4000 kHz	4.4 kHz	1 MHz	2.5 MHz	100 kHz	0.2MHz-1MHz	20 kHz

Table 3. Parameters of MOSFET used in Spice Simulations

MOSFET Model Parameters
MODEL RITSUBN3 NMOS (LEVEL=1 TPG=1 TOX=1.5E-8 LD=2.95E-7 WD=3.00E-7 UO= 726 VTO=1.0 THETA=0.349 RS=27 RD=27 DELTA=2.27 NSUB=1.45E17 XJ=1.84E-7 VMAX=1.10E7 ETA=0.837 KAPPA=0.508 NFS=3E11CGSO=3.4E-10 CGDO=3.48E-10 CGBO=5.75E-10 PB=0.95 XQC=0

The proposed structure is more efficient than the conventional converter structure for the same values as seen from the Table I. The proposed buck converter operates at a lower duty cycle and has low power consumption compared with a conventional buck converter. When it is investigated the Table II, it can be concluded that the duty cycle of the proposed design is lower than [24] and [25]. This corresponds to have higher efficiency for proposed design. This fact shows that the main advantage of the suggested converter is that it allows boosting up the efficiency of the system. The inductor is another parameter for the converter design since it affects the volume of the converter. An input voltage/output voltage ratio is another important parameter which correlates power losses and efficiency. There are also converter topologies which are proposed by Woo [26] and Park [27] has smaller input volt-age/output voltage ratio compared with the proposed circuit. Since this voltage difference between input volt-age and output voltage approximates, it is sensible to reach very high efficiencies in these designs. Since this circuit operates at low power level, the proper efficiency value may not be obtained. Zhang [28] and Su [29] has designed high efficiencies in these designs for digital circuit designs. Since this circuit operates at low power level, the proper efficiency value may not be obtained. Thus, the efficiency level of these designs cannot achieve expected values regarding with other converters in Table-II since the power dissipation of buck converterdecreases with the decline the output current of converter. for proposed design. This fact shows that the ma-in advantage of the suggested converter is that it allows boosting up the efficiency of the system.

The proposed design increases the efficiency of the suggested structure when it is compared with conventional circuit. This approach would be used in different converter topologies. The main aim of this study is to prove that this design increases the efficiency of the suggested structure when it is compared with conventional circuit.

This approach would be used in different topologies. When it is investigated deeply, the proposed design has larger input voltage/output voltage ratio when it is compared with other converter topologies in Table II. However, minimizing the input voltage can allow having a higher efficiency value for proposed converter. There-fore, the efficiency of novel converter is advantageous in this sense. The converter is also useful as shown in Table II with its simpleness and it is easier to it is easy to control than other converter designs in the literature. The buck proposed converter is advantageous for using in low power applications because it has smaller duty cycle than other converter designs which are listed in Table II. The quantity of power consumption is also another attractive property of this design since it has low power consumption as 1.76 mW. At a first glance, this value seems to bevery low when it is taken into consideration the other converter topologies. However, this is reasonable power consumption level for the DC-DC buck converter topology that operates at low power levels. It can also operate at lower duty cycle compared with other converter circuits.

The duty cycle of this converter is 0.39. The other con-verter topologies have bigger duty cycle values than the proposed converter. The exact contribution of this de-sign is to have low power consumption and operate at lower duty cycle compared with other converter topologies in the literature. The output current of buck converter is small in low power applications. Therefore, the output power also becomes small and the efficiency of the converter decreases respectively [30]. The proposed topology is available to develop more stable and efficient converter structure to design more advanced topologies.

4. CONCLUSIONS

In this work, a highly efficient and simple DC-DC Buck Converter is simulated and designed for mobile applications and microcontroller circuits with output voltage 3.3 V and input voltage 10V. The simulations and experiments are performed to validate the efficiency and performance of both converters. The simulations are performed in PSPICE for conventional and proposed circuits. Also, the experiments are performed for classic and proposed boost converter successively. The pro-posed converter efficiency is reasonable considering its simple circuit structure. It is concluded that the efficiency of the DC-DC Buck Converter increases with a applying bulk-terminal voltage signal on a MOSFET. The pro-posed buck converter operates at a lower duty cycle and has low power consumption. This is the result of the threshold voltage effect on MOSFET performance. The size of buck converter circuit elements is also minimized by specifying the proper switching frequency, the value of inductor and the value of capacitor. The efficiency of the converter will be improved by using different circuit structures which are low-power consumption. This topology is also suitable for CMOS integrated circuit structure. In conclusion, this proposed design can be used in microprocessors, portable devices, solar systems and embedded integrated circuits.

REFERENCES

[1] M. H. Rashid, *Power Electronics Handbook*, Aca. Pre. Ser. in Eng. 2011.

[2] N. Safari, Design of a DC/DC buck converter for ultra-low power applications in 65nm CMOS Process, Master thesis in Department of Electrical Engineering, Linköping Institute of Technology, 2012:54.

[3] İ.Büyükkeskin, , S. A.Tekin, , S.Gürel, M. S. Genç, Electricity Production from Wind Energy By Piezoelectric Material. *International Journal of Renewable Energy Development*, 8(1), pp41-46, 2019.

[4] S. Evanczuk, “Buck Converters Simplify Energy Harvesting from High-Input-Voltage-Transducers”. *Digi-key Electronics*,vol 1, 2013.

[5] M. Z. Hossain, N. A. Rahim, J. L. Selvaraj, Recent progress and development on power DC-DC converter topology, control, design, and applications: A review, *Renewable and Sustainable Energy Review*, vol.81, pp.205-230, 2017.

[6] C. Hua, Y. A. Deng, A Novel Dual-Bridge LLC Resonant Converter with Wide Range of Low Input Voltage”, *Energy Procedia*, pp.361-365,2019.

[7] N. Zhang, D. Sutanto and K. M. Muttaqi, “A review of topologies of three-port DC–DC converters for the integration of renewable energy and energy storage system”, *Renewable and Sustainable Energy Review*, vol.56, pp.388-40, 2015.

[8] D. Guilbert, S. M. Collura, A. Scipioni, DC/DC converter topologies for electrolyzers: State-of-the-art and remaining key issues, *International Journal of Hydrogen Energy*, vol.42,pp.23966-23985, 2017.

[9] S. Arruugam, P. Logmani, Modeling and adaptive control of modified LUO converter, *Microprocessors and Microsystems*, vol. 56, 102889, 2019.

[10] A. Amir, A. Amir, H. S. Che, A. Elkhateb, N. A. Rahim,Comparative analysis of high voltage gain DC-DC converter topologies for photovoltaic systems, *Renewable Energy*, vol.136, pp.1147-1163,2018.

[11] J. S. Lopez, I. P. F. Donoso, L. M. F. Morais, P. C. Cortizo, M. A. Sever, Digital control strategy for a buck converter operating as a battery charger for stand-alone photovoltaic systems, *Solar Energy*, vol.140, pp.473-487, 2016.

[12] H. Luo, H. Wen, X. Li, L. Jiang, Y. Hu, Synchronous buck converter based low-cost and high-efficiency sub-module DMPPT PV system under partial shading conditions, *Energy Conversion and Management*, vol.126, pp.473-487,2016.

[13] M. Gupta, S. p. Phulambrikar,” Design and analysis of Buck Converter”, *International Journal of Engineering Research and Technology*, vol.3, no.3, pp.2346-2350, 2014.

[14] F. Khateb, Bulk-driven floating-gate and bulk-driven quasi-floating gate techniques for low-voltage low-power analog circuit design., *AEU- International Journal of Electronics and Communications*, vol.68, no.1, pp.64-72, 2014.

[15] J. F. Da Rocha, N. B. Dos Santos, J. M. D. Costa, Voltage Spikes in Integrated CMOS Buck DC-DC Converters: Analysis for Resonant and Hard Switching Topologies, *Procedia Technology*, vol.17, pp.327-334,2014.

[16] V. R. K. Kanamarlapudi, B. Wang, N. K. Kandasamy, P. L. So, A New ZVS Full-Bridge DC–DC Converter for Battery Charging with Reduced Losses Over Full-Load Range, *IEEE Transactions on Industry Applications*, vol.54, no.6, pp. 571-579,2018.

[17] E. H. Ismail, M. A. Al-Saffar, A. J. Sabzali, High Conversion Ratio DC–DC Converters with Reduced Switch Stress, *IEEE Transactions on Circuits and Systems-I, Regular Paper*, vol.55, no.7,pp.2139-2151,2008.

[18] D. Oulad-Abbou, S. Doubabi, A. Rachid, Power switch failures tolerance of a photovoltaic fed three-level boost DC-DC converter, *Microelectronics Reliability*, vol.92, pp.87-95, 2018.

[19] Khateb, D. Biolek, “Bulk-Driven Current Differencing Transconductance Amplifier,*Circuits, Systems, and Signal Processing*, vol.30, pp.1071-1089, 2011.

[20] S. Gurel, S. A. Tekin, “The New Approach for Switching Performance of Power MOSFET”, *Innovative Applications in Engineering*, pp. 95-100, 2018.

[21] H. Ercan, S. A. Tekin, M. Alçı, “Low-voltage low-power multifunction current-controlled conveyor”, *International Journal of Electronics*, vol.102, no. 3, pp. 444-461, 2014.

[22] A. S. Sedra, K. C. Smith, T. C. Carusone, V. Gaudet, *Microelectronic Circuits*, New York: Oxford University Press, 2016.

[23] Power MOSFET Basics: Understanding Gate Charge andUsing it to Assess Switching Performance.*VISHAY SILICONIX, Device Application Note AN698A*. pp.1-6,2016.
[24] A. Lindiya, D. S. Palani, a. Iyyappan, Performance Comparison of Various Controllers for DC-DC Synchronous Buck Converter, *Procedia Engineering*, vol.38, pp.2679-2693, 2012.
[25] D. Ito, H. Asahara, T. Kousaka, T. Ueta, Clock pulse modulation for ripple reduction in-buck-converter circuits, *Chaos, Solitons & Fractals*, vol.111, pp.138-145, 2018.
[26] X. Zhang, P. Chen, Y. Okama, K. Ishida, Y. Ryu, K. Watanabe, T. Sakurai, M. Takamiya, A 0.6 V Input CCM/DCM Operating Digital Buck Converter in 40 nm CMOS, *IEEE Journal of Solid -State Circuits*, vol.49, no.11, pp.2377-2386,2014.
[27] L. Su, D. Ma, A. P. Brokaw, Design and Analysis of Monolithic Step-Down SC Power Converter With Subthreshold DPWM Control for Self-Powered Wireless Sensors, *IEEE Transactions on Circuits and Systems-I :Regular Papers*, vol.57, no.1, pp. 280-290, 2010.
[28] K. Woo, Y. Oh, B. Yang, "DC-DC Buck Converter Using Analog Coarse-Fine Self-Tracking Zero-Current Detection Scheme", *IEEE Transactions on Circuits and Systems-II:Express Briefs*, vol.66, no.11, pp.1850-184, 2019.
[29] Y Park, H. Kim, S. Kim, Y. Pu, K. Hwang, Y. Yang, M. Lee, K. Lee, A Design of a 92.4% Efficiency Triple Mode Control DC–DC Buck Converter with Low Power Retention Mode and Adaptive Zero Current Detector for IoT/Wearable Applications, *IEEE Transactions on Power Electronics*, vol.32, no. 9, pp.6946-6960, 2017.
[30] F. Santoro, R. Kuhn, N. Gibson, N. Rasera, T. Tost, D. Schmitt-Landsiedel, R. Brederlow, "A 92.1% Efficient DC-DC Converter for Ultra-Low Power Microcontrollers with Fast Wake-up" *2017 IEEE Custom Integrated Circuits Conference*, pp. 1-4, 2017.

Research Article *Energy, Environment and Storage* (2022) 02-02:41-53

Energy, Environment and Storage

JournalHomepage: www.enenstrg.com

Pre-Pilot Scale Microencapsulation of Phase Change Materials for Thermal Energy Storage Applications.

B. Srinivasaraonaik[1*],Rachit Agarwal[1],Gargi Mittal[1], L.P. Singh[2]

[1*]*Innovative Building Materials, CSIR- Central Building Research Institute, Roorkee, 247667, India*

[1]*Innovative Building Materials, CSIR- Central Building Research Institute, Roorkee, 247667, India*

[2]*Department of Basic and Applied Sciences, GuruGobind Singh Indraprastha University, New Delhi, India* [2]*ORCID:0000-0003-0026-7592*

ABSTRACT. Most of the researcher has attempted for the encapsulation of phase change materials in small scale for the thermal storage applications. However, energy conversion in field applications require enormous quantity of thermal energy storage materials. In this paper, a pre-pilot scale is developed for encapsulating of various binary mixtures using an in-situ polymerization technique.DSC, TGA, FTIR, XRD, and FE-SEM were used to delineate the thermal properties of obtained microcapsules in order to identify shape, mean size, functional groups, crystalline state, and weight loss of distinct microcapsules. The results show that the synthesized microcapsules were regular in shape and smooth and well encapsulated around cores. The thermal properties of different microcapsules are 34.9 ℃, 95.3 kJ/kg and 35.6 ℃, 98.5 kJ/kg resultant to microencapsulation of 75% Stearic acid (SA) + 25% Capric acid (CA) and 63% Capric acid (CA) + 37% Palmitic acid (PA),respectively. The encapsulation efficiencies were 78.2% and 73.09%. The yieldof the products are attained ~82%.

Keywords:Binary mixture; encapsulation ratio; thermal properties; energy conversation; pre-pilot scale.

Article History: Received: 25.03.2022; Revised: 18.04.2022; Accepted: 17.05.2022; Available online: 18.05.2022
Doi: https://doi.org/10.52924/AALV5824

Nomenclature

CA	Capric acid
MF	Melamine-Formaldehyde
MPCM	Microencapsulated Phase Change Materials
MUF	Melamine-Urea-Formaldehyde
PA	Palmitic Acid
PCMs	Phase Change Materials
PMMA	Poly-Methyl Methacrylate
PS	Poly styrene
SA	Stearic acid
TSM	Thermal Storage Materials
TST	Thermal Cycle Test
UF	Urea-Formaldehyde

1. INTRODUCTION

Energy crisis is gradually increasing particularly in industries, residential and commercial buildings, which may lead to depletion of fossil fuels and greater impact on global warming. Advanced thermal storage materials are being integrated into various sectors such as solar energy capture, buildings, textiles, transportation shelter, etc. Thermal storage materials (TSM) are phase change materials (PCMs) which has high energy density at constant temperature. PCMsabsorbs the heat from environment during phase transition from solid to liquid and vice-versa [1, 2]. These PCMs are commercially available in the market. The researchers are choosing the PCMson the basis of low cost, superior thermal properties, availability and nontoxicity [3, 4].PCMs are integrated in heat storage systems in three ways such as immersion, macro-encapsulation, and microencapsulation. In the immersion process, the PCM was infused into the cementitious material by capillary action aided by vacuum. This process was not stable owing to liquid leakage during phase transition [5]. The macro-encapsulation of PCMs has poor thermal conductivity, which need to be protected against annihilation and more workers are required to install in storage systems. PCMs are employed as the core in microencapsulation, and that they are surrounded by a shell made of either polymer or inorganic material, which is synthesized through physical and chemical processes. It prevents the leakage during phase transition, provides a high heat transfer rate, and capable of resisting volume change during phase transition [6]. Microencapsulation of PCMs were formulated in two ways, one is physical and another is chemical. The physical method includes spray drying whereas chemical methods include in-situ polymerization, complex

*Corresponding author: srinivas@cbri.res.in

coacervation, phase separation, and suspension-like polymerization [7-9]. Microencapsulation of PCMs has wide applications, particularly in cementitious materials owing to 30–40% of total energy consumption [10]. Generally, the core materials are fatty acids, paraffin, eutectic mixture, and salts whereas shell material are Polystyrene (PS) [11-13],Poly-Methyl Methacrylate (PMMA) [14], Melamine-Urea-Formaldehyde (MUF)[15-17], Melamine-Formaldehyde (MF) [18]. The long-term viability of thermal storage systems is determined on the durability of PCMs. It has a significant impact on the PCMs' service life. As a result, researchers conducted a thermal cycle test (TST) to assess the PCMs' service life. Yang et al., [19]performed accelerating test of different fatty acids such as lauric acid, myristic acid, palmitic acid and stearic acid. They have concluded that thermal properties of fatty acids have not changed significantly after 10,000. Shilei et al., [6] conducted TST oneutectic combination of capric and lauric acid. After 360 cycles of accelerated testing, there was no substantial change in the eutectic mixture. Chinnasamy andAppukuttan [20] determined thermal properties of eutectic mixture of lauric acid / myristyl alcohol after 1000 cycles. It was determined that, there was no change observed in thermal properties. Thermal characteristics of a eutectic mixture of lauric acid/1-tetradeconal were found to be stable up to 90 thermal cycle tests by Zuo et al [21]. Zhang et al. [22] combined PCMs with lauric acid, myristic acid, and palmitic acid to create a ternary mixture. Melting point and fusion heat were found to be steady for up to 50 cycles.According to a literature review, the thermal characteristics of fatty acids remained steady for a duration of 10000 cycles, implying that fatty acids had a 27-year life span.

Researchers are preparing MPCMs in lab size using the scientific methodologies mentioned above. It is a lengthy and time-consuming procedures.Microtek-BASF preparing these MPCMs with help of Spray dryer technique (physical process) required desired phase change temperature range at large scale. It is non-economical process at lab level.However, practical applications, such as pre-pilot lab experiments on solar thermal energy systems, textiles, solar water heating systems, transportation shelters, and prototype structures, necessitate a massive amount of MPCMs.Among the physical and chemical methods, *in-situ* polymerization technique is adopted for pre-pilot scale preparation of MPCMs. This method is very feasible and economic process at lab level.

In the present work, a pre-pilot scale in-situ polymerization for encapsulation of fatty acid mixtures were prepared using existing governed model. In that, two binary mixtures such as 75% SA + 25% CA and 63% CA + 37% PA fatty acids mixtures were used as core whereas, Melamine-Formaldehyde (MF) used as polymer shell. Designed the batch agitator vessel based on density and viscosity of the materials.The description of the agitator vessel has described below Fig.1 and 2.

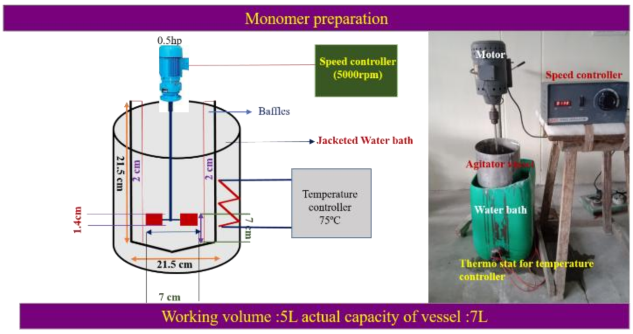

Fig. 1. Melamine –Formaldehyde Monomer preparation.

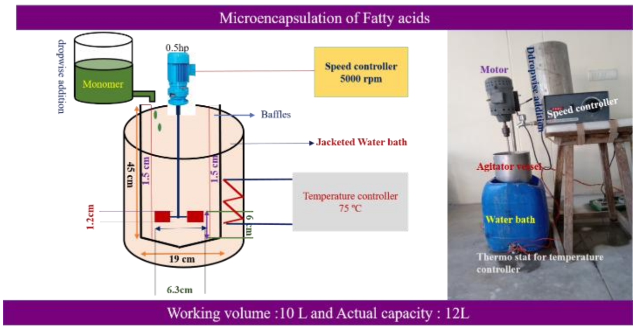

Fig. 2. Bulk scale preparation of microencapsulation of fatty acids.

Two categories of agitator vessel have been designed and developed. One was used for monomer preparation. Another was 12 L capacity of agitator vessel which was used for microencapsulation process. In situ–polymerization technique is thermal process for that the agitator vessels were placed in temperature controller water bath. Temperature was controlled with help of thermostat connected to the water bath.

The agitator vessels were designed using the following equations

$$\frac{H}{Dt} = 1 \quad (1)$$

$$\frac{J}{Dt} = \frac{1}{12} \quad (2)$$

$$\frac{W}{Da} = \frac{1}{5} \quad (3)$$

$$\frac{Da}{Dt} = \frac{1}{3} \quad (4)$$

$$\frac{E}{Dt} = \frac{1}{3} \quad (5)$$

$$\frac{L}{Da} = \frac{1}{3} \quad (6)$$

Where H is the height of agitator vessel, Dt diameter of agitator vessel, J is width of the vessel, Da is diameter of impeller, W is the width of the impeller blade, E is distance from bottom of the tank to impeller, L is length of the impeller blade.

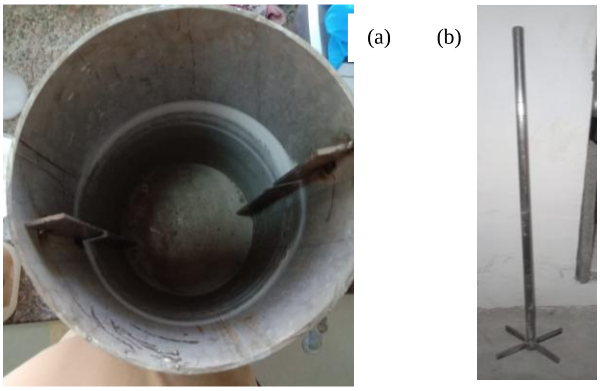

Fig. 3. Attachment of (a) Baffles (b) Impeller in Agitator vessels.

To avoid vortex in the agitator vessel, two baffles were installed Fig. 3. Open straight blade turbine is connected to shaft to the motor for agitation of viscous liquids. The power consumption of the agitator vessel has been determined using following equation

$$P = \frac{k_T n^3 D_a^5 \rho}{g_C} \qquad (7)$$

Where P is power consumption, K_T is impeller constant factor 1.27, n is rotational speed, D_a is diameter of agitator vessel, ρ is density of solution [23]. The designed and developed agitator vessel was presented in Fig.1 and 2 and the dimensions were given in table 1.

Table 1 Dimension of different agitator vessel

Dimension of monomer Agitator vessel	
Total Volume	7 L
Working volume	5 L
Height of agitator vessel	215 mm
Diameter of agitator vessel	215 mm
Width of the baffles (4Nos)	20mm
Diameter of the impeller	70mm
Width of the impeller blade	14mm
Length of the impeller blade	17.5 mm
Motor capacity	0.5 HP

Dimension of encapsulation Agitator vessel	
Total Volume	12 L
Working volume	10 L
Height of agitator vessel	450 mm
Diameter of agitator vessel	190 mm
Width of the baffles (4Nos)	15mm
Diameter of the impeller	63 mm
Width of the impeller blade	12 mm
Length of the impeller blade	15.8 mm
Motor capacity	0.5 HP

2. MATERIALS ANDMETHODS

2.1Materials:

Two kinds of eutectic mixture such as 75% Stearic acid (SA) + 25% Capric acid (CA), 63% Capric acid (CA) + 37% Palmitic acid were used as cores. The SA, CA and PA were purchased from Loba Chemie Pvt. Ltd Mumbai and Fisher Scientific Mumbai (India) Mumbai respectively. Their thermal properties were given in table 2. Melamine, and aqueous Formaldehyde procured from Loba Chemie Pvt. Ltd., Mumbai, was used as the shell. Sodium Dodecyl Sulfate (SDS) was obtained from Fisher Scientific, Mumbai (India) is an anionic surfactant used as emulsifier for the formation of the emulsion. Sodium carbonate anhydrous (Na_2CO_3) was procured from Merck, New Delhi used for maintaining basic medium, and Sulfuric acid (H_2SO_4) was purchased from Thomas baker, Mumbai (India) used for maintaining acidic medium for microencapsulation. Ethanol was purchased from Fine Chemical Co. Ltd used to remove unencapsulated PCM.For distinct solutions, two agitator vessels have been conceived and built. One was used to prepare monomers. Another was a microencapsulation agitator vessel with a capacity of 12 L. The agitator vessels were placed in a temperature-controlled water bath for the in situ–polymerization procedure, which is a thermal process. A thermostat connected to the water bath was used to regulate the temperature.

Table 2 Thermal properties of fatty acids

S. No	PCM	M.P (℃)	L.F (kJ/kg)	Ref.
1.	75% SA+25% CA	35	121.80	[24]
2.	63% CA+37% PA	36.2	134.75	[25]

2.2 Preparation of emulsion of different fatty acids

400–500 g of different eutectic mixtures was mixed with 5–7 L distilled water in a 12 L capacity of agitator vessel. The eutectic mixture heated at different melting range of 35–70 ℃ until solid becomes liquid in agitator vessel. 16–20 g of SDS was then added in the liquid solution and the solution was stirred using mechanical stirrer for 1h to make a stable emulsion. The optimized parameters for microencapsulation of PCMs such as pH 3.2, agitator speed 5000 rpm and temperature 75 ℃, core to shell ratio and composition were adopted from the previous study conducted by Srinivasaraonaik et al[24, 25]. The chemical composition of different PCMs has been provided in Table 3.

Table 3 Chemical composition of raw materials

S.No.	PCM (core) (g)	Melamine (g)	Formaldehyde (ml)	SDS (g)
1.	75% SA+25% CA (400)	160	300	16
2.	63%CA+37%PA (500)	200	375	20

2.3 Preparation of MF monomer

160–200 g of Melamine, 300–375 mL of formaldehyde and 5 L distilled water were taken in a 7L capacity of agitator vessel. The pH of the solution was adjusted to 8.8 using 10% sodium carbonate solution. The mixture was heated and stirred at 75 ℃ until it becomes transparent. The transparent colour represents the MF monomer.

2.4*Preparation of Microencapsulation of PCM*

The initial pH of the obtained emulsion was about 5. The pH of eutectic emulsion was adjusted from 5 to 3.2 by using 5% solution of sulfuric acid and the solution was heated up to 75 ℃ using thermostat (Fig. 1). The MF monomer was added dropwise into the emulsion of the eutectic mixtures and the mixture of MPCM was stirred and heated continuously for 5 hours. After 5 h, The obtained solution was cooled to room temperature. The obtained microcapsules were filtered with the help of vacuum filtration unit and laved with ethanol solvent to remove unencapsulated PCMs. The wet microcapsules were dried in the oven at 60 ℃ until completely moisture was removed on surface of the polymer (Fig. 4).

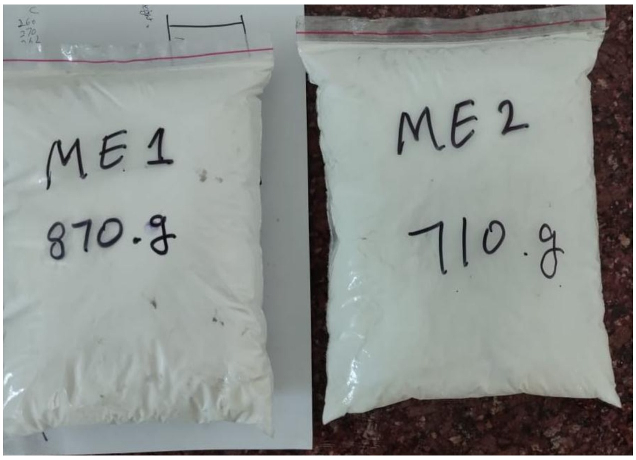

Fig. 4. Product of microencapsulation of (a) 75% SA + 25% CA (b) 63% CA + 37% PA.

2.5Charging and discharging of eutectic mixture of 63% CA + 37% PA

10 g of raw eutectic mixture and microencapsulated 63% CA + 37% PA was taken in various test tubes. These test tubes were placed in 500 mL capacity of water beaker. The calibrated K-type thermocouples were positioned in distinguish test tubes for measuring charging and discharging temperature of the samples. These thermo couples were connected to temperature data logged system. These samples were placed on a magnetic stirrer with a temperature controller. The magnetic stirrer temperature was raised to 50 $^{\circ}$C and the charging temperature recorded to until solid completely becomes liquid. When the test tubes are engaged in ambient conditions, the discharge temperature is recorded.

3.Characterization Techniques

The obtainedmicrocapsules of different eutectic mixtures were characterized by Field Emission Scanning Microscope (FESEM), X-Ray Diffraction (XRD), Fourier Transformation Infrared Spectroscopy (FTIR), Thermogravimetric / Differential Thermal Analysis (TG / DTA), Differential Scanning Calorimeter (DSC).

3.1 Field Emission Scanning Microscope (FESEM)

The morphology of the synthesized microcapsules of different eutectic mixtures were carried out using FESEM (Make: TESCAN, Model: MIRA 3). The synthesized MPCMs adhered to carbon tape which was on the sample holder. The samples were gold-coated by using a sputter coater (Make: Electron Microscopy Sciences, Model: K550X). The samples were analysed for morphological studies and determined average particle size of microcapsule with randomly selected ten microparticles.

3.2 X-ray Diffraction (XRD)

The powdered samples were flattened on a glass slide's sample holder. The mineralogical studies of raw PCMs and different MPCMs have been analysed through X-ray diffraction (Make: Rigaku and Model: Dmax 2200) operated in two theta range of 5–80 degree at the rate of 3 theta / min.

3.3 Fourier Transformation Infrared Spectroscopy (FTIR)

The samples and KBr were grinded and made the pellet with help of pressurized device. The prepared pellets were kept in FTIR (Make: Perkin, Model: Perkin Elmer spectrum version 14) for determining the functional groups attached in SA, CA, LA, eutectic mixture and different MPCMs.

3.4 Thermogravimetric Analysis (TG / DTA)

The thermal stability and percentage of weight loss of different MPCMs have been carried out by using TG / DTA (Make: LINSEIS Model: STA PT 1600) at a constant heating rate of 10 theta / min from temperature range of 50 $^{\circ}$C to 600 $^{\circ}$C

3.5. Differential Scanning Calorimeter (DSC)

The thermal properties such as melting point, latent heat of fusion and specific heat of different MPCMs have been determined with help of DSC (Make: TA instruments Model: Q200) in the presence of Argon at a heating rate of 5 theta / min in the temperature range from 30 $^{\circ}$C to 80 $^{\circ}$C.

4 RESULT AND DISCUSSION

4.1 Morphology of eutectic mixture of microencapsulated PCMs

The morphology of encapsulation of the different eutectic mixtures was presented in Fig 5 (a) and (b). The morphology of microcapsules was observed at the same scale and 10 kV. The shapes of microcapsules are spherical and smooth. The core is well encapsulated in the shell. Randomly different 10 sizes of the samples were selected and determined the mean size of capsules. The mean particle sizesare about 3.6–6 µm and 2.5–4 µm corresponding to encapsulation of 75% SA + 25% CA and 63% CA + 37% PA, respectively.

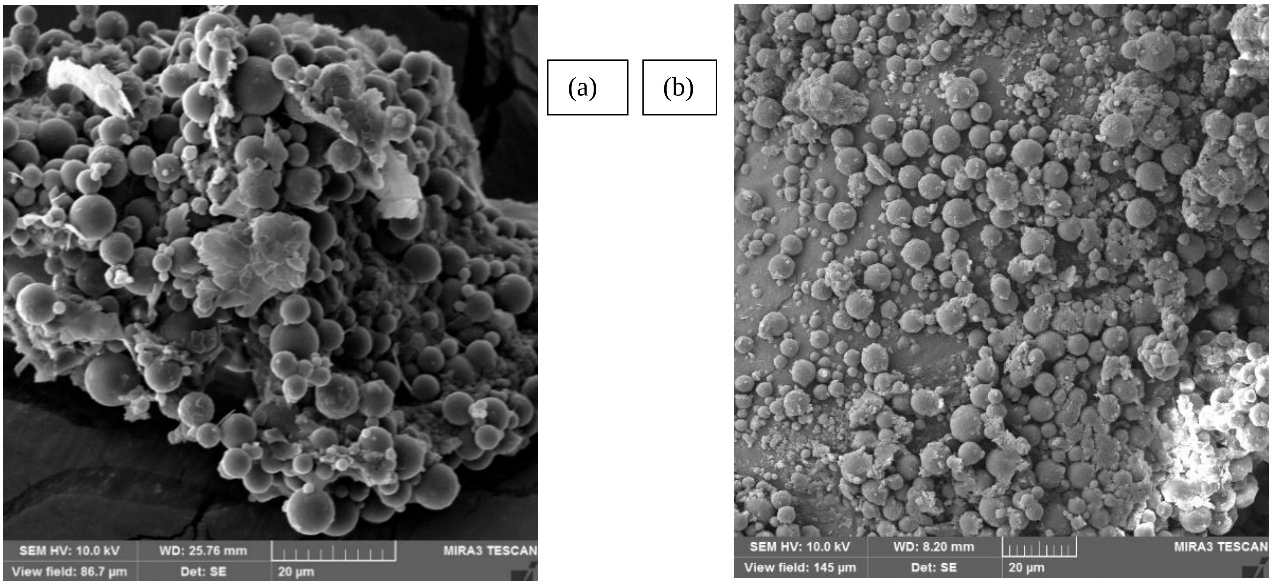

Fig. 5.Morphology of different MPCMS (a) 75% SA + 25% CA (b) 63% CA + 37% PA.

4.2 The FTIR patterns of microencapsulated eutectic mixture with MF shell

The FTIR analysis of shell, core and microcapsules were shown in Fig 6 and 7. The same shell was used for preparation of microencapsulation of eutectic mixture. The spectra of shell are represented in Fig 6 (a) and 7 (a). The stretching of N-H amine functional peak is observed approximately at 3457 cm^{-1}.The stretching vibrations of the C-H group and the C=O group are represented by the intensity peaks at 2945 cm^{-1} and 1710 cm^{-1}, respectively. 1137 cm^{-1} and 820 cm^{-1} are assigned to the C-N stretching bend and aromatic C-H vibrations, respectively. C-H stretching vibrations are represented by the intensity peaks 2918 cm^{-1} and 2852 cm^{-1}. C-H bending vibrations account for the peak at 1432 cm^{-1}. The =C-H alkene group is determined by the intensity peaks 940 cm^{-1} and 726 cm^{-1}.The spectral strong stretching vibration peak C=O is observed at 1702 cm^{-1} in Fig. 6 (b). The spectrum of 63% CA + 37% PA is shown in Fig 7 (b). The intensity peaks 2916 cm^{-1} and 2850 cm^{-1}represent to C-H stretching vibrations. The spectral strong stretching vibration peak C=O is observed at 1698 cm^{-1}. The peak at 1430 cm^{-1} is allocated to C-H bending vibrations. The intensity peaks 944 cm^{-1} and 724 cm^{-1} are the =C-H alkene group is established. The peaks are shown in Fig 6 (b) and 7 (b) almost same with little shifting because of encapsulation efficiency difference. In the distinct microcapsules depicted in Fig 6 (c) and 7 (c), the core and shell peaks are well-defined, and no further peaks were observed. The observed peaks confirm that the distinct cores are properly positioned within the shells and that no chemical interactions have occurred between them.

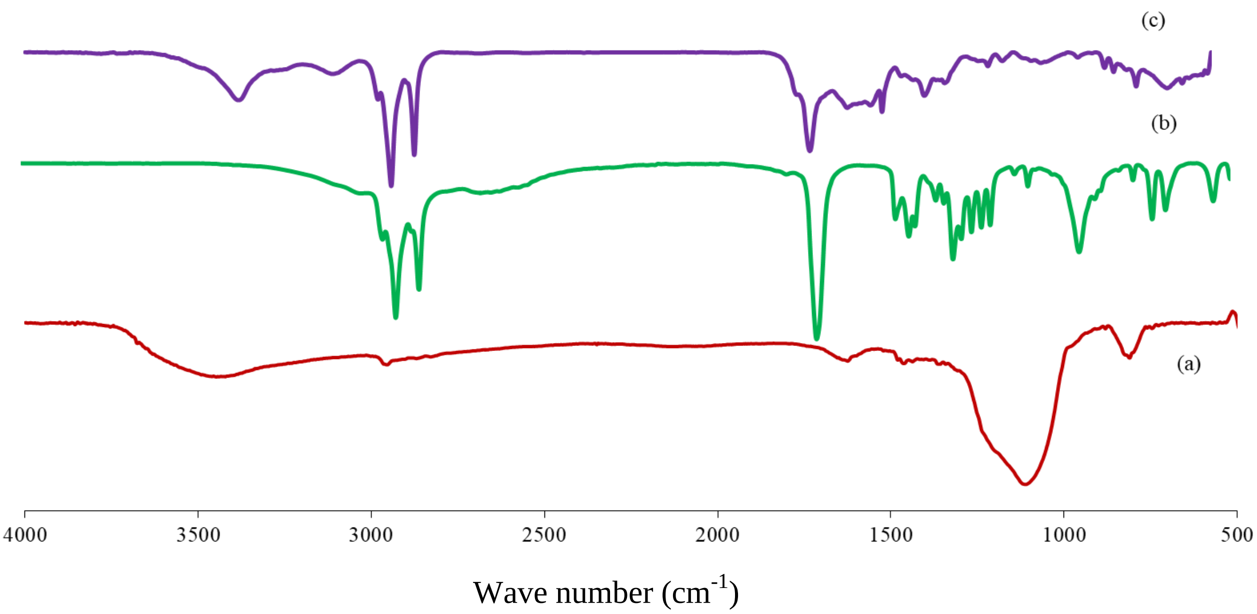

Fig. 6.FTIR analysis (a) MF (b) 75% SA + 25% CA (c) MPCM.

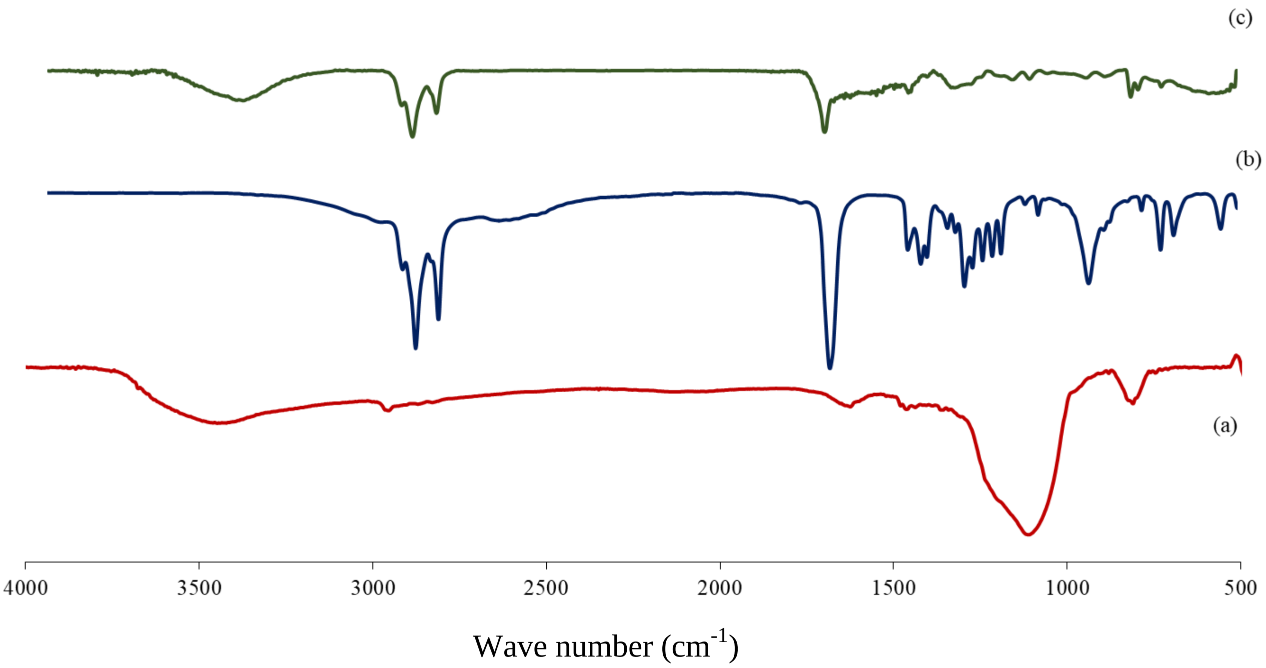

Fig. 7. FTIR analysis (a) MF (b) 63% CA+37% PA (c) MPCM

4.3 XRD patterns of microencapsulated eutectic mixtures

The XRD patterns of core, various eutectic mixtures and encapsulated eutectic mixtures were represented in Fig 8 and 9. The mineralogical study of shell is amorphous characteristic observed in Fig 8 (a) and 9 (a). The minerals peaks of different eutectic mixtures are determined at different 2 theta values. The XRD peaks at 7.2°, 9.1°, 21.72°, and 21.98° are instigated to 75% SA + 25% CA as shown in Fig 8 (b). The XRD peaks at 7.9°, 9.5°, 21.92° and 22° are engendered to 63% CA+37% PA in Fig 9 (b). From the Fig 8 (b) and 9 (b), it has been observed same peaks at slight positions happened by the same group. In Fig 8 (c), the peaks are at 6.9°, 9.3°, 21.53° and 22.01°observed with semi region of amorphous characteristic. In Fig 9 (c) 8.1°, 9.8°, 22.05° and 22.45° determined. It is clearly stated that, the shell is encapsulated around different mixtures with altered position and new peak is not revealed in Fig 8 (c) and 9 (c). The modest shift in locations is due to changes in core and shell composition

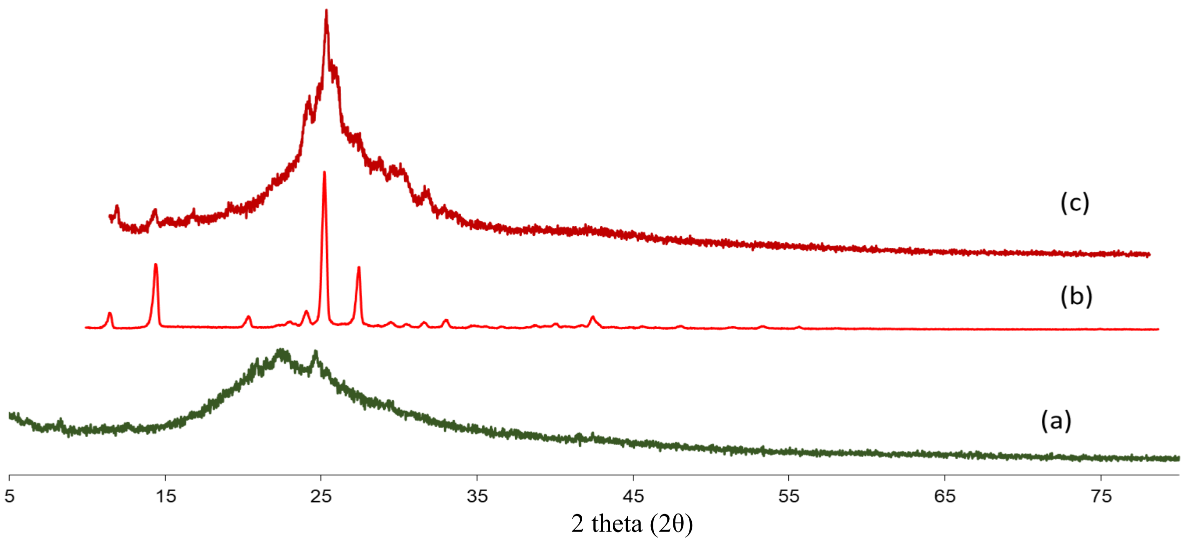

Fig. 8. XRD analysis (a) MF (b) 75% SA+25% CA (c) MPCM.

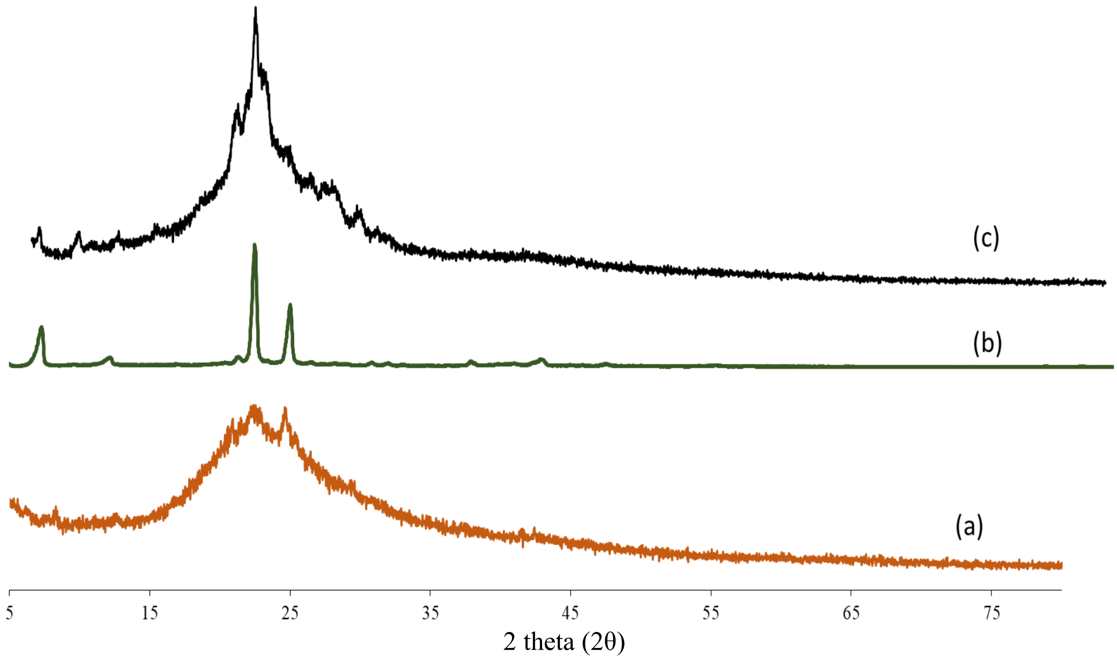

Fig. 9. XRD analysis (a) MF (b) 63% SA + 37% CA (c) MPCM.

4.4 Thermogravimetric analysis of microencapsulated eutectic mixtures

The weight loss of microencapsulated eutectic mixtures and their phase transitions were shown in Fig 10 and 11. In TGA analysis, two distinguish percentage weight losses are observed as temperature increased from 50 °C to 500 °C. From temperature 50 °C to 100 °C minor weight loss owing to moisture content over surface of the microcapsules. The primary percentage weight losses are 69% and 67% occurred in the temperature range 155 °C to 248 °C and 152 °C to 237 °C corresponding to microencapsulation of 75% SA + 25% CA and 63% CA + 37% PA due to evaporation of different composition of eutectic mixtures. The secondary weight losses are 19.4% and 23.3% due to decomposition of shell material contained in MPCMs in the temperature range of 270 °C to 450 °C Fig 10 (a) and (b). Thermal stability of phase transition of different eutectic mixtures is 202.5 °C [24] and 201 °C [25] corresponding to 75% SA + 25% CA and 63% CA+37% PA respectively. The thermal stability of microencapsulation of 75% SA + 25% CA increased from 202.5 °C to 241°C as shown Fig 11 (a) and 63% CA+37% PA from 201 °C to 228 °C Fig 11(b). Residue loss accounts for the remaining minor weight losses. When compared to microcapsules with 63 % CA+37 % PA, microcapsules with 75 % SA+25 % CA have a higher percentage weight loss. This indicates that the core content in the shell is more occupied due to encapsulation efficiency and density of eutectic mixtures. The varying thermal stability of microencapsulation of eutectic mixtures are based on their compositions between core and shell.

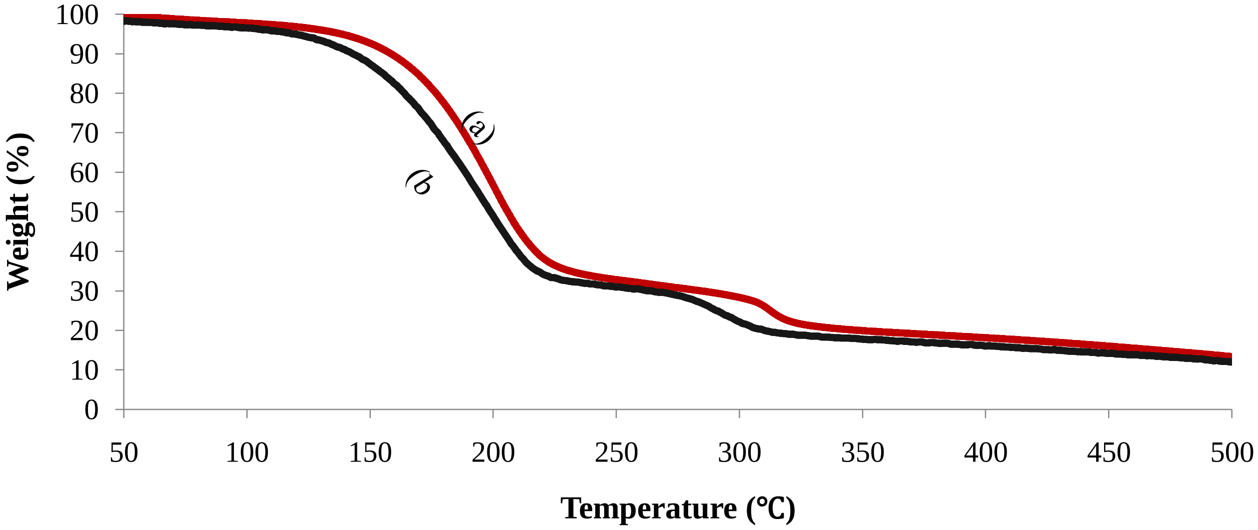

Fig. 10.TGA analysis of MPCM (a) 75% SA + 25% CA (b) 63% CA + 37% PA.

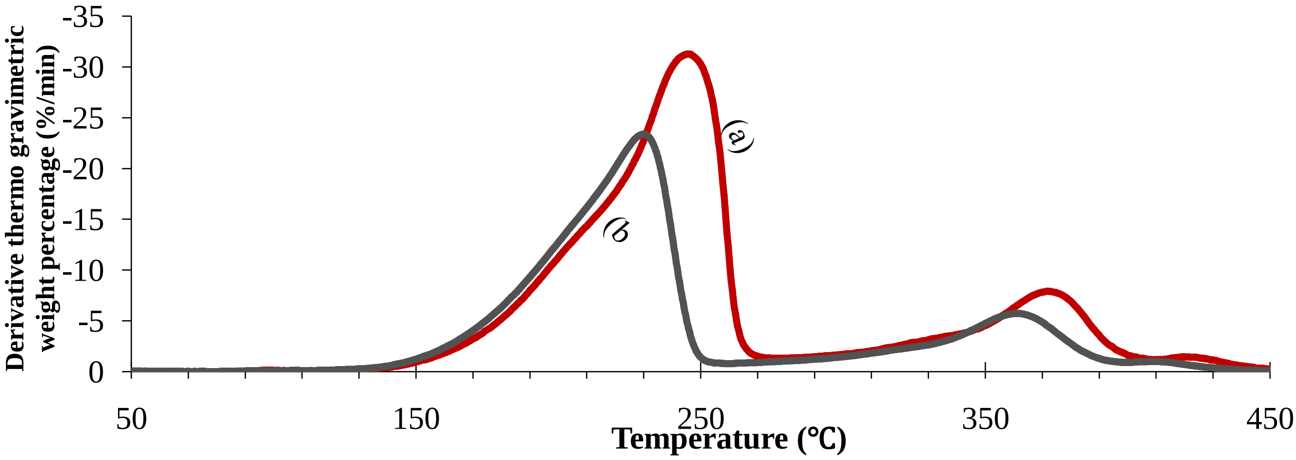

Fig. 11.DTG analysis of MPCM (a) 75% SA+25% CA (b) 63% CA+37% PA.

4.5 DSC analysis of microencapsulated eutectic mixtures

Energy can be storage in two ways such as sensible heat storage and latent heat storage. The latent heat of fusion has been carried out by using DSC instrument. The heating and cooling curve of microencapsulation of 75% SA+25% CA and 63% CA+37% PA shown in Fig 12 and 13. The melting point and latent heat of fusion of 75% SA + 25% CA and 63% CA + 37% PA are 35 $^{\circ}$C 121.8 kJ/kg [24] and 36.2 $^{\circ}$C and 134.75 kJ/kg [25] respectively. The tangent lines were drawn to left of the curves and determined area under curve refers to latent heat of fusion. The thermal properties of different microcapsules are 34.9 $^{\circ}$C, 95.3 kJ/kg and 35.6 $^{\circ}$C, 98.5 kJ/kg resultant to microencapsulation of 75% SA+ 25% CA and 63% CA + 37% PA respectively Fig 12 (a) and (b) and 13 (a) and (b). The latent heat of fusion of microcapsules of 63% CA + 37% PA is more as compared to microcapsules of 75% SA+ 25% CA. The difference in latent heat of fusion is owing to energy density of 63% CA + 37% PA is high. The core content in the shells were 78.2% and 73.09 %. The obtained results revealed that, the different microcapsules have the potential to incorporate in different applications such solar energy system and building components such as mortar, gypsum, concrete and bricks etc.

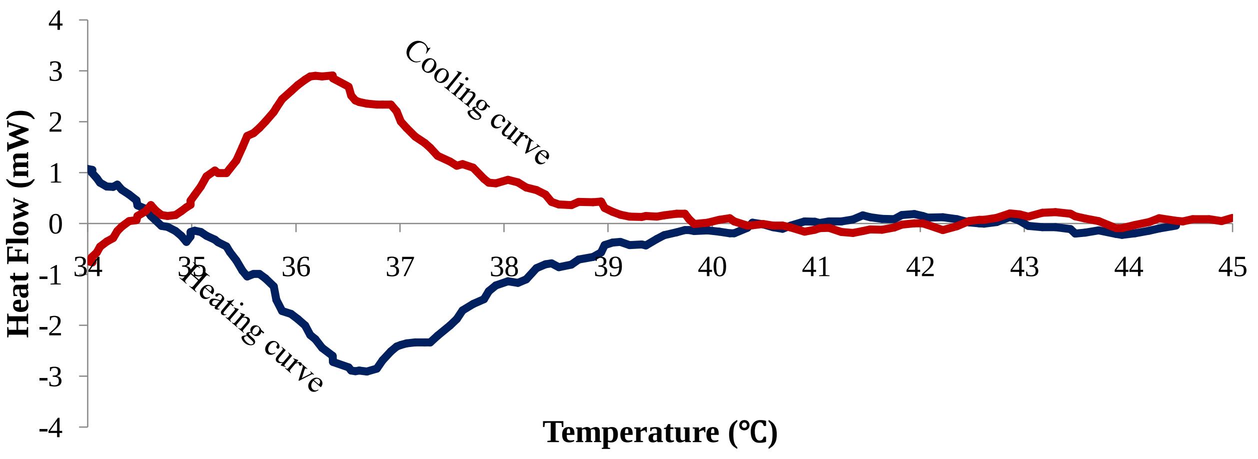

Fig. 12. DSC heating and cooling curve of MPCM of 75% SA + 25% CA.

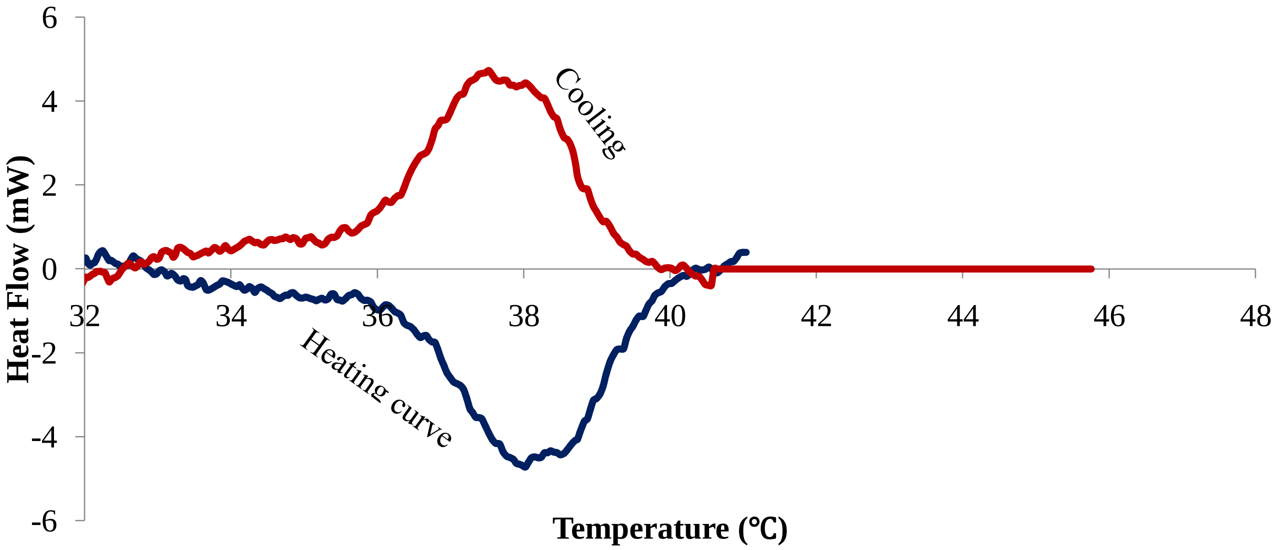

Fig. 13.DSC heating and cooling curve of MPCM of 63% CA + 37% PA.

4.6 Charging and discharging of microencapsulated eutectic mixtures

The charging and discharging of microcapsules of 75% SA+ 25% CA has been discussed in detail in our previous study[24]. The experimental setup of microcapsules of 63% CA + 37% PA was presented in Fig 14 and the obtained results are in Fig 15 (a) and(b) and Fig. 16(a) and (b). Both the eutectic mixture and the microcapsule were initiated at 33 °C. The heat is fastened on account of sensible heat from 33 °C to 35.4 °C for 150 seconds. The temperature curves of the eutectic mixture and microcapsule were flat from 150 to 210 seconds at 35.4 °C. It indicates that the material melts and the heat is concentrated by latent heat of fusion for up to 210 seconds, when the material is entirely liquid Fig 15 (a) and (b). Figure 16 (a) and (b) illustrates the eutectic mixture and microcapsule discharge curves (b). The temperature drops suddenly from 41.4 °C to 35.1 °C, and the sensible heat is quickly released into the environment within 120 seconds. The heat is gently released to the atmosphere starting at 35.1 °C and continues until the substance solidifies entirely after 420 seconds. The charging and discharging of material are found to be dependent on the core content in the shell, the thermal conductivity of the shell, and the rate of heat transmission as a result of the findings.

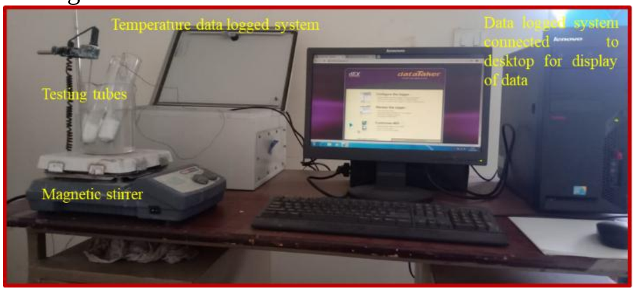

Fig. 14. Experimental set up for charging and discharging curve

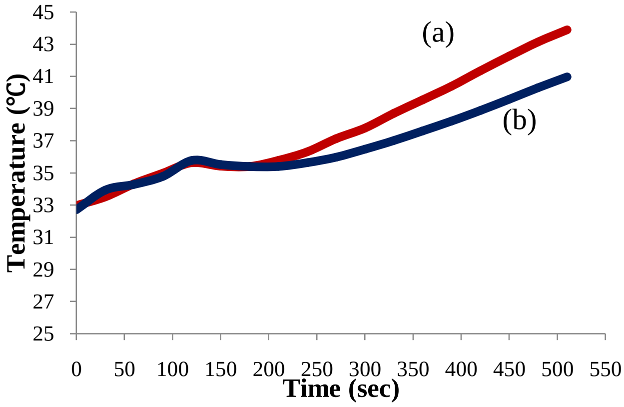

Fig. 15. Charging curve of (a) 63% CA + 37% PA (b) MPCM

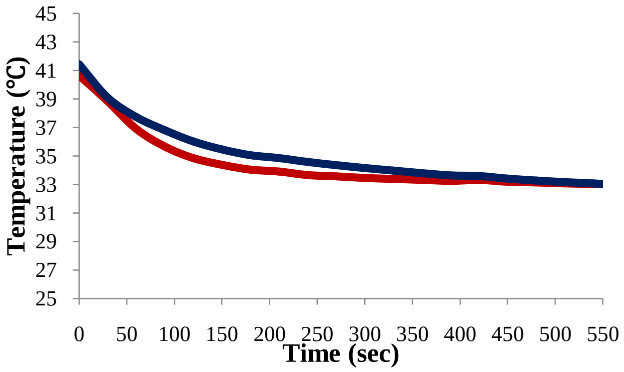

Fig. 16. Discharging curve of (a) 63% CA + 37% PA (b) MPCM

4.7 Percentage yield of the different microcapsules

The characterization of different microcapsules demonstrated that a pre-pilot scale development of in-situ polymerization process can produce around 1kg of product per day. It will be beneficial to incorporate into several domains such as building energy conversation, solar heating, paints, textiles, and food processing industries, as well as preparing various fatty acids such as LA, SA, CA, and Paraffin, among others. The resulting different products were cleaned with ethanol to remove any unformed microcapsules and dried before being weighed to determine the yield percentage. The yield of the product has been determined according to the following equation

$$\%Yield = \frac{M_1 - M_2}{M_1} \times 100 \quad (8)$$

M_1 is amount of raw materials (g), M_2 is the amount of different microcapsules (g).

Table 4 Determination of yield of microcapsules

S. No	PCM	Amount raw materials (M1) (g)	Formation of MPCM (M2) (g)	%Yield
1	75% SA+25% CA	860	710	82.5
2	63% CA+37% PA	1059	870	81.6

The amount of individual raw materials and dosage of microcapsules were provided in table 4. The percentage yield of the products is obtained approx. 82%.According to Vogel and Furniss [26] different norms are categorized as follows quantitative yields are those that are close to 100 percent, excellent yields are those that are above 90%, very good yields are those that are above 80 %, good yields are those that are above 70%, fair yields are those that are above 50%, and poor yields are those that are below 40%. As per author, the obtained yield is falls under in very good achievement for pre-pilot scale preparation of various microcapsules. The obtained results compared with available literature as shown in table 5.

5. CONCLUSION

The microencapsulation of 75% SA + 25% CA and 63% CA + 37% PA successfully synthesized with designed and development of in-situ polymerization technique from lab scale to pre-pilot scale. The microcapsules are regular shaped, smooth and well encapsulated around eutectic mixtures. The mean particle size was about 3.6–6 µm and 2.5–4 µm corresponding to encapsulation of 75% SA + 25% CA and 63% CA + 37% PA respectively. The XRD and FTIR analysis of different microencapsulation revealed that, there is no interaction between the core and shell during preparation of microencapsulated eutectic mixtures. The thermal stability of different microencapsulation increased from 202.5 to 241 °C and 201 to 228 °C corresponding to distinguish microcapsules. The thermal properties of different microcapsules are 34.9 °C, 95.3 kJ/kg and 35.6 °C, 98.5 kJ/kg resultant to microencapsulation of 75% SA+ 25% CA and 63% CA + 37% PA respectively. The encapsulation of efficiencies was 78.2% and 73.09 %. The time taken to charging and discharging of microcapsules of 63% CA + 37% PA were 210 sec and 420 sec respectively. The generated products will be applied to evaluate thermal efficiency, energy demand reduction, and thermal characteristics such as specific heat and thermal conductivity in cementitious materials such as mortar, cement less concrete (i.e. gypsum), hollow bricks, and concrete.

Table 5 Lab scale preparation of different fatty acids.

S.No.	PCM	Amount (g)	Polymer	L.F (kJ/kg)	M.P (°C)	E.E(%)	Ref.
1.	Butyl stearate	25	MF	----	70	52.00	[27]
2.	Styrene maleic anhydride	10	MF	225	24	------	[28]
3.	n -dodecane	25	MF	125.2	26	90.00	[29]
4.	Hexadecane	120	MF	---	----	----	[10]
5.	Pentadecane	----	MUF	88.2	8.73	48.00	[30]
6.	n-Octadecane	15	MF	17.9	-----	71.20	[31]
7.	paraffin		MUF	134.3		77.10	[32]
8.	n-octadecane	7	PMMA	170	22.68	----	[33]
9.	Caprylic acid	15.31	PS	1.77–79.21	15–17	49.90	[13]
10.	Paraffin	---	PS	72.52	61	42.00	[34]
11.	LA	----	PS	167.26	43.77	91.64	[35]
12.	n-hexadecane	25	Poly (butyl acry-late	65.67	17	---	[36]
13.	LA	12	MF	84.96	45	---	[5]
14.	PA + CA	10	PS	46.3 and 77.3	13.5 and 17.1	---	[11]
15.	n-octadecane	20	MF	240	28	87.30	[37]
16.	Paraffin	----	UF	75.9	65	41.60	[38]
17.	n-tetradecane	10	polystyrene-silica	83.38	2.13	17.50	[39]
18.	Na_2HPO_4·7H2O	-----	SiO_2	159.8	50.1	82.41	[40]
19.	Paraffin	10-20	SiO_2	107.05	58.3	87.00	[41]
20.	n-Dodecanol	----	SiO_2	244	21	----	[42]
21.	63% CA + 37% PA	100	MF	167.26	43.77	----	[25]
22.	Paraffin	2	SiO_2	45	56.6	31.70	[43]
23.	n-octadecane	20	SiO_2	109.5	---	51.50	[44]
24.	Sodium phosphate dodecahydrate	20	SiO_2	177.0		75.3	[45]
25.	75% SA + 25% CA	20	MF	103.9	34.5	85	[24]
26.	Octadecane	15	SiO_2	227.66	28	---	[46]
27.	Na_2SO_4	1-10	SiO_2	170.60	885	----	[47]
28.	LA		SiO_2	93.80	41.5	44	[48]
29.	SA		SiO_2	46.00	71	23	[49]
30.	Paraffin		SiO_2	111.00	26.1	64	[50]
31.	75% SA + 25% CA	870	MF	95.3	34.9	78.2	Present study
32.	63% CA + 37% PA	710	MF	98.5	35.6	73.1	Present study

Acknowledgment
The authors are thankful to the Director, CSIR- CBRI for providing infrastructural facilities. The authors also acknowledge the financial support received from the Department of Science and Technology and Indo-US science and technology forum, Govt. of India through the project no.: GAP-0806 and GAP-0311

Conflict of interest
The authors report no conflict of interest.

REFERENCES

[1] Y. E. Milian, A. Gutierrez, M. Grageda, and S. Ushak, **2017**, A review on encapsulation techniques for inorganic phase change materials and the influence on their thermophysical properties. Renewable and Sustainable Energy Reviews, 73, 983-999.
[2] G. Alva, Y. Lin, L. Liu, and G. Fang, **2017**, Synthesis, characterization and applications of microencapsulated phase change materials in thermal energy storage: A review. Energy and Buildings, 144, 276-294.
[3] H. Akeiber, P. Nejat, M. Z. A. Majid, M. A. Wahid, F. Jomehzadeh, I. Z. Famileh, J. K. Calautit, B. R. Hughes, and S. A. Zaki, **2016**, A review on phase change material (PCM) for sustainable passive cooling in building envelopes. Renewable and Sustainable Energy Reviews, 60, 1470-1497.
[4] S. A. Mohamed, F. A. Al-Sulaiman, N. I. Ibrahim, M. H. Zahir, A. Al-Ahmed, R. Saidur, B. S. Yılbaş, and A. Z. Sahin, **2017**, A review on current status and challenges of inorganic phase change materials for thermal energy storage systems. Renewable and Sustainable Energy Reviews, 70, 1072-1089.
[5] Y.-H. Bao, W. Pan, T.-W. Wang, Z. Wang, F.-M. Wei, and F. Xiao, **2011**, Microencapsulation of fatty acid as phase change material for latent heat storage. Journal of Energy Engineering, 137,(4), 214-219.
[6] L. Shilei, Z. Neng, and F. Guohui, **2006**, Eutectic mixtures of capric acid and lauric acid applied in building wallboards for heat energy storage. Energy and Buildings, 38,(6), 708-711.
[7] M. M. Farid, A. M. Khudhair, S. a. K. Razack, and S. Al-Hallaj, **2004**, A review on phase change energy storage: materials and applications. Energy conversion and management, 45,(9-10), 1597-1615.
[8] X. Huang, C. Zhu, Y. Lin, and G. Fang, **2019**, Thermal properties and applications of microencapsulated PCM for thermal energy storage: A review. Applied Thermal Engineering, 147, 841-855.
[9] J. Giro-Paloma, M. Martínez, L. F. Cabeza, and A. I. Fernández, **2016**, Types, methods, techniques, and applications for microencapsulated phase change materials (MPCM): a review. Renewable and Sustainable Energy Reviews, 53, 1059-1075.
[10] F. Khakzad, Z. Alinejad, A. R. Shirin-Abadi, M. Ghasemi, and A. R. Mahdavian, **2014**, Optimization of parameters in preparation of PCM microcapsules based on melamine formaldehyde through dispersion polymerization. Colloid and polymer science, 292,(2), 355-368.
[11] D. K. Döğüşcü, A. Altıntaş, A. Sarı, and C. Alkan, **2017**, Polystyrene microcapsules with palmitic-capric acid eutectic mixture as building thermal energy storage materials. Energy and Buildings, 150, 376-382.
[12] D. K. Döğüşcü, Ç. Kızıl, A. Bicer, A. Sarı, and C. Alkan, **2018**, Microencapsulated n-alkane eutectics in polystyrene for solar thermal applications. Solar Energy, 160, 32-42.
[13] Y. Konuklu and H. Ö. Paksoy, **2017**, Polystyrene-based caprylic acid microencapsulation for thermal energy storage. Solar Energy Materials and Solar Cells, 159, 235-242.
[14] A. Sarı, C. Alkan, and A. N. Özcan, **2015**, Synthesis and characterization of micro/nano capsules of PMMA/capric–stearic acid eutectic mixture for low temperature-thermal energy storage in buildings. Energy and Buildings, 90, 106-113.
[15] Y. Konuklu, H. O. Paksoy, M. Unal, and S. Konuklu, **2014**, Microencapsulation of a fatty acid with Poly (melamine–urea–formaldehyde). Energy conversion and management, 80, 382-390.
[16] H. Wang, P. Gui, Y. Zhu, and S. Hu, **2020**, Preparation and Characterization of Poly (melamine-urea-fbrmaldehyde) Tetradecanol Microcapsules Coated with Silver Particles. Journal of Wuhan University of Technology-Mater. Sci. Ed., 35, 327-334.
[17] S. Han, Y. Chen, S. Lyu, Z. Chen, S. Wang, and F. Fu, **2020**, Effects of processing conditions on the properties of paraffin/melamine-urea-formaldehyde microcapsules prepared by in situ polymerization. Colloids and Surfaces A: Physicochemical and Engineering Aspects, 585, 124046.
[18] H. Zhang and X. Wang, **2009**, Fabrication and performances of microencapsulated phase change materials based on n-octadecane core and resorcinol-modified melamine–formaldehyde shell. Colloids and Surfaces A: Physicochemical and Engineering Aspects, 332,(2-3), 129-138.
[19] L. Yang, X. Cao, N. Zhang, B. Xiang, Z. Zhang, and B. Qian, **2019**, Thermal reliability of typical fatty acids as phase change materials based on 10,000 accelerated thermal cycles. Sustainable Cities and Society, 46, 101380.
[20] V. Chinnasamy and S. Appukuttan, **2019**, Preparation and thermal properties of lauric acid/myristyl alcohol as a novel binary eutectic phase change material for indoor thermal comfort. Energy Storage, 1,(5), e80.
[21] J. Zuo, W. Li, and L. Weng, **2011**, Thermal properties of lauric acid/1-tetradecanol binary system for energy storage. Applied thermal engineering, 31,(6-7), 1352-1355.
[22] N. Zhang, Y. Yuan, X. Wang, X. Cao, X. Yang, and S. Hu, **2013**, Preparation and characterization of lauric–myristic–palmitic acid ternary eutectic mixtures/expanded graphite composite phase change material for thermal energy storage. Chemical Engineering Journal, 231, 214-219.
[23] W. L. Mccabe, J. C. Smith, and P. Harriott, Unit operations of chemical engineering. Vol. 5. McGraw-hill New York, 1993.
[24] B. Srinivasaraonaik, L. P. Singh, I. Tyagi, A. Rawat, and S. Sinha, **2020**, Microencapsulation of a eutectic PCM using in situ polymerization technique for thermal energy storage. International Journal of Energy Research, 44,(5), 3854-3864.
[25] B. Srinivasaraonaik, L. P. Singh, S. Sinha, I. Tyagi, and A. Rawat, **2020**, Studies on the mechanical

properties and thermal behavior of microencapsulated eutectic mixture in gypsum composite board for thermal regulation in the buildings. Journal of Building Engineering, 31, 101400.

[26] A. I. Vogel; and B. S. Furniss, Vogel's Textbook of Practical Organic Chemistry. Prentice Hall, 1996.

[27] B. Alič, U. Šebenik, and M. Krajnc, **2012**, Microencapsulation of butyl stearate with melamineformaldehyde resin: Effect of decreasing the pH value on the composition and thermal stability of microcapsules. Express polymer letters, 6,(10), 826–836.

[28] J. Su, L. Wang, and L. Ren, **2006**, Fabrication and thermal properties of microPCMs: Used melamine- formaldehyde resin as shell material. Journal of applied polymer science, 101,(3), 1522-1528.

[29] Z. Chen, J. Wang, F. Yu, Z. Zhang, and X. Gao, **2015**, Preparation and properties of graphene oxide-modified poly (melamine-formaldehyde) microcapsules containing phase change material n-dodecanol for thermal energy storage. Journal of Materials Chemistry A, 3,(21), 11624-11630.

[30] Y. Konuklu and F. Erzin, **2019**, Preparation of pentadecane/poly (melamine- urea- formaldehyde) microcapsules for thermal energy storage applications. International Journal of Energy Research, 43,(12), 6322-6326.

[31] X. Wang and T. Zhao, **2016**, Effects of parameters of the shell formation process on the performance of microencapsulated phase change materials based on melamine-formaldehyde. Textile Research Journal, 87,(15), 1848-1859.

[32] X. Wang, C. Li, and T. Zhao, **2018**, Fabrication and characterization of poly(melamine-formaldehyde)/silicon carbide hybrid microencapsulated phase change materials with enhanced thermal conductivity and light-heat performance. Solar Energy Materials and Solar Cells, 183, 82-91.

[33] W. Su, T. Zhou, Y. Li, and Y. Lv, **2019**, Development of microencapsulated phase change material with poly (methyl methacrylate) shell for thermal energy storage. Energy Procedia, 158, 4483-4488.

[34] Y. Shao, H. Jiang, S. Li, J. Yang, M. Zhang, and J. Li, **2018**, Preparation of microencapsulated phase change materials based on expanded polystyrene foam wastes. Micro & Nano Letters, 13,(7), 998-1000.

[35] S. Sami, S. M. Sadrameli, and N. Etesami, **2018**, Thermal properties optimization of microencapsulated a renewable and non-toxic phase change material with a polystyrene shell for thermal energy storage systems. Applied Thermal Engineering, 130, 1416-1424.

[36] S. Alay, F. Göde, and C. Alkan, **2011**, Synthesis and thermal properties of poly (n- butyl acrylate)/n- hexadecane microcapsules using different cross- linkers and their application to textile fabrics. Journal of Applied Polymer Science, 120,(5), 2821-2829.

[37] M. Palanikkumaran, K. K. Gupta, A. K. Agrawal, and M. Jassal, **2010**, Effect of emulsion preparation method on microencapsulation of n-octadecane using melamine-formaldehyde pre-polymers.

[38] L. Sánchez-Silva, V. Lopez, N. Cuenca, and J. L. Valverde, **2018**, Poly (urea-formaldehyde) microcapsules containing commercial paraffin: in situ polymerization study. Colloid and Polymer Science, 296,(9), 1449-1457.

[39] W. Fu, X. Liang, H. Xie, S. Wang, X. Gao, Z. Zhang, and Y. Fang, **2017**, Thermophysical properties of n-tetradecane@ polystyrene-silica composite nanoencapsulated phase change material slurry for cold energy storage. Energy and Buildings, 136, 26-32.

[40] Y. Fang, L. Huang, X. Liang, S. Wang, H. Wei, X. Gao, and Z. Zhang, **2020**, Facilitated synthesis and thermal performances of novel SiO_2 coating Na_2HPO_4· $7H_2O$ microcapsule as phase change material for thermal energy storage. Solar Energy Materials and Solar Cells, 206, 110257.

[41] G. Fang, Z. Chen, and H. Li, **2010**, Synthesis and properties of microencapsulated paraffin composites with SiO_2 shell as thermal energy storage materials. Chemical engineering journal, 163,(1-2), 154-159.

[42] L. Geng, S. Wang, T. Wang, and R. Luo, **2016**, Facile synthesis and thermal properties of nanoencapsulated n-dodecanol with SiO_2 shell as shape-formed thermal energy storage material. Energy & Fuels, 30,(7), 6153-6160.

[43] B. Li, T. Liu, L. Hu, Y. Wang, and L. Gao, **2013**, Fabrication and properties of microencapsulated paraffin@ SiO_2 phase change composite for thermal energy storage. ACS Sustainable Chemistry & Engineering, 1,(3), 374-380.

[44] S. Liang, Q. Li, Y. Zhu, K. Chen, C. Tian, J. Wang, and R. Bai, **2015**, Nanoencapsulation of n-octadecane phase change material with silica shell through interfacial hydrolysis and polycondensation in miniemulsion. Energy, 93, 1684-1692.

[45] Z. Liu, Z. Chen, and F. Yu, **2019**, Preparation and characterization of microencapsulated phase change materials containing inorganic hydrated salt with silica shell for thermal energy storage. Solar Energy Materials and Solar Cells, 200, 110004.

[46] F. Tang, L. Liu, G. Alva, Y. Jia, and G. Fang, **2017**, Synthesis and properties of microencapsulated octadecane with silica shell as shape–stabilized thermal energy storage materials. Solar Energy Materials and Solar Cells, 160, 1-6.

[47] X. Wu, M. Fan, S. Cui, G. Tan, and X. Shen, **2018**, Novel Na_2SO_4@ SiO_2 phase change material with core-shell structures for high temperature thermal storage. Solar Energy Materials and Solar Cells, 178, 280-288.

[48] Y. Zhang, J. Zhang, X. Li, and X. Wu, **2019**, Preparation of hydrophobic lauric acid/SiO_2 shape-stabilized phase change materials for thermal energy storage. Journal of Energy Storage, 21, 611-617.

[49] N. Şahan and H. Paksoy, **2017**, Determining influences of SiO_2 encapsulation on thermal energy storage properties of different phase change materials. Solar Energy Materials and Solar Cells, 159, 1-7.

[50] R. Luo, S. Wang, T. Wang, C. Zhu, T. Nomura, and T. Akiyama, **2015**, Fabrication of paraffin@ SiO_2 shape-stabilized composite phase change material via chemical precipitation method for building energy conservation. Energy and Buildings, 108, 373-380.

Research Article

Energy, Environment and Storage x (2022) 02-02:54-63

Energy, Environment and Storage

JournalHomepage: www.enenstrg.com

Experimental and Numerical Analysis of Savonius Wind Turbine with End Plate on Various Types

MahmutBurak Akkus[1*], Zeki Haksever[1], Suleyman Teksin[1,2]

[1*]*ErciyesUniversity, Faculty of Engineering, Department of Mechanical Engineering, Kayseri, Turkey*

[1*] *mbakkus54@gmail.com, ORCID:0000-0002-4561-7093*

[1]*Erciyes University, Faculty of Engineering, Department of Mechanical Engineering, Kayseri, Turkey*

[1]*zhaksever@gmail.com, ORCID: 0000-0001-7037-4540*

[1,2]*Van YuzuncuYil University, Faculty of Engineering, Department of Mechanical Engineering, Van, Turkey*

[1,2]*steksin@yyu.edu.tr, steksin@erciyes.edu.tr, ORCID:0000-0001-8854-0332*

ABSTRACT. This study aims to observe whether the overall yield has changed utilizing the different blade structures and the end plates placed on the different blade structures of the Savonius-type wind turbine. End plates of different diameters are placed at the top and bottom of the turbine to increase overall efficiency.While the experimental analysis was conducted in the aerodynamic laboratory of the faculty of Aeronautical and Astronauticalat Erciyes University, Ansys Fluent software is used for numerical calculations.The turbine structure used for the numerical study is made according to the optimum values taken from the experimental investigationto minimize the time wasted. The results in the experimental and numerical analysis were compared with each other and the overall yield was observed to increase according to these analysis results. The presence of the end plate significantly increased the efficiency of the savonius turbine and allowed it to operate in the higher *TSR* range.This increase is directly proportional to the enlarging in the diameter of the end plate.

Keywords:Efficiency, Turbine, VAWT, Savonius, Numerical-Experimental Analysis

Article History: Received: 02.03.2022; Revised: 04.03.2022; Accepted: 27.04.2022; Available online: 24.05.2022

Doi: https://doi.org/10.52924/IUJX7477

1. INTRODUCTION

Although fossil fuels are mostly used in energy production in today's energy systems, energy production models are gradually moving to renewable energy. An important reason for this is the increase in prices of fossil resources recently [1]. Especially in the last decade, it became possible to increase the sustainability of energy production systems using the benefits of the newest technologies. For instance, methods of wind power energy systems have become more popular due to being environment-friendly and developing technologies. Furthermore, wind power energy systems generate electrical power through wind turbines. While more electricity can be produced especially from other renewable energy sources. There is no carbon emission in electricity production in wind energy [2]. Even though wind turbines might differ in terms of structure, size, and number of blades, they function in the same manner. The main functionality of wind turbines is to use the airflow within their body as much as possible to convert it into electrical energy. Although the efficiency of horizontal axis wind turbines is generally higher, vertical axis wind turbines are also widely used due to high installation and maintenance costs, high noise [3],and less wear of the parts in the system. In addition, taking the wind coming on the turbine from all directions is another important advantage and it is independent of the wind direction. Their ability to self-starting at low wind speeds is high [4]. Savonius wind turbines, whose general appearance resembles the letter S, is one of these vertical axis turbine structures.

An increasing number of studies about general structure or optimization are being conducted on wind turbines. Lots of variations affect the performance of the Savonius wind turbine such as blade shape, number of blades, gap ratio, overlap ratio, end plate, etc. [5,6]. Moreover, the wind velocity is also important for increasing the Savonius turbine performance[7].

The overlap ratio is the ratio between the distance of overlap to the turbine diameter. It also decreased the

*Corresponding author: mbakkus54@gmail.com

negative drag [8]. Fujisawa [9] determined the bucket overlap around 15%. Gupta et al. [10] have investigated both the three-bucket Darrieus and Savonius-Darrieus rotor. They found that the combination showed better performance. Simsek et al. [11] studied the different models of Savonius turbine. They used 12 models with 3 different structures by changing the number of blades. According to their study, 3 bladed modified turbine has better performance. Lee and Lim [12] investigated the performance characteristics of helical Savonius. They determined the maximum power coefficient at an angle of 45°. When this angle was set to 90° and 135°, start to decrease for Cp.

Low aspect ratios are used in designing Savonius rotors to avoid the structural failure problem of rotors due to high aspect ratios [13]. Ushiyama and Nagai[14] recommended the optimum design parameter for the rotor with a straight bucket. Placing circular flat plates on the blade tips of Savonius turbines due to tip losses is positive in terms of performance. There are many studies on endplate in the literature. Looking at these studies, usage of endplate showed an increase in the coefficient of performance [15,16]. Mohamed et al. [17] defined the stator optimum point of a conventional plate.

This paper aims to increase the efficiency of Savonius wind turbine energy systems therefore the theoretical interpretations about efficiency are examined in detail. After designing model in CAD program (Solidworks), a 3D printer was also used to produce, and numerical analyzes were carried out using the Ansys Fluent program. Numerical analysis of pressure and velocity contours of Savonius wind turbines was presented in the results and discussion section. The coefficient of performance or also called as C_P ratio is obtained by the division of airflow power in turbines over the mechanical power generated by airflow. Moreover, the TSR (tip speed ratio) value which is the ratio of the linear speed of the turbine caused by its angular speed to the linear airflow speed was calculated by experiment results. Furthermore, the x-y graph of TSR vs C_P shows that as TSR increases C_P also increases exponentially at first. Then, it reaches an optimum value and after that peak point, it starts to decrease exponentially. The peak point of this graph which is called as optimum value is the maximum efficiency point of the system.

2. MATERIALS AND METHODS

The main objective was to find a way to increase the torque in the general formula of mechanical power. The efficiency can be controlled by changing the airflow. However, the airflow speed was determined as a constant value in the experiment. Therefore, the relationship between torque and mechanical structure of turbines was examined in detail. Using constant angular speed, the change in torque was analyzed by adding different types of plates at the bottom and top of the turbine. This process was both applied numerically and experimentally. Two different types of turbine models as straight and helical were used. The relation between torque and mechanical structure of turbines was evaluated. The parameters of functions used to calculate the efficiency of the system are explained below.

Front view area,

$$\boldsymbol{A_{front\ view}} = \boldsymbol{H} * \boldsymbol{d_{rotor}} \quad (1)$$

where H is the turbine height.

Mechanical power,

$$\boldsymbol{P_{turbine}} = (\boldsymbol{T} * \boldsymbol{\omega_{turbine}}) \quad (2)$$

where $\boldsymbol{T}$ is the torque and ω is the Turbine angular velocity.

Wind power,

$$\boldsymbol{P_{wind}} = (\boldsymbol{\rho}\, \boldsymbol{A_{front\ view}} \boldsymbol{V_{wind}}^{\boldsymbol{3}}) / \boldsymbol{2} \quad (3)$$

where $\boldsymbol{\rho}$ is the density and $\boldsymbol{V_{wind}}$ is wind speed.

Tip speed ratio,

$$\boldsymbol{TSR} = (\boldsymbol{\omega_{turbine}} * (\boldsymbol{d_{rotor}}/\boldsymbol{2}) / \boldsymbol{V_{wind}}) \quad (4)$$

Coefficient of performance,

$$\boldsymbol{Cp} = (\boldsymbol{Pturbine}/\, \boldsymbol{Pwind}) \quad (5)$$

2.1 The Production of Turbines and Their Dimensions

Firstly, the turbine has 3 blades and 2 plates which were printed using a 3D printer. The infill percentage of plates is 40% and for the blades, it is 60%. Furthermore, the print bed temperature was approximately 60°C and the temperature of the nozzle was 200°C. Medium quality PLA **(**Polylactic acid) 3D printing filament was used. The dimensions of a final product were matching with desired values thus production was achieved successfully. The top view and dimensions were given of Model-1 (straight-bladed) in Figure 1.

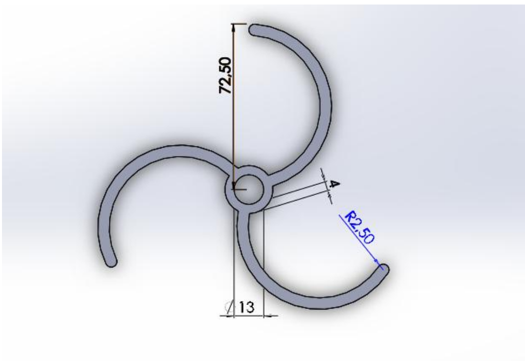

Figure 1. The Model-1 (without end plate)

Figures 3, 4, and 5 show cases where endplates are added. These plates with diameters of 5, 12, and 16 cm are indicated in figures 3, 4, and 5, respectively. The height of both models is 20 cm.

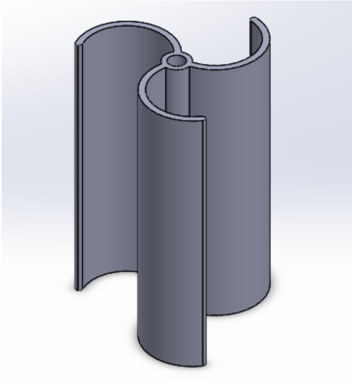

Figure 2. The Model-1 of an isometric view

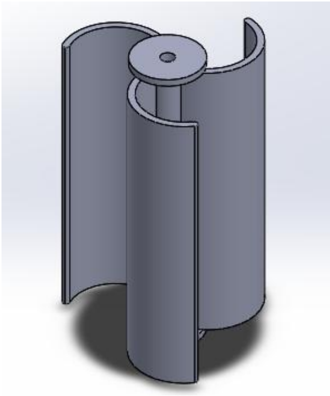

Figure 3. The Model-1 (with 5cm end plate) of an isometric view

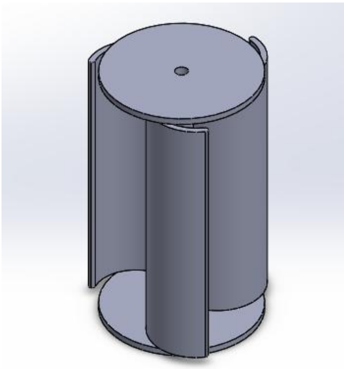

Figure 4. The Model-1 (with 12cm end plate) of an isometric view

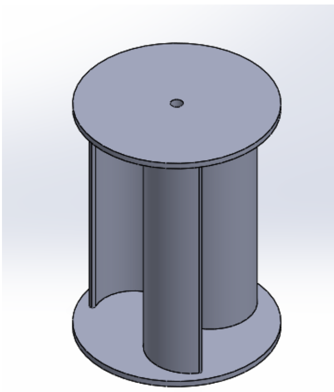

Figure 5. The Model-1 (with 16cmend plate) of an isometric view

Figure 6 indicates the general dimensions of the helical turbine. The isometric view of this turbine without an endplate can be seen in figure 7.

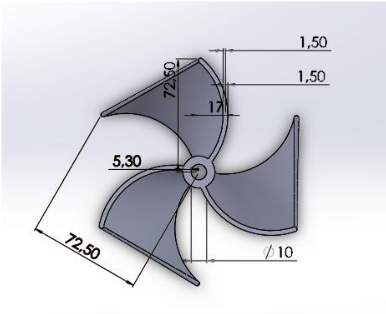

Figure 6. TheModel-2 (without end plate)

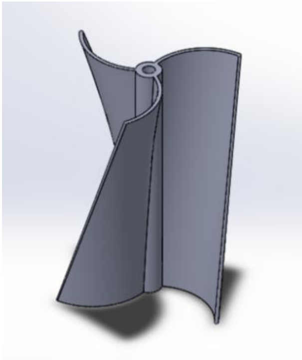

Figure 7. TheModel-2of an isometric view

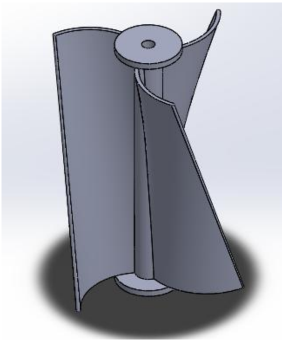

Figure 8. The Model-2 (with 5cm end plate) ofan isometric view

Figures 8,9, and 10 show the state of endplates with varying diameters.

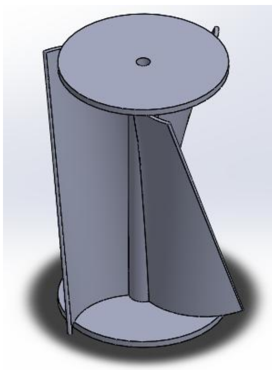

Figure 9. TheModel-2(with 12cm end plate) ofan isometric view

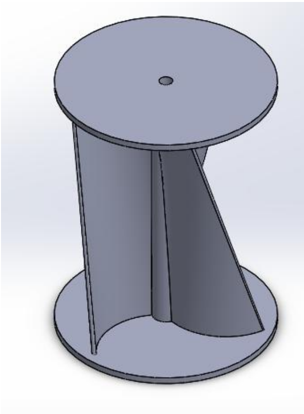

Figure 10. The Model-2(with 16 cm end plate) of an isometric view

2.2 EXPERIMENTAL ANALYSIS

The wind tunnel is used as an experimental environment (Fig. 11 and 12).The experiment place shown in figure 11 was carried out in the aerodynamics laboratory of Erciyes University, Faculty of Aeronautics and Astronautics. Savonius wind turbines consist of one main body structure formed by 3 blades. Moreover, the values of power and efficiency were compared by applying wind tunnel tests using different types and numbers of blades. Furthermore, different-sized plates depending on the nominal diameter are placed at the bottom and top of the blades. The temperature of the experiment environment was 15°C and the dynamic viscosity value was determined as 1.78×10^{-5} kg/m.s based on temperature. The value of density was chosen as 1.089 kg/m^3 considering the altitude. The velocity of the air inlet is constant at 10 m/s.

Figure 11. Photos of the wind tunnel from Aerodynamics Laboratory of Erciyes University, Faculty of Aeronautics and Astronautics

2.2.1 Experiment Procedure

In the experimental environment, turbines were placed in the test section of the wind tunnel. The wind tunnel has a 570x570 mm inlet and 590x590 mm outlet section at the test zone. Moreover, the airflow was supplied externally ith a 15 kW electrical fan to reach the required wind speed. In order to reduce experimental errors, after the turbine started to rotate, it has waited until the voltage value produced was stabilized. Furthermore, the voltage value was reduced gradually with an electronical load and the resulting angular velocity value and torque were measured by the torque meter to the turbine shaft connected with coupling. Then, the printed end plates for the blade were mounted and the same operations were repeated. The results of the experimental analyzes made in the wind tunnel are shown in figures 13 and 14. The x-axis in these graphs is TSR (Tip Speed Ratio) and the y-axis is Cp (Coefficient of Performance). The experiment was carried out with a constant wind speed of 10 m/s, and the models used were first carried out without end plates, and then by placing plates of 5 cm, 12 cm, and 16 cm in diameter, respectively.Using the parameters mentioned before and experiment results, the graphs shown in Figures 13 and 14 were obtained. TSR- CP diagram showed that the presence of the end plate affected positively. The increase in the diameter of the end plate resulted in a greater increase in the power coefficient CP, and at the same time, it operated at high TSR values. Differences between experimental and numerical results were thought to be due to printer calibration problems in the production of models manufactured from 3D printers [19]. According to the information obtained from the experiment, the following can be said: By taking the no plates condition of the models produced as a reference, it has been seen that the plates with a smaller diameter than the nominal diameter of the models do not affect increasing the efficiency (5cm and 12cm end plates). However, positive results were obtained for the plates with a diameter larger than the nominal diameter of the models (16cm end plates) to increase the overall efficiency**.**

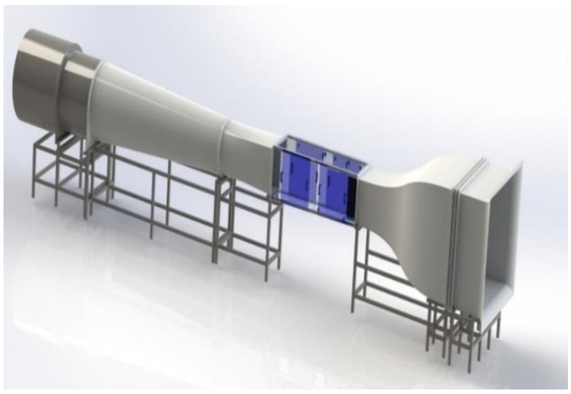

Figure 12. Themodel of the wind tunnel (adapted from [18])

Figure 14. The Model-2 of the TSR-CP diagram

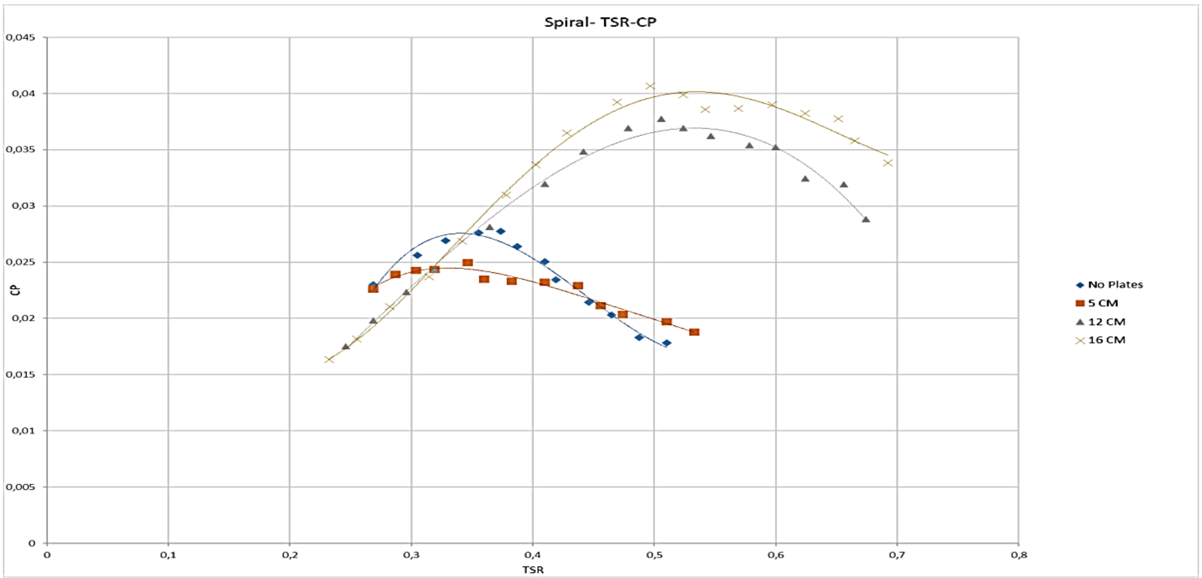

Figure 14.The Model-2 of the TSR-CP diagram

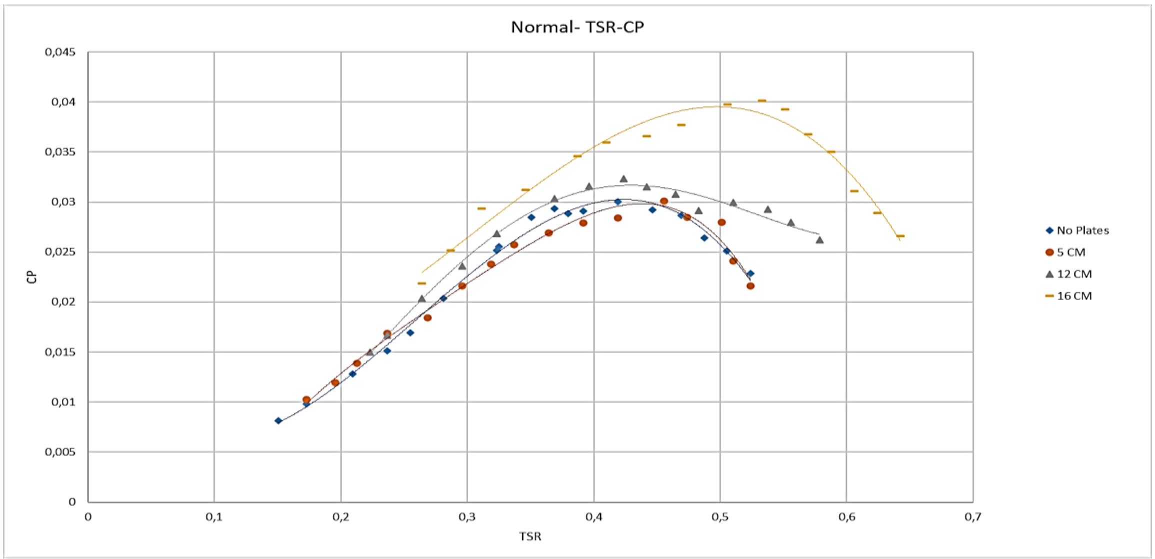

Figure 13.The Model-1 of the TSR-CP diagram

2.3 Numerical Analysis

ANSYS Fluent software was used to simulate the system and to compare experimental results with numerical analysis. The parameters used for numerical analysis are experimental analysis conditions. The turbulence model used for analytics has been selected as the SST k-ω turbulence model, seen to be good at aerodynamic and turbocharger analysis in recent academic studies [1,14,20]. The SST k-ω solving model contains both advantages of k-ε and k-u turbulencemodels[21].Coupled method and second-order differential solution in Fluent were chosen.

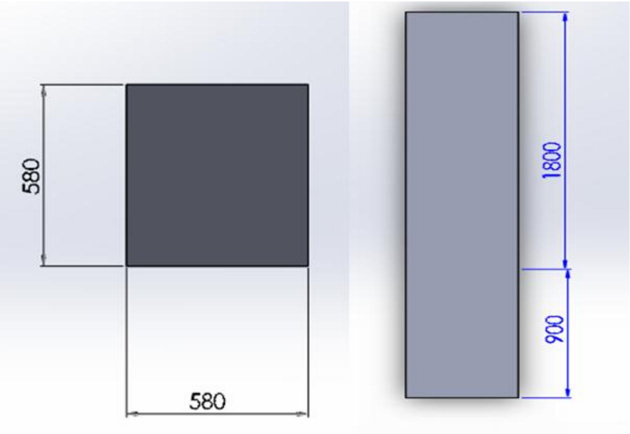

Figure 15. Size of the wind tunnel for ANSYS analysis.

In figure 15, the size of the wind tunnel was given for numerical solution. While inlet distance was 900 mm, the distance after the body was 1800 mm in length. An isometric view of the tunnel is also given in figure 16. The cylindrical shape represents the placed turbine location which was set rotary zone.

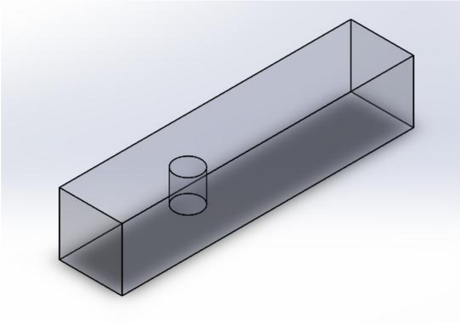

Figure 16. The wind tunnel of an isometric view

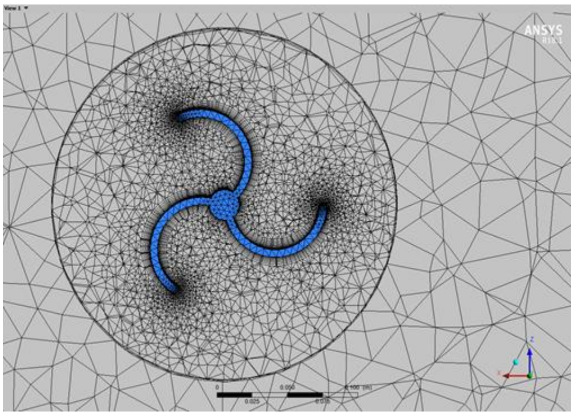

Figure 17. TheModel-1's mesh structure for ANSYS analysis

Figure 17 showed a mesh structure around the Savonius wind turbine with the sectional plane.

Table 1 The table here shows only the changed settings. Settings not mentioned are taken by default in the program.

	Normal-no plates	Normal-16 cm plates added	Spiral-no plates	Spiral- 16 cm plates added
General mesh	Fine	Fine	Fine	Fine
Method	Tetrahedron (rot,tunnel) -patch conforming	Tetrahedron (rot,tunnel) -patch conforming	Tetrahedron (rot,tunnel) -patch conforming	Tetrahedron (rot,tunnel) -patch conforming
Local mesh	Sizing (wall_kanat)- 5 mm	Sizing (wall_kanat)- 5 mm	Sizing (wall_kanat)- 5 mm	Sizing (wall_kanat)- 5 mm
Inflation	Smooth transition-10 layers	Smooth transition-10 layers	Smooth transition-10 layers	Smooth transition-5 layers
Element/node statistics	1217837/361449	1300511/408196	2137710/602844	1883500/467884

A steady solution with 2000 iterations was found independent of time. The method in figure 18 was used in each analysis solution. The primary outcome in the data obtained from the analyzes here is with determining angular velocity whether the torque changes depending on different plates placed on the turbine. If the torque changes in a positive manner, that means the TSR/C_P ratio mentioned above will increase. This clearly shows that maintaining more airflow within the blades provides more power output thus the efficiency increases. In addition, the analysis of the pressure and velocity distributions of the turbines was achieved with the help of CFD-post within the external flow. Therefore, it was possible to observe the airflow events and their impact around the turbine.

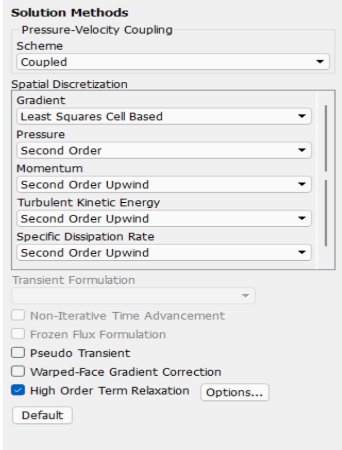

Figure 18. Solution methods

Table 2 Mesh Metric Values-Quality (Orthogonal)

Quality Values (Based On Ansys Fluent Guide)				
	Ortogonal Quality			
Name	MIN	MAX	AVG	DEVIATION
Model-1 (with no end plates)	0,11247	0,99376	0,76167	0,12237
Model-2 (with no end plates)	0,10031	0,99559	0,76156	0,11586
Model-1 (with 16 cm end plates)	0,10959	0,99561	0,75418	0,12762
Model-2 (with 16 cm end plates)	0,13315	0,99634	0,7616	0,11902

Table 3 Mesh Metric Values-Quality (Element)

Quality Values (Based On Ansys Fluent Guide)				
	Element Quality			
Name	MIN	MAX	AVG	DEVIATION
Model-1 (with no end plates)	2,0116e-002	0,99994	0,61219	0,31636
Model-2 (with no end plates)	2,1826e-002	0,99992	0,6369	0,31023
Model-1 (with 16 cm end plates)	2,2884e-002	0,99992	0,58134	0,32362
Model-2 (with 16 cm end plates)	5,5574e-002	1	0,7228	0,24058

Table 4 Mesh Metric Values-Quality (Skewness)

Quality Values (Based On Ansys Fluent Guide)				
	Skewness			
Name	MIN	MAX	AVG	DEVIATION
Model-1 (with no end plates)	1,037e-004	0,8456	0,23705	0,12256
Model-2 (with no end plates)	1,5443e-004	0,82389	0,23733	0,1165
Model-1 (with 16 cm end plates)	1,5443e-004	0,88186	0,24463	0,12787
Model-2 (with 16 cm end plates)	7,3693e-006	0,86685	0,23736	0,12045

Adequate mesh optimization could not be performed in the numerical analysis, and meshing was performed in accordance with the quality values scale found in the Ansys Fluent manual by looking at the computer capacity (tables 2, 3 and 4)[21]. The results from numerical analysis will be closer to the results of experimental analysis by using better mesh structure.

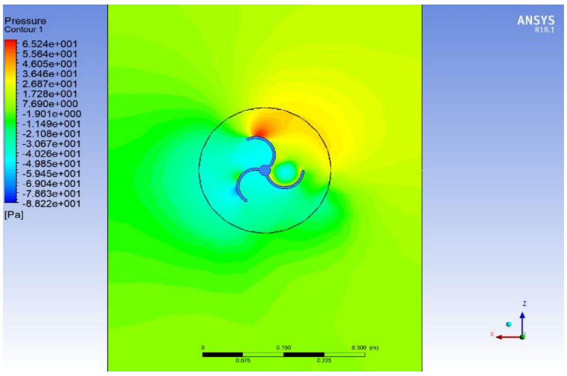

Figure 19. The Model-1's (without end plate) contour of pressure (ZX plane)

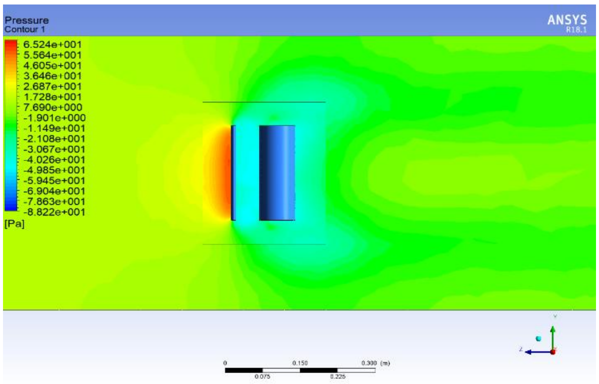

Figure 20. TheModel-1's (without end plate) contour of pressure (YZ plane)

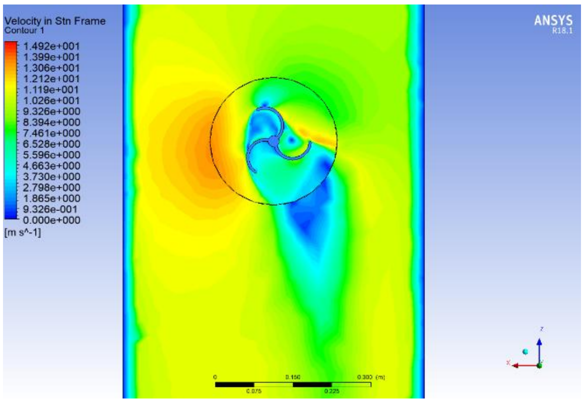

Figure 21. The Model-1's (without end plate) contour of velocity (ZX plane)

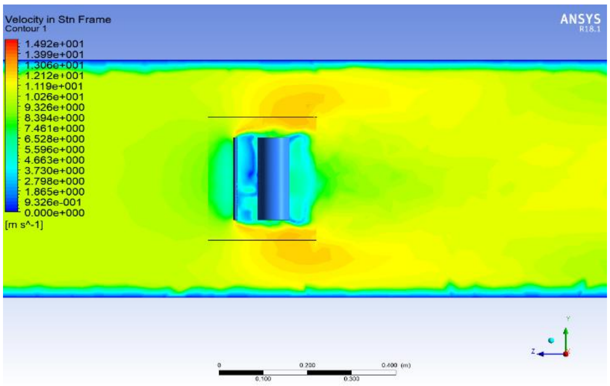

Figure 22. The Model-1's (without end plate) contour of velocity (YZ plane)

Bare cases of the turbine (without end plate) were demonstrated in figures 19-22.Figure 19 and figure 20 showed pressure contours, top/side view respectively. The other view defined the velocity contours. On the other hand, figures 23-26 show the same status with a diameter of 16 mm endplate. According to these figures, endplate narrowed the wake flow region and increased the speed of wind leaving the blades. The maximum pressure level did not change however pressured zone was minimized in front of the turbine.

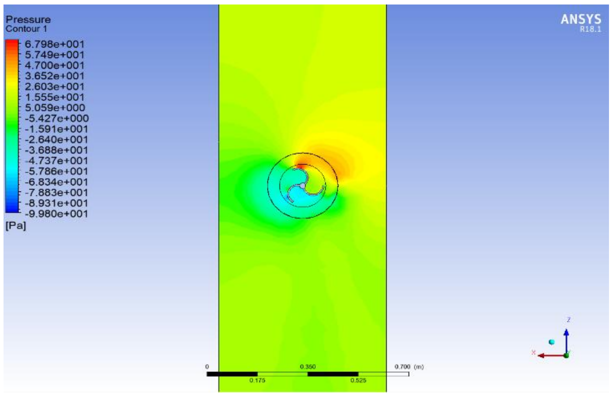

Figure 23. The Model-1's (with 16cm end plate) contour of pressure (ZX plane)

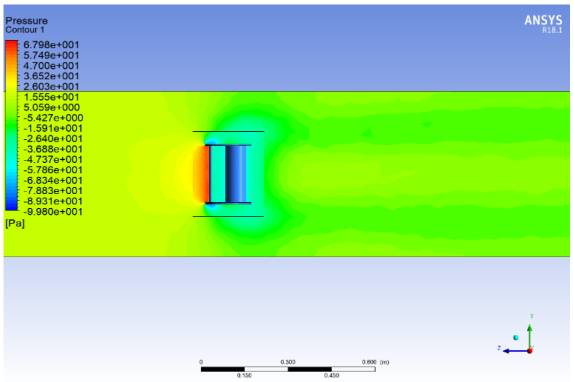

Figure 24. The Model-1's (with 16cm end plate) contour of pressure (YZ plane)

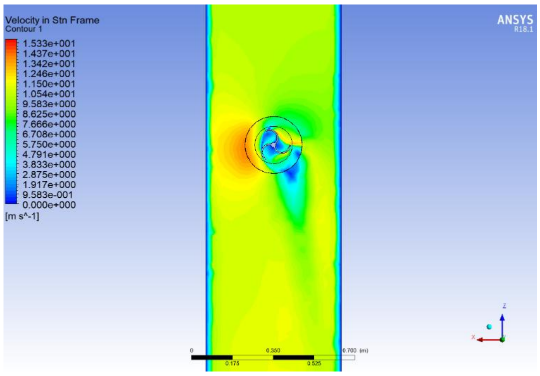

Figure 25. The Model-1's (with 16cm end plate) contour of velocity (ZX plane)

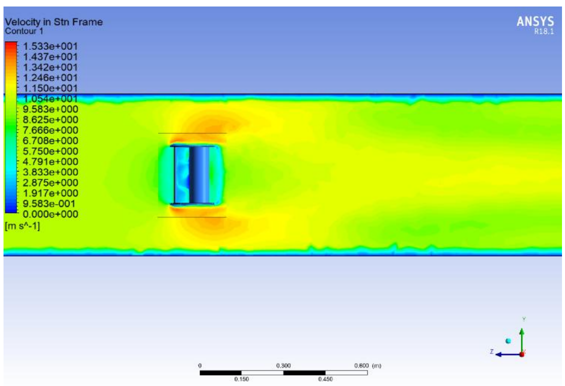

Figure 26. The Model-1's (with 16cm end plate) contour of velocity (YZ plane)

These figures (between 19-26) are the velocity and pressure contours created with the numerical analysis program (ANSYS Fluent CFD-post) using the data obtained from the experiments carried out in the wind tunnel. Here, figures 19-22 are the velocity and pressure contours of the analysis of the Model-1 without plates. In addition, figures (between 23-26) are the velocity and pressure contours of the model formed by placing plates with a diameter of 16 cm on the Model-1. Velocity images obtained from these areas were lower than the plated analysis of the Model-1 without plate (figures 21-22) compared to the plated analysis (figures 25- 26). The reason for this is that the Model-1 with the plate rotates faster because there is more air in the blade in the unit time structure. However, in the pressure contours obtained, it was observed that the Model-1, which was analyzed without a plated (figure 19-20), was less exposed to pressure.

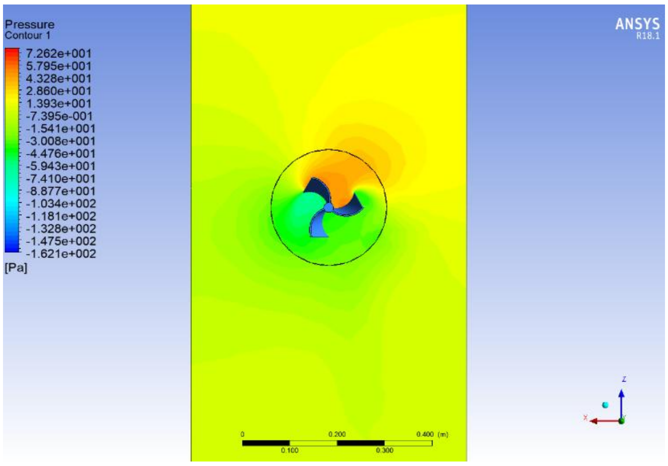

Figure 27. The Model-2's (without end plate) contour of pressure (ZX plane)

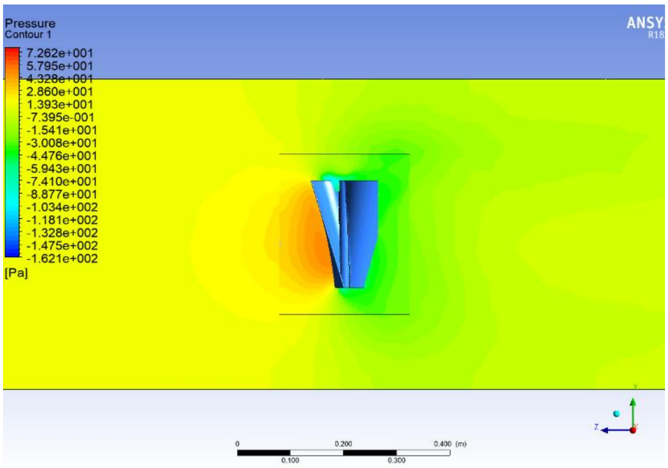

Figure 28. The Model-2's (without end plate) contour of pressure (YZ plane)

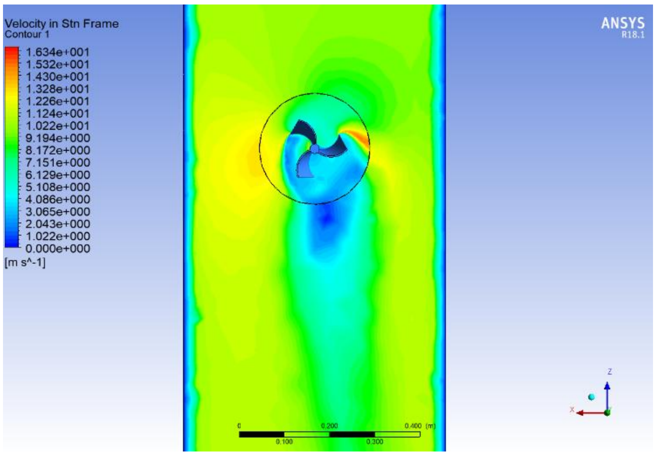

Figure 29. The Model-2's (without end plate) contour of velocity (ZX plane)

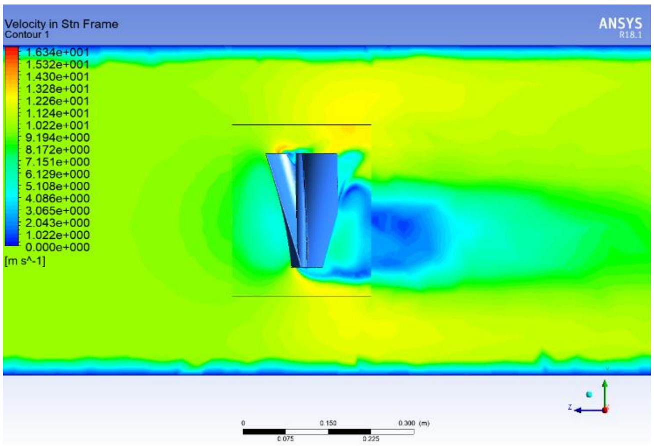

Figure 30. The Model-2's (without end plate) contour of velocity (YZ plane)

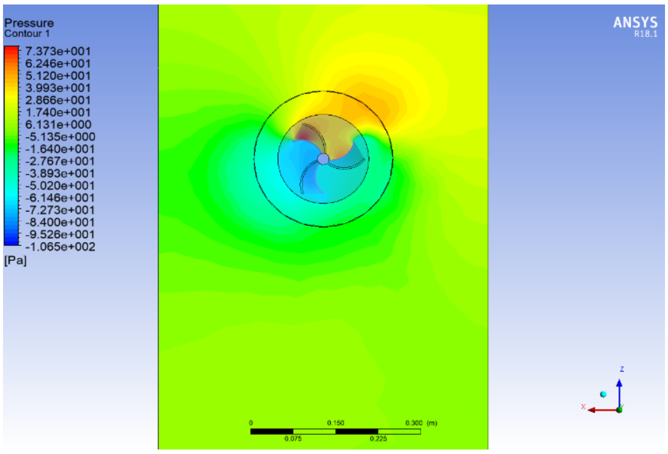

Figure 31. The Model-2's (with 16 cm end plate) contour of pressure (ZX plane)

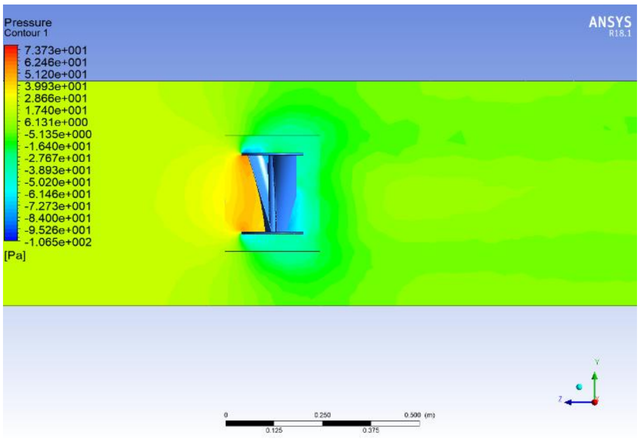

Figure 32. The Model-2's (with 16 cm end plate) contour of pressure (YZ plane)

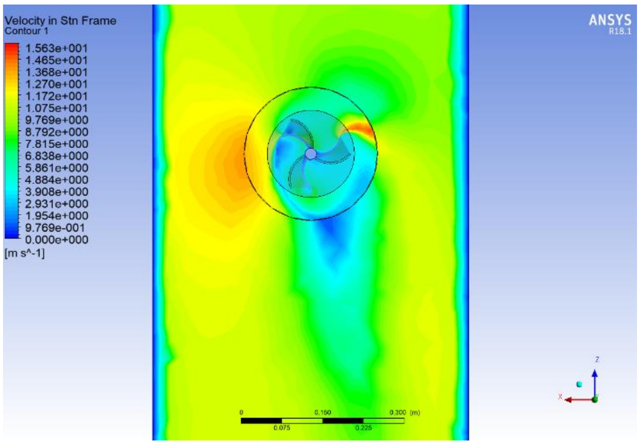

Figure 33. The Model-2's (with 16 cm end plate) velocity of pressure (ZX plane)

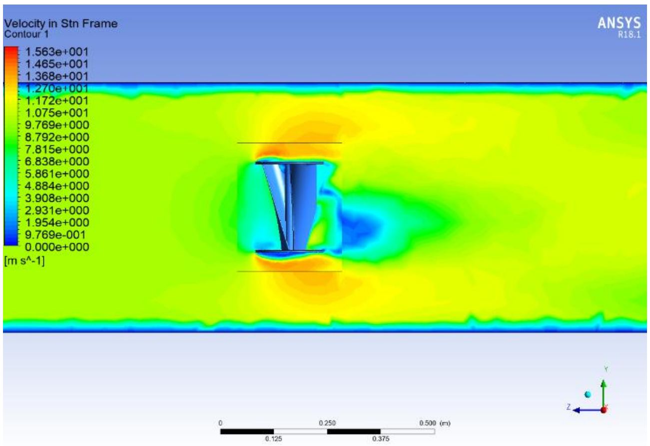

Figure 34. The Model-2's (with 16 cm end plate) velocity of pressure (YZ plane)

Here, figures 27-30 are the velocity and pressure contours of the analysis of the Model-2without plates. In addition, figures (between 31-34) are the velocity and pressure contours of the model formed by placing plates with a diameter of 16 cm on the Model-2. Velocity images obtained from these areas were lower than the plated analysis of the Model-2without plate (figures 29-30) compared to the plated analysis (figures 33-34). Thereason for this is that the Model-2with the plate rotates faster due to the fact that there is more air in the blade in the unit time structure. However, in the pressure contours obtained, it was observed that the Model-2, which was analyzed without a plated (figure 27-28),was less exposed to pressure.It is possible to see the comments made on the results of the numerical analyzes in the Model-1,similarly in the results of the numerical analyzes made in the Model-2.

	Experimental Data				Numerical Data				Relative Error	
Name	n (rpm)	T (Nm)	TSR	C_p	n (rpm)	T (Nm)	TSR	C_p	TSR-%	C_p-%
Model-1 (with no end plates)	552	0,0082	0,4191	0,0300	552	0,0072	0,4191	0,0264	0	12
Model-2 (with no end plates)	492	0,0085	0,3735	0,0277	492	0,0155	0,3735	0,0506	0	82
Model-1 (with 16 cm end plates)	702	0,0091	0,5330	0,0402	702	0,0038	0,5330	0,0168	0	58
Model-2 (with 16 cm end plates)	654	0,0099	0,4965	0,0407	654	0,009	0,4965	0,0370	0	9

Table 5 The table here shows numerical and experimental analysis data

In table 5, 4 numerical and experimental analyses are compared. The best values that can be obtained for the design point (max c_p values) should be examined both experimentally and numerically. Otherwise, it will be difficult to obtain the result because it will cause more time and cost.

3. RESULTS

After analyzing both the numerical analysis and the experimentaldata, it was concludedthat when the diameter of the plates placed on the blades is larger than the nominaldiameter of the models, the yield expression also increases, and when it is small, it has nopositive contribution to the efficiency. In the experimental analysis, it has been observed that Model-2 with 12cm and 16cm end plates aremore efficient than Model-1 with 12cm and 16cm end plates. According to the initial conditions for numerical analysis in Model-2 and Model-1, verification is performed according to max c_p. the result is reliable because the data obtained from experimental analysis and data in numerical analysis are largely matched.

Acknowledgments

We thank Prof. Dr. Selahaddin Orhan Akansu and Merve Uzunoğlu for their assistance on this paper.

Nomenclatures

T	:	Torque (Nm)
P	:	Power (Watt)
P_{wind}	:	Wind Power (Watt)
$P_{turbine}$	:	Turbine Power (Watt)
TSR	:	Tip Speed Ratio (-)
Cp	:	Power Coefficient (-)
μ	:	Dynamic Viscosity (kg/m.s)
ω	:	Angular Velocity (rad/s)
ρ	:	Density (kg/m^3)

REFERENCES

[1] Arsalan O. F. I., Numerical and experimental study with optimization of a small–scale vertical axis wind turbine, 2017. Master's Thesis. Yildiz Technical University.

[2] Kilic F., Goktas M., Savonius Rüzgar Türbini (İkili ve Üçlü) Kanat Çevresi Akışının Sayısal Analizi. Süleyman Demirel Üniversitesi Fen Bilimleri Enstitüsü Dergisi, 2018, 22.3: 1256-1261.

[3] Shigetomi, A.; Murai, Y.; Tasaka, Y.; Takeda, Y. Interactive flow field around two Savonius turbines. Renew. Energy 2011, 36, 536–545.

[4] Sivasegaram,S. Design parameters a ecting the performance of resistance-type, vertical-axis windrotors—An experimental investigation. Wind Eng. 1977, 1-8.

[5] Altan, B.D.; Atılgan, M.; Özdamar, A. An experimental study on improvement of a Savonius rotor performance with curtaining. Exp. Therm. Fluid Sci. 2008, 32, 1673–1678.

[6] Zhao, Z.; Zheng, Y.; Xu, X.; Liu,W. Research on the improvement of the performance of savonius rotor based on numerical study. In Proceedings of the International Conference on Sustainable Power Generation and Supply, Nanjing, China, 6–7 April 2009; pp. 1–6.

[7] S.Teksin, N.Azginoglu, S.O.Akansu, Structure estimation of vertical axis wind turbine using artificial neural network, Alexandria Engineering JournalVolume 61, Issue 1, January 2022, Pages 305-314.

[8] Zhao Z, Zheng Y, Xu X, Hu G. Research on the improvement of the performance of Savonius rotor based on numerical study. In: The proceedings of the international conference on sustainable power generation and supply; 2009. p. 1-6.

[9] Fujisawa, N. On the torque mechanism of Savonius rotors. J. Wind Eng. Ind. Aerodyn. **1992**, 40, 277–292.

[10] Gupta, R.; Biswas, A.; Sharma, K.K. Comparative study of a three-bucket Savonius rotor with a combined three-bucket Savonius-three-bladed Darrieus rotor. Renew. Energy 2008, 33, 1974–1981.

[11] Simsek A., Akansu S.O, Akansu Y.A., Teksin S., Performance Analysis of Savonius Wind Turbines In Different Models, Wind Engineering, 2022

[12] Lee, J.H.; Lee, Y.T.; Lim, H.C. E_ect of twist angle on the performance of Savonius wind turbine. Renew. Energy 2016, 89, 231–244.

[13] Akwa JV, Vielmo HA, Petry AP. A Review on the performance of Savonius wind turbines. Renew Sustain Energy Rev 2012;16(5):3054-64.

[14] Menter FR. Two equations eddy-viscosity turbulence models for engineering. AIAA J 1994;32:1598-605.

[15] Jeon KS, Jeong JI, Pan JK, Ryu KW. Effects of end plates with various shapes and sizes on helical Savonius wind turbines. Renew Energy 2015;79:167-76.

[16] Jeon KS, Jeong JI, Pan JK, Ryu KW. Effects of end plates with various shapes and sizes on helical Savonius wind turbines. Renew Energy 2015;79(1):167–76.

[17] Mohamed MH, Janiga G, Pap E, Thevenin D. Optimization of Savonius turbines using an obstacle shielding the returning blade. Renew Energy 2010;35(11): 2618-26.

[18] YILMAZ, İlker, et al. FarklıRüzgarTürbinKanatProfillerininAerodinamikPerformansınınDeneyselİncelenmesi. PoliteknikDergisi, 2016, 19.4: 577-584.

[19] ÖZDEN, Mustafa, et al. RüzgartürbinikanadindaakişkaynaklideformasyonlarininsayisalvedeneyselIncelenmesi. 3. İzmir RüzgârSempozyumu, 2015.

[20] Saad El-Deen AE, Nawar MAA, Attai YA, Abd El-Maksoud RM. On the enhancement of Savonius Bach-type rotor performance by studying the optimum stator configuration. Ocean Eng2020;217:107954.

[21] ANSYS fluenttheoryguiderelease 15.0. ANSYS, Inc.; 2013.